Linköping studies in science and technology. Thesis.
No. 1656
Licentiate's Thesis

Probabilistic modeling for positioning applications using inertial sensors

Manon Kok

REGLERTEKNIK
AUTOMATIC CONTROL
LINKÖPING

Division of Automatic Control
Department of Electrical Engineering
Linköping University, SE-581 83 Linköping, Sweden
`http://www.control.isy.liu.se`
`manko@isy.liu.se`

Linköping 2014

This is a Swedish Licentiate's Thesis.

Swedish postgraduate education leads to a Doctor's degree and/or a Licentiate's degree.
A Doctor's Degree comprises 240 ECTS credits (4 years of full-time studies).
A Licentiate's degree comprises 120 ECTS credits,
of which at least 60 ECTS credits constitute a Licentiate's thesis.

Linköping studies in science and technology. Thesis.
No. 1656

Probabilistic modeling for positioning applications using inertial sensors

Manon Kok

`manko@isy.liu.se`
`www.control.isy.liu.se`
Department of Electrical Engineering
Linköping University
SE-581 83 Linköping
Sweden

ISBN 978-91-7519-341-0 ISSN 0280-7971 LIU-TEK-LIC-2014:89

Printed by LiU-Tryck, Linköping, Sweden 2014

To everyone who reads this

Abstract

In this thesis, we consider the problem of estimating position and orientation (6D pose) using inertial sensors (accelerometers and gyroscopes). Inertial sensors provide information about the change in position and orientation at high sampling rates. However, they suffer from integration drift and hence need to be supplemented with additional sensors. To combine information from the inertial sensors with information from other sensors we use probabilistic models, both for sensor fusion and for sensor calibration.

Inertial sensors can be supplemented with magnetometers, which are typically used to provide heading information. This relies on the assumption that the measured magnetic field is equal to a constant local magnetic field and that the magnetometer is properly calibrated. However, the presence of metallic objects in the vicinity of the sensor will make the first assumption invalid. If the metallic object is rigidly attached to the sensor, the magnetometer can be calibrated for the presence of this magnetic disturbance. Afterwards, the measurements can be used for heading estimation as if the disturbance was not present. We present a practical magnetometer calibration algorithm that is experimentally shown to lead to improved heading estimates. An alternative approach is to exploit the presence of magnetic disturbances in indoor environments by using them as a source of position information. We show that in the vicinity of a magnetic coil it is possible to obtain accurate position estimates using inertial sensors, magnetometers and knowledge of the magnetic field induced by the coil.

We also consider the problem of estimating a human body's 6D pose. For this, multiple inertial sensors are placed on the body. Information from the inertial sensors is combined using a biomechanical model which represents the human body as consisting of connected body segments. We solve this problem using an optimization-based approach and show that accurate 6D pose estimates are obtained. These estimates accurately represent the *relative* position and orientation of the human body, i.e. the shape of the body is accurately represented but the *absolute* position can not be determined.

To estimate absolute position of the body, we consider the problem of indoor positioning using time of arrival measurements from an ultra-wideband (UWB) system in combination with inertial measurements. Our algorithm uses a tightly-coupled sensor fusion approach and is shown to lead to accurate position and orientation estimates. To be able to obtain position information from the UWB measurements, it is imperative that accurate estimates of the receivers' positions and clock offsets are known. Hence, we also present an easy-to-use algorithm to calibrate the UWB system. It is based on a maximum likelihood formulation and represents the UWB measurements assuming a heavy-tailed asymmetric noise distribution to account for measurement outliers.

Populärvetenskaplig sammanfattning

I denna licentiatsavhandling betraktar vi problemet att skatta position och orientering med hjälp av tröghetssensorer (accelerometrar och gyroskop). Tröghetssensorer tillhandahåller information om förändringar i position och orientering vid höga samplingshastigheter. Nackdelen med denna typ av sensor är att skattningarna driver över tid (integrationsdrift) och behöver därför kompletteras med ytterligare sensorer. För att kombinera information från tröghetssensorer med information från andra sensorer använder vi probabilistiska modeller, både för sensorfusion och för sensorkalibrering.

Tröghetssensorer kan kompletteras med magnetometrar, som typiskt används för att erhålla riktningsinformation. Detta bygger på antaganden att det uppmätta magnetfältet är lika med ett konstant lokalt magnetfält och att magnetometern är korrekt kalibrerad. Närvaron av metalliska föremål i närheten av sensorn kommer att göra det första antagandet ogiltigt. Om det metalliska föremålet och magnetometern sitter ihop utan att kunna röra sig inbördes så kan magnetometern kalibreras med avseende på denna magnetiska störning. Efteråt kan mätningarna användas för riktningsskattning som om störningen inte var närvarande. I denna avhandling presenterar vi en praktisk algoritm för kalibrering av en magnetometer och visar att den leder till förbättrade skattningar av orientering. Ett alternativt tillvägagångssätt är att utnyttja närvaron av magnetiska störningar i inomhusmiljöer genom att använda dem som en källa till positionsinformation. Vi visar att i närheten av en magnetisk spole är det möjligt att erhålla precisa positionsskattningar med användning av tröghetssensorer, magnetometrar och kunskap om det magnetfält som induceras av spolen.

Vi ställer också upp problemet att skatta position och orientering hos en mänsklig kropp. För detta ändamål placeras flera tröghetssensorer på kroppen, och information från dessa kombineras med en biomekanisk modell som representerar den mänskliga kroppen. Denna modell består av kroppssegment som är knutna till varandra. Vi löser det resulterande problemet genom att använda en optimeringsbaserad metod vilket resulterar i korrekta *relativa* positions- och orienteringsskattningar. Detta betyder att formen på kroppen är rätt representerad men den *absoluta* positionen kan inte fastställas.

För att skatta den absoluta positionen av kroppen formulerar vi inomhuspositioneringsproblemet med hjälp av *time of arrival* mätningar från ett *ultra-wideband* (UWB) system i kombination med tröghetsmätningar. Vår algoritm använder ett angreppssätt baserat på *tightly-coupled* sensorfusion och leder till goda positions- och orienteringsskattningar. För att kunna få positionsinformation från UWB mätningar är det nödvändigt att känna till UWB mottagarnas positioner och tidsförskjutningar. För detta ändamål presenterar vi en lättanvänd algoritm för att kalibrera ett UWB system. Den är baserad på en *maximum likelihood* formulering som modellerar bruset hos UWB mätningar med hjälp av en asymmetrisk fördelning med *heavy tails* för att hantera orimliga mätningar.

Acknowledgments

The past 2.5 years have been an incredible journey in which I feel I have learned so much and I have met so many great people. The Automatic Control Group at Linköping University is a very inspiring environment and I am very grateful to Prof. Thomas Schön, Prof. Fredrik Gustafsson and Prof. Svante Gunnarsson for giving me the opportunity to join the group. Our head Prof. Svante Gunnarsson makes sure that there is always a good atmosphere and Ninna Stensgård is always there for help with administrative tasks. I would also like to thank Dr. Henk Luinge and Dr. Jeroen Hol. Without you I would not have started this journey.

My supervisor Prof. Thomas Schön is a great source of inspiration. Our meetings have become longer and longer over the past year but they have also become more and more interesting and I always feel inspired to go back to work afterwards. I would also like to thank my former colleagues at Xsens Technologies, specifically Dr. Henk Luinge and Dr. Jeroen Hol for our collaborations and for always welcoming me back whenever I am in Enschede.

This thesis has been proofread by Dr. Jeroen Hol, Dr. Gustaf Hendeby, Lic. Ylva Jung, Jonas Linder and my supervisors Prof. Thomas Schön and Prof. Fredrik Gustafsson. Your comments have been very valuable! The Swedish abstract would not be in such good shape without the help of Dr. Zoran Sjanic, Prof. Thomas Schön, soon-to-be-Lic. Johan Dahlin, Jonas Linder and Lic. Ylva Jung. Thanks a lot to you all!

Writing the thesis would not have been as easy without the LaTeX template developed and maintained by Dr. Henrik Tidefelt and Dr. Gustaf Hendeby. Gustaf, your LaTeX help, even late in the evenings and during the weekends is very much appreciated. I would also like to thank Dr. Daniel Petersson for introducing me to Ti*k*Z.

It would not have been as easy to move to another country were it not for all my colleagues. We have had a great time both at work and outside of work dancing bugg, playing and learning bridge, going to conferences, going out for a beer, having barbecues etc. I would like to thank my roommate Farzaneh Karami and my former roommate Dr. Zoran Sjanic for their company and for making our room a nice place to work in. I would also like to thank Lic. Sina Khoshfetrat Pakazad for always being the one to arrange fun things to do during weekends and evenings, Lic. Marek Syldatk for making our corridor more lively, Lic. Niklas Wahlström for nice times during conferences in Singapore and Vancouver, Lic. Ylva Jung for being a great friend and for convincing me to sometimes go and do some sports, soon-to-be-Lic. Johan Dahlin, for always being there to help me (and for defending his licentiate one week ahead of me so he always finds out how to do things before me :-)), Jonas Linder for always being there to talk to and all other collegues for making sure that RT is such a nice place to work at and for all the fun things we do outside of work.

This work has been supported by MC Impulse, a European Commission, FP7

research project and by CADICS, a Linnaeus Center funded by the Swedish Research Council (VR). The thesis would not have been possible without their financial support and I would like to hereby gratefully acknowledge both.

I would also like to thank my friends from outside our group. I have met a lot of international PhD students during for instance Swedish course, pedagogics course, our weekly lunches with our lunch group etc. It is great to meet people from all over the world and knowing so many people makes sure that Linköping feels like home.

Last but not least I would like to thank my parents, my sister and Mike. Mike, I know that it is a big change from living together to living 966 km away from each other. I hope you understand that I think it is worth it, thanks for your patience and support!

Finally, I would like to say that I am happy that the licentiate is only a half-way point. I am looking forward to the coming 2.5 years!

Linköping, May 2014
Manon Kok

Contents

II Publications

Notation

SYMBOLS AND OPERATORS

Notation	Meaning
n	Navigation frame
b	Body frame
x_t	State vector at time t
$x_{1:N}$	Set of states from time $t = 1$ to $t = N$
u_t	Known input vector at time t
y_t	Measurements at time t
$y_{1:N}$	Set of measurements from time $t = 1$ to $t = N$
$f_t(\,\cdot\,)$	State update equation at time t
$h_t(\,\cdot\,)$	Measurement equation at time t
$\hat{x}_{t\|t}$	State estimate at time t given measurements up to and including time t
$P_{t\|t}$	State covariance at time t given measurements up to and including time t
θ	Parameter vector
$\hat{\theta}$	Parameter estimate
$p\,(a \mid b)$	Conditional probability of a given b
$p_\theta(b)$	Probability of b parametrized by θ
$\mathcal{N}(\mu, \sigma^2)$	Gaussian distribution with mean μ and covariance σ^2
$\mathrm{Cauchy}(\mu, \gamma)$	Cauchy distribution with location parameter μ and scale parameter γ
$\emptyset$	Empty set
$\in$	Is a member of
$A \subseteq B$	A is a subset of or is included in B
$\mathbb{R}$	Set of real numbers
$\arg\max$	Maximizing argument
$\arg\min$	Minimizing argument
$\|\|a\|\|_2$	Two-norm of the vector a

SYMBOLS AND OPERATORS

Notation	Meaning
$\mathcal{I}_n$	$n \times n$ identity matrix
$\triangleq$	Defined as
$\frac{\partial y}{\partial x}$	Partial derivative of y with respect to x
$\det A$	Determinant of the matrix A
A^T	Transpose of the matrix A
$[a\times]$	Cross product matrix of the vector a
A^{-1}	Inverse of the matrix A
$\odot$	Quaternion multiplication
q^L	Left quaternion multiplication of the quaternion q
q^R	Right quaternion multiplication of the quaternion q
q_v	Vector part of the quaternion q

ABBREVIATIONS

Abbreviation	Meaning
BFGS	Broyden-Fletcher-Goldfarb-Shanno
EKF	Extended Kalman filter
GPS	Global positioning system
IMU	Inertial measurement unit
KF	Kalman filter
MAP	Maximum a posteriori
MEKF	Multiplicative extended Kalman filter
MEMS	Micro-machined electromechanical system
ML	Maximum likelihood
NLOS	Non-line-of-sight
PDF	Probability density function
PF	Particle filter
PF-MAP	Maximum a posteriori estimate for the particle filter
RBPF	Rao-Blackwellized particle filter
RBPF-MAP	Maximum a posteriori estimate for the Rao-Blackwellized particle filter
SLAM	Simultaneous localization and mapping
TOA	Time of arrival
UWB	Ultra-wideband

Part I

Background

1

Introduction

In this thesis, we consider the problem of estimating position and orientation using inertial sensors (accelerometers and gyroscopes). Throughout the thesis, the inertial measurements are used in combination with other sensors, namely magnetometers and time of arrival (TOA) measurements from an ultra-wideband (UWB) system. We also consider the problem of using multiple inertial sensors placed on the human body to estimate the body's position and orientation (6D pose). Information from the inertial sensors is in that case combined using a biomechanical model which represents the human body as consisting of body segments that are attached to each other. To efficiently combine information from different sensors and different models, we rely on probabilistic models.

Part I of this thesis serves as background material to Part II in which four papers are presented. Hence, in Part I we will frequently refer to the different papers in Part II. In Section 1.1 of this chapter, we will first give a short description of the different sensors used throughout this thesis. Subsequently, the topic of probabilistic modeling will be introduced in Section 1.2. In the remainder we will discuss some example applications and summarize the contributions of this thesis.

1.1 Sensors

In this section we will introduce the sensors that are used throughout this thesis. In all four papers in Part II, our algorithms make use of inertial measurements from an inertial measurement unit (IMU). The IMUs we use are based on micro-machined electromechanical system (MEMS) technology and are equipped with both inertial sensors (see Section 1.1.1) and with a three-axis magnetometer (see

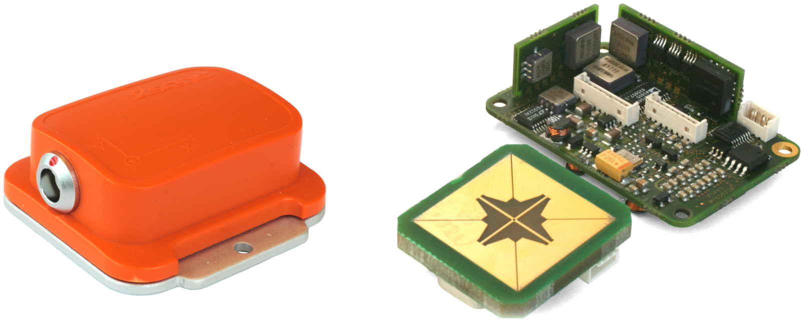

Figure 1.1: *Example sensors. Left and right: an inertial measurement unit (IMU) with and without casing. Middle: an ultra-wideband (UWB) transmitter. By courtesy of Xsens Technologies.*

Section 1.1.2). An example of an IMU can be found in Figure 1.1.

1.1.1 Inertial sensors

The term *inertial sensor* is used to denote the combination of a three-axis accelerometer and a three-axis gyroscope. A gyroscope measures the sensor's angular velocity, i.e. the rate of change of the sensor's orientation. Hence, integration of the gyroscope signals provides information about the orientation of the sensor.

An accelerometer measures the external specific force acting on the sensor. The specific force consists of both the sensor's acceleration and the earth's gravity. The earth's gravity is of the order of 9.81 m/s^2, while the sensor's acceleration is generally of much smaller magnitude. The accelerometer measurements will therefore typically consist of a large contribution from the earth's gravity and a relatively small contribution due to the motion of the sensor. After subtraction of the earth's gravity, double integration of the accelerometer signals provides information about the sensor position. To subtract earth's gravity, however, it is necessary that the orientation of the sensor is known. Hence, estimation of the sensor's position and orientation are inextricably linked when using inertial sensors. The combined estimation of both position and orientation is sometimes called *pose estimation*. The process of estimating position and orientation using inertial sensors is summarized in Figure 1.2.

The integration steps from angular velocity to rotation and acceleration to position introduce *integration drift*. Hence, errors in the measurements have a large impact on the quality of the estimated position and orientation using inertial sensors only. This is specifically the case for position, which relies both on double integration of the acceleration and on accurate orientation estimates to subtract the earth's gravity. Because of this, inertial sensors need to be supplemented with other sensors to lead to accurate position and orientation estimates. The inertial measurements can for instance be combined with TOA measurements from a UWB system. UWB will be introduced in Section 1.1.3.

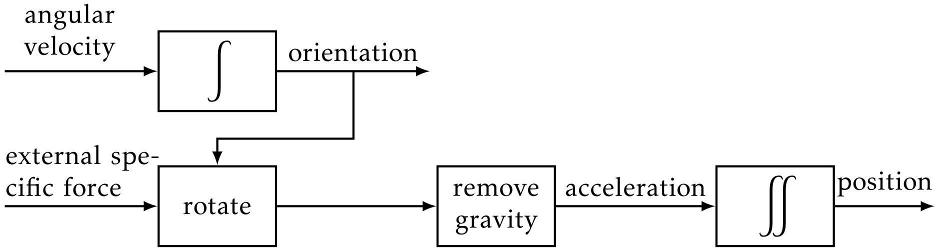

Figure 1.2: *Schematic illustration of the process of determining position and orientation from the accelerometer measurements (external specific force) and the gyroscope measurements (angular velocity), assuming a known initial position and orientation.*

In case we are interested in orientation estimation only, it is possible to use inertial sensors in combination with a magnetometer. For this, however, we need an additional model assumption concerning the acceleration. One can recognize that when the sensor is (almost) not accelerating, the accelerometer (almost) only measures the gravity. Using this model assumption, the accelerometer measurements can provide an estimate of the vertical direction (aligned with the gravity vector). The angle of deviation from the vertical is called the inclination. The accelerometer measurements can hence be said to *stabilize* the inclination estimates from the gyroscope. They do, however, not provide any information about the heading, i.e. the rotation around the vertical axis. Information about this can be obtained from magnetometers, which will be introduced in Section 1.1.2. Since IMUs often consist of both inertial sensors and magnetometers, it is for many applications possible to obtain accurate orientation estimates using an IMU.

1.1.2 Magnetometers

A magnetometer measures the strength and the direction of the magnetic field. In combination with inertial sensors, magnetometers typically serve the purpose of a compass and are used to determine the sensor's heading. This approach relies on the assumption that the magnetic field is at least locally constant and that it points in the direction of a local magnetic north. This is specifically the case when there are no magnetic objects in the vicinity of the sensor. In that case the magnetometer only measures the earth's magnetic field. Both the magnitude and the direction of the earth's magnetic field depend on the location on the earth, as depicted in Figure 1.3. However, the horizontal component of the magnetic field always points towards the earth's magnetic north.

Magnetometers typically provide accurate measurements of the magnetic field at high sampling rates. The measured magnetic field is, however, often not equal to the earth's magnetic field due to the presence of metallic objects in the vicinity of the sensor. The presence of objects causing magnetic disturbances is typically considered to be undesirable since they negatively affect the heading estimates.

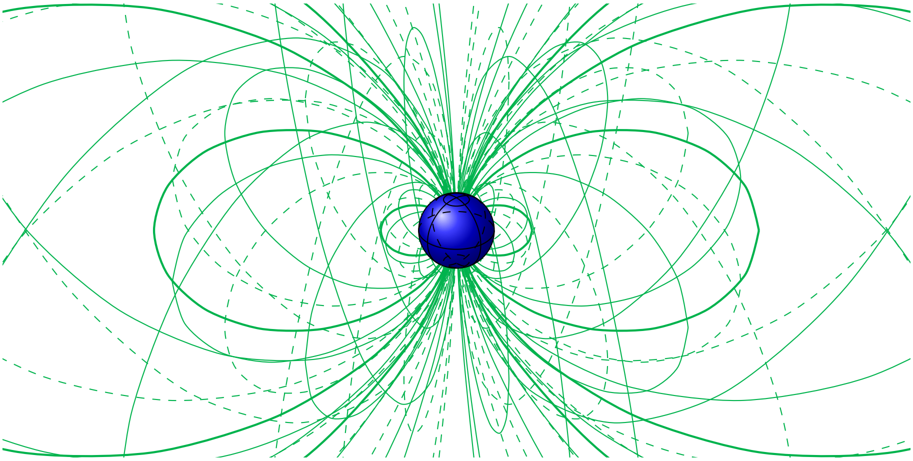

Figure 1.3: *Schematic of the earth magnetic field lines (green) around the earth (blue).*

However, if the metallic object is rigidly attached to the sensor the magnetometer can be calibrated for the presence of this disturbance. Afterwards, the measurements can be used for heading estimation as if the disturbance was not present. Example scenarios for which this calibration can be used are when a magnetometer is attached to e.g. a smartphone, a car or an aircraft. Magnetometer calibration is the topic of Paper A, where a practical magnetometer calibration algorithm is derived.

An alternative approach is to exploit the presence of magnetic disturbances in indoor environments by using them as a source of position information, see e.g. Angermann et al. (2012); Frassl et al. (2013). This approach assumes that knowledge of the magnetic field is represented as a map in which we want to localize the sensor. For instance, the strength and/or direction of the magnetic field at a specific location can be compared with a magnetic field map of the environment to estimate possible sensor locations. This is the topic of Paper D.

1.1.3 Ultra-wideband

A third type of measurements used in Part II of this thesis is based on TOA measurements from a UWB system. The UWB system consists of a number of stationary UWB receivers and a number of mobile transmitters, as depicted in Figure 1.4. The UWB transmitter (see also Figure 1.1) sends out a UWB pulse. The receivers measure the time of arrival of the pulse. Ideally, the time it takes for the pulse to reach the receivers is proportional to the distance between the transmitter and the receiver. However, due to multipath or non-line-of-sight (NLOS) conditions, the pulse can be delayed leading to a measurement *outlier*. In Paper B we consider the problem of indoor positioning using UWB measurements in combination with inertial measurements. The paper focuses on sensor fusion between

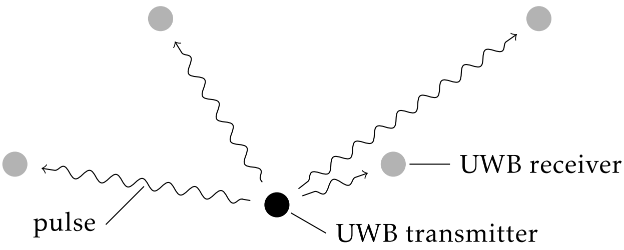

Figure 1.4: *The UWB setup consists of a number of stationary receivers making TOA measurements of signal pulses originating from a mobile transmitter.*

the UWB measurements and the inertial measurements. It also presents a calibration algorithm that determines the positions and clock offsets of the receivers and a novel approach to obtain position estimates using only the UWB measurements.

1.2 Probabilistic modeling

In this thesis we use measurements from the sensors discussed in Section 1.1 in combination with models to estimate the sensor's position and orientation. Both the measurements and the models provide uncertain information, for instance due to measurement noise or measurement outliers, but also due to model imperfections. Hence, we reason about our problem in terms of random variables with a *probability density function* (PDF). Combining information from different sensors based on a probabilistic framework is called *sensor fusion*, see e.g. Gustafsson (2012).

We typically describe our problems in the form of a *state-space model*,

$$x_{t+1} = f_t(x_t, u_t, \theta, v_t), \tag{1.1a}$$
$$y_t = h_t(x_t, \theta, e_t), \tag{1.1b}$$

where (1.1a) is the *dynamics* or *state update equation* and (1.1b) is the *measurement equation*. The dynamics model how the state changes over time, i.e. they describe the state x at time $t+1$, denoted x_{t+1}, in terms of a possibly nonlinear and time-varying model $f_t(\cdot)$. The model $f_t(\cdot)$ depends on the state x, the input u and the process noise v at time t, and on a constant parameter vector θ. The measurement equation models the measurements y_t as a function $h_t(\cdot)$ of the state x_t, i.e. it describes which information about the state can be inferred from the measurements. The function $h_t(\cdot)$ also depends on a constant parameter vector θ and the measurement noise e_t. The noise terms v_t and e_t can reflect our confidence in the models and in the measurements, respectively. They can also be used to model different noise distributions to for instance take into account the presence of measurement outliers.

State-space models (1.1) are often used for *state estimation*, where we estimate the state $x_{1:N} = \{x_1, \ldots, x_N\}$. State estimation is often done using a *maximum a posteriori* (MAP) approach,

$$\hat{x}_{1:N}^{\mathrm{MAP}} = \arg\max_{x_{1:N}} \; p(x_{1:N} \mid y_{1:N}), \tag{1.2}$$

where $p(a \mid b)$ denotes the conditional probability of a given b. Hence, the estimated state $x_{1:N}$ is chosen to be the one most likely from the measurements $y_{1:N} = \{y_1, \ldots, y_N\}$. Various techniques exist to obtain the MAP estimate. In Chapter 2 we will discuss background to the state estimation techniques that are used in the papers presented in Part II of this thesis.

In specific situations, the model parameters θ are unknown and need to be estimated from data. An example of this is sensor calibration where for instance the presence of an unknown measurement bias could be modeled as an unknown parameter in the measurement equation (1.1b). Estimation of parameters in a state-space model is also called *grey-box system identification* (Ljung, 1999; Bohlin, 2006). It can be done using *maximum likelihood* (ML) estimation,

$$\hat{\theta}^{\mathrm{ML}} = \arg\max_{\theta \in \Theta} \; p_\theta(y_{1:N}), \tag{1.3}$$

where $p_\theta(b)$ denotes the probability of b parametrized by θ. The parameter vector θ is an n_θ-dimensional vector which can be limited to a subset Θ of $\mathbb{R}^{n_\theta}$, i.e. the optimization is performed over $\theta \in \Theta$ with $\Theta \subseteq \mathbb{R}^{n_\theta}$. The problem of sensor calibration will be discussed in more detail in Chapter 3 and will be the subject of Paper A and of part of Paper B.

1.3 Example applications

Position and orientation estimation is of interest for a wide range of applications. One can think of for instance aircraft or car localization, but also of pedestrian localization (Hol, 2011; Woodman, 2010; Grzonka, 2011; Callmer, 2013). For outdoor applications, it is typically possible to make use of measurements from a global positioning system (GPS). For indoor positioning, however, GPS signals are not available.

As discussed in Section 1.1.1, inertial sensors provide information about the change in orientation and position at high sampling rates. With the development of MEMS technology, small inertial sensors which can be worn on the human body have become available. This has applications in for instance pedestrian tracking (Woodman, 2010) which often focuses on estimating the position of first-responders such as fire-fighters (Grzonka, 2011; Callmer, 2013). It also has applications for human body motion capture which is the subject of Paper C. There, a subject wears a suit with 17 IMUs on different body segments. The inertial measurements are used in combination with a biomechanical model to estimate the pose of the body. This biomechanical model is used to represent the assumption that the different body segments are (and remain) attached to each other. An example of pose estimates using inertial sensors is shown in Figure 1.5. The motion

Figure 1.5: *Example of inertial human body motion capture. Left: olympic and world champion speed skating Ireen Wüst wearing an inertial motion capture suit with* 17 *inertial sensors. Right: graphical representation of the estimated position and orientation of the body segments. By courtesy of Xsens Technologies.*

Figure 1.6: *Example of inertial motion capture using* 17 *inertial sensors as well as* 3 *UWB transmitters on the head and on the feet. The estimated pose is shown in orange. By courtesy of Xsens Technologies.*

capture suit can also be used in combination with UWB measurements. Paper B focuses on the use of UWB measurements and the sensor fusion of UWB measurements with inertial measurements. In Figures 1.6 and 1.7 a subject is shown who wears 17 inertial sensors as well as 3 UWB transmitters, on both his feet and his head.

1.4 Thesis outline

The thesis is divided into two parts, with edited versions of published and unpublished papers in Part II. In Part I, we will give background information relevant to the different papers.

Part I – Background

In Chapter 2, we describe the subject of pose estimation using inertial sensors and magnetometers. We focus on different algorithms/algorithm implementations to estimate the sensor's orientation. This serves as background material to Papers A, B and C. We also discuss some issues related to particle filtering for

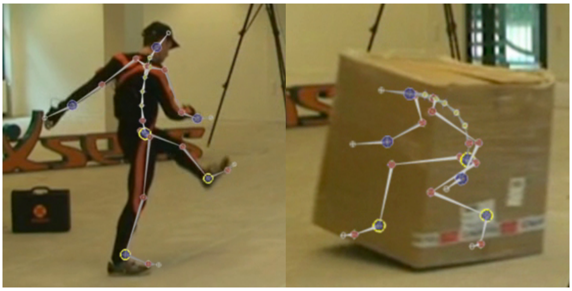

Figure 1.7: *Example of inertial motion capture using* 17 *inertial sensors as well as* 3 *UWB transmitters on the head and on the feet. The estimated pose is overlaid on the body. As discussed in Section 1.1.3, UWB does not require line-of-sight. Hence, it is also possible to get good pose estimates when the subject is covered by for instance a box (right plot).*

pose estimation using the magnetic field as a source of position information as in Paper D. In Chapter 3, we discuss the topic of sensor calibration. It provides background to the magnetometer calibration problem in Paper A and the UWB calibration algorithm presented in Paper B. Part I concludes with a summary of the contributions of the papers and a discussion of possible directions for future work.

Part II – Publications

Part II of the thesis consists of edited versions of four papers. These papers contain the following main contributions of this thesis:

- A novel magnetometer calibration algorithm which uses inertial sensors to calibrate the magnetometer for the presence of magnetic disturbances, for magnetometer sensor errors and for misalignment between the magnetometer and the inertial sensor axes [Paper A].
- A novel approach to combine inertial measurements with TOA measurements from a UWB system for indoor positioning. We present a tightly-coupled sensor fusion approach to combine the inertial measurements and the UWB measurements, an easy-to-use algorithm to calibrate the UWB setup and a novel multilateration approach to estimate the transmitter's position from the UWB measurements [Paper B].
- A novel inertial human body motion capture approach which solves the motion capture problem using an optimization-based approach [Paper C].
- A novel algorithm for 6D pose estimation where inertial measurements are complemented with magnetometer measurements assuming that a magnetic field map is known. In this approach, the magnetometer measurements are hence used as a source of position information [Paper D].

Below we provide a summary of each paper together with a discussion of the background and of the author's contributions.

Paper A: Magnetometer calibration using inertial sensors

Paper A is an edited version of

> M. Kok and T. B. Schön. Magnetometer calibration using inertial sensors. *Preprint*, 2014b.

Earlier versions of this work were presented in

> M. Kok and T. B. Schön. Maximum likelihood calibration of a magnetometer using inertial sensors. In *Proceedings of the 19th World Congress of the International Federation of Automatic Control (accepted for publication)*, Cape Town, South Africa, August 2014a,
>
> M. Kok, J. D. Hol, T. B. Schön, F. Gustafsson, and H. Luinge. Calibration of a magnetometer in combination with inertial sensors. In *Proceedings of the 15th International Conference on Information Fusion*, Singapore, July 2012.

Summary: In this work we present a practical calibration algorithm that calibrates a magnetometer using inertial sensors. The calibration corrects for magnetometer sensor errors, for the presence of magnetic disturbances and for misalignment between the magnetometer and the inertial sensor axes. It is based on a maximum likelihood formulation and is formulated as an offline method. It is shown to give good results using data from two different commercially available sensor units. Using the calibrated magnetometer measurements in combination with the inertial sensors to determine orientation, is shown to lead to significantly improved heading estimates.

Background and contributions: Before the author of this thesis started her work as a PhD student at Linköping University, she worked at Xsens Technologies. During this time she studied the topic of magnetometer calibration. Hence, the magnetometer calibration problem provided a good starting point for research during her PhD. A first paper on this subject has therefore been co-authored with Dr. Jeroen Hol and Dr. Henk Luinge from Xsens Technologies. Later work has mainly been done in cooperation with Prof. Thomas Schön. Dr. Henk Luinge and Laurens Slot from Xsens Technologies and Dr. Gustaf Hendeby from Linköping University have been so kind as to help in collecting the data sets presented in the paper. The author of this thesis has implemented the calibration algorithm and has written a major part of the paper.

Paper B: Indoor positioning using ultra-wideband and inertial measurements

Paper B is an edited version of

> M. Kok, J. D. Hol, and T. B. Schön. Indoor positioning using ultra-wideband and inertial measurements. *Preprint*, 2014b.

Summary: In this work we present an approach to combine measurements from accelerometers and gyroscopes (inertial sensors) with time of arrival measurements from an ultra-wideband system for indoor positioning. Our algorithm uses a tightly-coupled sensor fusion approach and is shown to lead to accurate 6D pose (position and orientation) estimates as compared to data from an optical reference system. To be able to obtain position information from the ultra-wideband measurements, it is imperative that accurate estimates of the receivers' positions and clock offsets are known. Hence, we also present an easy-to-use algorithm to calibrate the ultra-wideband system. It is based on a maximum likelihood formulation and represents the ultra-wideband measurements assuming a heavy-tailed asymmetric noise distribution to account for measurement outliers. Using the heavy-tailed asymmetric noise distribution and the calibration results, it is shown that accurate position estimates can be obtained from the ultra-wideband measurements using a novel multilateration approach.

Background and contributions: The co-authors of this paper, Dr. Jeroen Hol and Prof. Thomas Schön, have been working on the subject of indoor positioning using ultra-wideband measurements and inertial measurements, resulting in the two papers Hol et al. (2009, 2010) and in the results presented in Hol (2011). The author of this thesis has extended the calibration and multilateration algorithms from Hol (2011); Hol et al. (2010) by assuming a heavy-tailed asymmetric distribution to represent the outliers in the ultra-wideband measurements. The presented sensor fusion results are based on previous results from Hol et al. (2009). The paper has been written together with Dr. Jeroen Hol.

Paper C: An optimization-based approach to human body motion capture using inertial sensors

Paper C is an edited version of

> M. Kok, J. D. Hol, and T. B. Schön. An optimization-based approach to human body motion capture using inertial sensors. In *Proceedings of the 19th World Congress of the International Federation of Automatic Control (accepted for publication)*, Cape Town, South Africa, August 2014a.

Summary: In inertial human motion capture, a multitude of body segments are equipped with inertial measurement units, consisting of 3D accelerometers, 3D gyroscopes and 3D magnetometers. Relative position and orientation estimates can be obtained using the inertial data together with a biomechanical model. In this work we present an optimization-based solution to magnetometer-free inertial motion capture. It allows for natural inclusion of biomechanical constraints, for handling of nonlinearities and for using all data in obtaining an estimate. As a proof-of-concept we apply our algorithm to a lower body configuration, illustrating that the estimates are drift-free and match the joint angles from an optical reference system.

Background and contributions: The co-authors Dr. Jeroen Hol and Prof. Thomas Schön came up with the idea of solving the human body motion capture problem as an optimization problem. The implementation of the optimization algorithm has been done using a framework developed by Xsens Technologies. With this framework, it is possible to define the optimization problem at a high level. The author of this thesis has been involved in developing and implementing the algorithm, in the data collection and has written a major part of the paper.

Paper D: MEMS-based inertial navigation based on a magnetic field map

Paper D is an edited version of

> M. Kok, N. Wahlström, T. B. Schön, and F. Gustafsson. MEMS-based inertial navigation based on a magnetic field map. In *Proceedings of the 38th International Conference on Acoustics, Speech, and Signal Processing (ICASSP)*, pages 6466–6470, Vancouver, Canada, May 2013.

Summary: This paper presents an approach for 6D pose estimation where MEMS inertial measurements are complemented with magnetometer measurements assuming that a model (map) of the magnetic field is known. The resulting estimation problem is solved using a Rao-Blackwellized particle filter. In our experimental study the magnetic field is generated by a magnetic coil giving rise to a magnetic field that we can model using analytical expressions. The experimental results show that accurate position estimates can be obtained in the vicinity of the coil, where the magnetic field is strong.

Background and contributions: The idea of looking into pose estimation using magnetometers as a source of position information was started through discussions with Dr. Slawomir Grzonka during the CADICS "Learning World Models" workshop in 2010 in Linköping. The experiments used in the paper were performed while the author of this thesis was working at Xsens Technologies. During this time, a first implementation of the pose estimation algorithm was made, using an extended Kalman filter. During the author's time at Linköping University, the work has been extended with an implementation using a Rao-Blackwellized particle filter. The author of this thesis wrote a major part of this paper.

Publications of related interest, but not included in this thesis

> J. Kronander, J. Dahlin, D. Jönsson, M. Kok, T. B. Schön, and J. Unger. Real-time video based lighting using GPU raytracing. In *Proceedings of the 2014 European Signal Processing Conference (EUSIPCO)*, Lisbon, Portugal, September 2014. (submitted, pending review).

> N. Wahlström, M. Kok, T. B. Schön, and F. Gustafsson. Modeling magnetic fields using Gaussian processes. In *Proceedings of the 38th International Conference on Acoustics, Speech, and Signal Processing (ICASSP)*, pages 3522–3526, Vancouver, Canada, May 2013.

2

Pose estimation using inertial sensors and magnetometers

As discussed in Chapter 1, position and orientation estimation are closely related in the case of inertial sensors. Pose estimation denotes the simultaneous estimation of position and orientation. One can use standard estimation techniques for this. However, due to the nonlinear nature of the orientation and the different orientation representations, it is not obvious what is the best technique to use to estimate the orientation. In the different papers we use a variety of different techniques for orientation estimation, depending on the particular situation. In this chapter we will discuss a few different approaches and their pros and cons.

We start by introducing different representations of orientations in Section 2.1. Subsequently, two different *extended Kalman filter* (EKF) implementations are discussed in Section 2.2. EKFs can be used to solve the MAP problem (1.2) introduced in Chapter 1. Section 2.3 will introduce an alternative way of solving the MAP problem (1.2) using optimization techniques. In Section 2.4, some details with respect to particle filtering will be discussed.

2.1 Orientation representations

The orientation of an object is defined as the rotation between its coordinate frame with respect to a second coordinate frame. In this thesis we will mostly make use of the body coordinate frame b and the navigation coordinate frame n. The body frame b has its origin in the center of the accelerometer triad and its axes are aligned with the inertial sensor axes. The navigation frame n is aligned with the earth's gravity and the local magnetic field.

Orientation can be represented in many different ways (Shuster, 1993). Perhaps the most intuitive representation is to make use of Euler angles. Rotation in

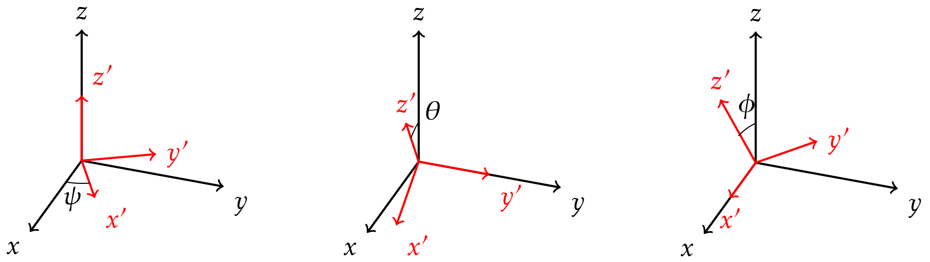

Figure 2.1: *Definition of the Euler angles with left: rotation ψ around the z-axis, middle: rotation θ around the y-axis and right: rotation ϕ around the x-axis.*

terms of Euler angles is defined as a consecutive rotation around the three axes. We use the convention (z, y, x) which first rotates around the z-axis, subsequently around the y-axis and finally around the x-axis. The rotations around the three axes, often denoted as the roll ϕ, the pitch θ and the yaw ψ angles, are depicted in Figure 2.1. Although Euler angles are an intuitive representation of orientation, they suffer from ambiguities. For instance, any addition of 2π to the different angles results in the same orientation. Another ambiguity is sometimes called gimbal lock where certain rotation sequences lead to the same orientation, for instance the rotation $(0, \pi/2, \pi)$ is equal to the rotation $(-\pi, \pi/2, 0)$.

An alternative way to represent orientation is to use rotation matrices where the rotation matrix representation of the Euler angle rotation (ψ, θ, ϕ) is given by

$$\begin{aligned} R &= \begin{pmatrix} 1 & 0 & 0 \\ 0 & \cos\phi & \sin\phi \\ 0 & -\sin\phi & \cos\phi \end{pmatrix} \begin{pmatrix} \cos\theta & 0 & -\sin\theta \\ 0 & 1 & 0 \\ \sin\theta & 0 & \cos\theta \end{pmatrix} \begin{pmatrix} \cos\psi & \sin\psi & 0 \\ -\sin\psi & \cos\psi & 0 \\ 0 & 0 & 1 \end{pmatrix} \\ &= \begin{pmatrix} \cos\theta\cos\psi & \cos\theta\sin\psi & -\sin\theta \\ \sin\phi\sin\theta\cos\psi - \cos\phi\sin\psi & \sin\phi\sin\theta\sin\psi + \cos\phi\cos\psi & \sin\phi\cos\theta \\ \cos\phi\sin\theta\cos\psi + \sin\phi\sin\psi & \cos\phi\sin\theta\sin\psi - \sin\phi\cos\psi & \cos\phi\cos\theta \end{pmatrix}. \end{aligned} \tag{2.1}$$

Rotation matrices are a useful orientation representation and they will frequently be used throughout this thesis. For orientation *estimation* purposes, however, rotation matrices are less suitable. The reason is that they would lead to a 9-dimensional state vector subject to the following constraints

$$RR^{\mathsf{T}} = R^{\mathsf{T}}R = \mathcal{I}_3, \quad \det R = 1, \tag{2.2}$$

where $\mathcal{I}_3$ denotes a 3×3 identity matrix.

A commonly used alternative orientation representation is that of unit quaternions. Quaternions were first introduced by Hamilton (1844) and are widely used in orientation estimation algorithms, see e.g. Kuipers (1999); Hol (2011).

Quaternions use a 4-dimensional description of the orientation

$$q = \begin{pmatrix} q_0 & q_1 & q_2 & q_3 \end{pmatrix}^\mathsf{T} = \begin{pmatrix} q_0 \\ q_v \end{pmatrix}, \tag{2.3}$$

with the constraint that $\|q\|_2 = 1$. The rotation matrix R and the quaternion q are related by

$$\begin{aligned} R &= q_v q_v^\mathsf{T} + q_0^2 \mathcal{I}_3 + 2q_0[q_v \times] + [q_v \times]^2 \\ &= \begin{pmatrix} 2q_0^2 + 2q_1^2 - 1 & 2q_1q_2 - 2q_0q_3 & 2q_1q_3 + 2q_0q_2 \\ 2q_1q_2 + 2q_0q_3 & 2q_0^2 + 2q_2^2 - 1 & 2q_2q_3 - 2q_0q_1 \\ 2q_1q_3 - 2q_0q_2 & 2q_2q_3 + 2q_0q_1 & 2q_0^2 + 2q_3^2 - 1 \end{pmatrix}, \end{aligned} \tag{2.4}$$

where $[q_v \times]$ denotes the cross product matrix

$$[q_v \times] = \begin{pmatrix} 0 & -q_3 & q_2 \\ q_3 & 0 & -q_1 \\ -q_2 & q_1 & 0 \end{pmatrix}. \tag{2.5}$$

Special quaternion algebra is available, see e.g. Kuipers (1999); Hol (2011). In this chapter, we will only introduce the quaternion algebra needed to derive the algorithms.

Note that a rotation is always represented from one coordinate frame to another. Hence, we use a double superscript on the rotation matrix R and the quaternion q as

$$m^\mathrm{n} = R^\mathrm{nb} m^\mathrm{b}, \tag{2.6}$$

where m^b is a vector in the body frame b and the rotation matrix R^nb rotates the vector to the navigation frame n. Equivalently,

$$m^\mathrm{b} = \left(R^\mathrm{nb}\right)^\mathsf{T} m^\mathrm{n} = R^\mathrm{bn} m^\mathrm{n}. \tag{2.7}$$

where a vector m^n in the navigation frame n is rotated to the body frame b using the rotation matrix $(R^\mathrm{nb})^\mathsf{T} = R^\mathrm{bn}$.

2.2 Extended Kalman filters for orientation estimation

Orientation estimation is a state estimation problem, where the state $x_{1:N}$ in a state-space model (see (1.1)) is estimated from a time update and a measurement model. As discussed in Section 1.2, state estimation aims at obtaining a MAP estimate of the state. In the case of linear models this can be done using a *Kalman filter* (KF). KFs were first introduced by Kalman (1960) and are the best linear unbiased filters in the sense that they minimize the variance of the state estimation error. The EKF is an extension of the Kalman filter which makes the filter also applicable to nonlinear models. Unlike KFs, EKFs are not guaranteed to minimize the variance of the state estimation error. Actually, no guarantees for the quality of the EKF estimates can be given (Rawlings and Mayne, 2009). However, in cases where the model is not "too" nonlinear, they typically work well. EKFs are widely used due to their simplicity and computational efficiency, see e.g. Xsens Technologies B.V. (2014); Gustafsson (2012). For our case of estimating orientation using inertial measurements, EKFs are known to work quite well. The reason is that due to the high sampling rates of the IMU, each update in the EKF is typically not very nonlinear.

In the case of orientation estimation, the state in the EKF represents the orientation. Hence, a choice needs to be made which of the orientation representations (see Section 2.1) to use to represent the state. In this section, we will introduce two different EKF implementations for orientation estimation. To introduce the problem, in Section 2.2.1 we will first introduce the well-known EKF equations. Sections 2.2.3 and 2.2.4 will subsequently introduce EKF implementations to estimate orientation. The first uses a 4-dimensional quaternion state vector, the second uses a 3-dimensional state vector representing the orientation deviation from a linearization point. These discussions will focus on the simplest model to estimate orientations, i.e. we focus on an EKF implementation with *only* orientation states.

2.2.1 The extended Kalman filter

An EKF uses a nonlinear state-space model (1.1) as introduced in Section 1.2. We typically assume that the measurement noise is additive, and that both the process and the measurement noise are zero-mean Gaussian with constant covariance, i.e.

$$x_{t+1} = f_t(x_t, u_t, v_t), \tag{2.8a}$$

$$y_t = h_t(x_t) + e_t, \tag{2.8b}$$

with $v_t \sim \mathcal{N}(0, Q)$ and $e_t \sim \mathcal{N}(0, R)$.

The EKF estimates the state by performing a *time update* and a *measurement update*. The time update uses the model (2.8a) to “predict” the state to the next time step according to

$$\hat{x}_{t+1|t} = f_t(\hat{x}_{t|t}, u_t), \tag{2.9a}$$

$$P_{t+1|t} = A_t P_{t|t} A_t^\mathsf{T} + G_t Q G_t^\mathsf{T}, \tag{2.9b}$$

with

$$A_t = \left.\frac{\partial f_t(x_t,u_t,v_t)}{\partial x_t}\right|_{x_t=\hat{x}_{t|t}, v_t=0}, \qquad G_t = \left.\frac{\partial f_t(x_t,u_t,v_t)}{\partial v_t}\right|_{x_t=\hat{x}_{t|t}, v_t=0}. \tag{2.10}$$

Here, $\hat{x}$ is used to distinguish the *estimated* state from the “true” state x. The matrix P denotes the state covariance. The double subscripts on $\hat{x}_{t+1|t}$ and $P_{t+1|t}$ denote the state estimate and the state covariance at time $t + 1$ given measurements up to time t. Similarly, $\hat{x}_{t|t}$ and $P_{t|t}$ denote the state estimate and the state covariance at time t given measurements up to time t.

The measurement update uses the measurement model (2.8b) in combination with the measurements y_t to update the "predicted" state estimate as

$$\hat{x}_{t|t} = \hat{x}_{t|t-1} + P_{t|t-1} C_t^{\mathsf{T}} \left(C_t P_{t|t-1} C_t^{\mathsf{T}} + R \right)^{-1} \left(y_t - \hat{y}_{t|t-1} \right), \tag{2.11a}$$

$$P_{t|t} = P_{t|t-1} - P_{t|t-1} C_t^{\mathsf{T}} \left(C_t P_{t|t-1} C_t^{\mathsf{T}} + R \right)^{-1} C_t P_{t|t-1}, \tag{2.11b}$$

with

$$\hat{y}_{t|t-1} = h(\hat{x}_{t|t-1}), \quad C_t = \left. \tfrac{\partial h_t(x_t)}{\partial x_t} \right|_{x_t = \hat{x}_{t|t-1}}. \tag{2.12}$$

Note that in (2.11) we have shifted our notation by one time step as compared to the notation in (2.9) to avoid cluttering the notation. The measurement update is often expressed in terms of the Kalman gain K_t, the residual ε_t and the residual covariance S_t

$$\varepsilon_t = y_t - \hat{y}_{t|t-1}, \quad S_t = C_t P_{t|t-1} C_t^{\mathsf{T}} + R, \quad K_t = P_{t|t-1} C_t^{\mathsf{T}} S_t^{-1}. \tag{2.13}$$

The EKF iteratively performs a time update and a measurement update to estimate the state and the state covariance.

Design choices in the EKF are the choice of the state and of the dynamic and the measurement models. In Sections 2.2.2 – 2.2.4 we will focus on these design choices for the case of orientation estimation using inertial sensors and magnetometers. Hence, we will focus on the derivation of the models, the choice of the state x and the derivation of the corresponding $f_t(\,\cdot\,)$, $h_t(\,\cdot\,)$, A_t, C_t, and G_t.

2.2.2 Modeling the orientation estimation problem

In this section we consider the problem of estimating orientation using inertial sensors and magnetometers. We use a measurement model where the gyroscope measurements $y_{\omega,t}$ are modeled as (Titterton and Weston, 1997)

$$y_{\omega,t} = \omega_t + e_{\omega,t}, \tag{2.14}$$

where ω_t denotes the angular velocity and $e_{\omega,t} \sim \mathcal{N}(0, \Sigma_\omega)$. For simplicity we assume that the gyroscope measurements are bias-free.

The accelerometer measurements $y_{\mathrm{a},t}$ are modeled as (Titterton and Weston, 1997)

$$\begin{aligned} y_{\mathrm{a},t} &= R_t^{\mathrm{bn}} \left(a_t^{\mathrm{n}} - g^{\mathrm{n}} \right) + e_{\mathrm{a},t} \\ &\approx -R_t^{\mathrm{bn}} g^{\mathrm{n}} + e_{\mathrm{a},t}, \end{aligned} \tag{2.15}$$

where $e_{\mathrm{a},t} \sim \mathcal{N}(0, \Sigma_{\mathrm{a}})$ and R_t^{bn} denotes the rotation from the navigation frame n to the body frame b at time t as described in Section 2.1. As discussed in Chapter 1, the accelerometer measures both the sensor's acceleration, denoted by a_t^{n} and the earth's gravity, denoted by g^{n}. In the case of using only inertial sensors and magnetometers to estimate the orientation, it is necessary to stabilize the inclination by assuming something about the sensor's acceleration. A possible model for this is to assume that the mean of the acceleration is zero, as in Paper C and Luinge (2002). In this section and in Paper A we use a simpler model, where it is assumed that the acceleration a_t^{n} is approximately zero for all t.

The magnetometer measurements $y_{\mathrm{m},t}$ are modeled as

$$y_{\mathrm{m},t} = R_t^{\mathrm{bn}} m^{\mathrm{n}} + e_{\mathrm{m},t}, \tag{2.16}$$

where $e_{\mathrm{m},t} \sim \mathcal{N}(0, \Sigma_{\mathrm{m}})$. The local magnetic field is denoted by m^{n}. It is assumed to be constant and its horizontal component is assumed to be in the direction of the local magnetic north.

As discussed in Gustafsson (2012), it is possible to use the gyroscope measurements either as an input to the dynamic equation (2.8a) or as a measurement in (2.8b). In this thesis, we use an estimate of the angular velocity as a motion model for the orientation, i.e. we use the gyroscope measurements as an input to (2.8a). The noise v_t in (2.8a) hence represents the measurement noise of the gyroscope.

2.2.3 Quaternion states

Using the model from Section 2.2.2, we will now derive an EKF to estimate the orientation using quaternions as a state vector. The state-space model (recall (2.8)) is for this case given by

$$q_{t+1}^{\mathrm{nb}} = f_t(q_t^{\mathrm{nb}}, y_{\omega,t}, e_{\omega,t}), \tag{2.17a}$$

$$y_t = h_t(q_t^{\mathrm{nb}}) + e_t, \tag{2.17b}$$

where $e_{\omega,t} \sim \mathcal{N}(0, \Sigma_\omega)$ and $e_t \sim \mathcal{N}(0, R)$. The measurement model uses the accelerometer and magnetometer measurement models (2.15) and (2.16).

The dynamic equation is given by (Gustafsson, 2012; Törnqvist, 2008)

$$\begin{aligned} q_{t+1}^{\mathrm{nb}} &= \exp\left(-\tfrac{T}{2} S(\omega_t)\right) q_t^{\mathrm{nb}} && (2.18\mathrm{a}) \\ &\approx \left(\mathcal{I}_4 + \tfrac{T}{2} S(\omega_t)\right) q_t^{\mathrm{nb}} && (2.18\mathrm{b}) \\ &= \left(\mathcal{I}_4 + \tfrac{T}{2} S(\hat{\omega}_t)\right) q_t^{\mathrm{nb}} + \tfrac{T}{2} \bar{S}(q_t^{\mathrm{nb}}) v_t, && (2.18\mathrm{c}) \end{aligned}$$

where exp denotes the matrix exponential, T denotes the sampling time and

$$\hat{\omega}_t = y_{\omega,t} = \omega_t + e_{\omega,t}. \tag{2.19}$$

The matrices $\bar{S}(q)$ and $S(\omega)$ are given by

$$\bar{S}(q) = \begin{pmatrix} -q_1 & -q_2 & -q_3 \\ q_0 & -q_3 & q_2 \\ q_3 & q_0 & -q_1 \\ -q_2 & q_1 & q_0 \end{pmatrix}, \quad S(\omega) = \begin{pmatrix} 0 & -\omega_1 & -\omega_2 & -\omega_3 \\ \omega_1 & 0 & \omega_3 & -\omega_2 \\ \omega_2 & -\omega_3 & 0 & \omega_1 \\ \omega_3 & \omega_2 & -\omega_1 & 0 \end{pmatrix}. \tag{2.20}$$

To obtain (2.18b), a first order approximation is used. Subsequently, (2.18c) is obtained using the gyroscope measurement model (2.14). Note that without loss of generality we have changed the sign in front of the zero-mean Gaussian noise-term in (2.14).

The state-space model (2.8) used to obtain the basic EKF equations, is therefore more explicitly given in terms of its dynamic equation (2.18) and its measure-

Algorithm 1 EKF estimating orientation using quaternion states

1. Time update

$$\hat{q}^{\mathrm{nb}}_{t+1|t} = \exp\left(-\tfrac{T}{2} S(\hat{\omega}_t)\right) \hat{q}^{\mathrm{nb}}_{t|t}, \tag{2.21a}$$

$$P_{t+1|t} = A_t P_{t|t} A_t^{\mathsf{T}} + G_t Q G_t^{\mathsf{T}}, \tag{2.21b}$$

with

$$A_t = \mathcal{I}_4 + \tfrac{T}{2} S(\hat{\omega}_t), \quad G_t = \tfrac{T}{2} \bar{S}(\hat{q}^{\mathrm{nb}}_t), \quad Q = \Sigma_\omega.$$

2. Measurement update

$$\hat{q}^{\mathrm{nb}}_{t|t} = \hat{q}^{\mathrm{nb}}_{t|t-1} + P_{t|t-1} C_t^{\mathsf{T}} \left(C_t P_{t|t-1} C_t^{\mathsf{T}} + R\right)^{-1} \left(y_t - \hat{y}_{t|t-1}\right), \tag{2.22a}$$

$$P_{t|t} = P_{t|t-1} - P_{t|t-1} C_t^{\mathsf{T}} \left(C_t P_{t|t-1} C_t^{\mathsf{T}} + R\right)^{-1} C_t P_{t|t-1}, \tag{2.22b}$$

with

$$\hat{y}_{t|t-1} = \begin{pmatrix} -\hat{R}^{\mathrm{bn}}_{t|t-1} g^{\mathrm{n}} \\ \hat{R}^{\mathrm{bn}}_{t|t-1} m^{\mathrm{n}} \end{pmatrix}, \quad C_t = \begin{pmatrix} -\left.\frac{\partial R^{\mathrm{bn}}_{t|t-1}}{\partial q^{\mathrm{nb}}_{t|t-1}}\right|_{q^{\mathrm{nb}}_{t|t-1} = \hat{q}^{\mathrm{nb}}_{t|t-1}} g^{\mathrm{n}} \\ \left.\frac{\partial R^{\mathrm{bn}}_{t|t-1}}{\partial q^{\mathrm{nb}}_{t|t-1}}\right|_{q^{\mathrm{nb}}_{t|t-1} = \hat{q}^{\mathrm{nb}}_{t|t-1}} m^{\mathrm{n}} \end{pmatrix}, \quad R = \begin{pmatrix} \Sigma_{\mathrm{a}} & 0 \\ 0 & \Sigma_{\mathrm{m}} \end{pmatrix}.$$

3. Renormalize the quaternion $\hat{q}^{\mathrm{nb}}_{t|t}$.

ment models (2.15) and (2.16). Using the results from Section 2.2.1, the EKF implementation for estimating orientation using quaternion states can be derived. It is given in Algorithm 1. Note that to avoid cluttering notation, the time indices are again shifted between the time and the measurement update.

Due to the norm 1 constraint of the quaternions, we expect the state covariance matrix P in Algorithm 1 to be rank deficient. Due to linearization, however, the matrix P in the EKF is typically not rank deficient. Hence, the actual interpretation of the covariance matrix is problematic. To avoid problems with a rank deficient state covariance matrix, in Section 2.2.4 we will derive a different EKF implementation.

2.2.4 Orientation error states

A second possible EKF implementation makes use of a 3-dimensional state vector η_t representing the orientation deviation from a linearization point $\tilde{q}^{\mathrm{nb}}_t$. This EKF implementation is sometimes referred to as a multiplicative EKF (MEKF) (Crassidis et al., 2007; Markley, 2003). Its derivation is slightly more involved than the one using quaternions. However, its implementation is computationally attractive since it only uses a 3-dimensional state (compared to the 4-dimensional state in Section 2.2.3). Furthermore, the interpretation of the state covariance is more intuitive since it is not expected to be rank-deficient as was the case for the quaternion implementation.

The linearization point $\tilde{q}^{\mathrm{nb}}_t$ is encoded using a unit quaternion. Defining without loss of generality[1] that the orientation deviation is in the body frame b, the ori-

---

[1] A similar derivation can be done assuming an orientation deviation in the navigation frame n.

entation q_t^{nb} can be defined in terms of a linearization point $\tilde{q}_t^{\text{nb}}$ and the state η_t^{b} as

$$q_t^{\text{nb}} = \tilde{q}_t^{\text{nb}} \odot \delta q(\eta_t^{\text{b}}). \tag{2.23}$$

Here, $\odot$ denotes the quaternion multiplication defined as

$$p \odot q \triangleq \begin{pmatrix} p_0 q_0 - p_v \cdot q_v \\ p_0 q_v + q_0 p_v + p_v \times q_v \end{pmatrix}, \tag{2.24}$$

which can equivalently be written as the following matrix-vector multiplications

$$p \odot q = \underbrace{\begin{pmatrix} p_0 & -p_v^{\mathsf{T}} \\ p_v & p_0 \mathcal{I}_3 + [p_v \times] \end{pmatrix}}_{p^{\text{L}}} \begin{pmatrix} q_0 \\ q_v \end{pmatrix} = \underbrace{\begin{pmatrix} q_0 & -q_v^{\mathsf{T}} \\ q_v & q_0 \mathcal{I}_3 - [q_v \times] \end{pmatrix}}_{q^{\text{R}}} \begin{pmatrix} p_0 \\ p_v \end{pmatrix}. \tag{2.25}$$

The notation $\delta q(a)$ denotes the quaternion representation of a vector a according to

$$\delta q(a) = \begin{pmatrix} \cos \frac{\|a\|}{2} \\ \frac{a}{\|a\|} \sin \frac{\|a\|}{2} \end{pmatrix} \approx \begin{pmatrix} 1 \\ \frac{a}{2} \end{pmatrix}, \tag{2.26}$$

where the second equality uses a first order approximation, assuming that the vector a is small.

Based on (2.23), the dynamic and measurement models and the resulting EKF time and measurement update equations of the state η_t^{b} can be derived. In the remainder, the superscript b will be omitted for brevity.

Time update

To determine the EKF time update equations, we need to derive the dynamic equation

$$\eta_{t+1} = f_t\left(\eta_t, y_{\omega,t}, e_{\omega,t}\right). \tag{2.27}$$

To derive the dynamic model (2.27), we start from (2.23) for two different time steps

$$q_{t+1}^{\text{nb}} = \tilde{q}_{t+1}^{\text{nb}} \odot \delta q(\eta_{t+1}), \tag{2.28a}$$

$$q_t^{\text{nb}} = \tilde{q}_t^{\text{nb}} \odot \delta q(\eta_t). \tag{2.28b}$$

The dynamics of the orientation is defined in terms of the angular velocity ω_t as (see e.g. Shuster (1993); Hol (2011))

$$q_{t+1}^{\text{nb}} = q_t^{\text{nb}} \odot \delta q(T \omega_t), \tag{2.29}$$

where $\delta q(T\omega_t)$ is defined as in (2.26).

Comparing (2.28) and (2.29), we can use the gyroscope measurements to either update the linearization point $\tilde{q}_t^{\text{nb}}$ or to update the state η_t. Assuming that the gyroscope measurements are used to update the linearization point,

$$\tilde{q}^{\text{nb}}_{t+1} = \tilde{q}^{\text{nb}}_{t} \odot \delta q(T\hat{\omega}_t), \tag{2.30}$$

where $\hat{\omega}_t$ is defined in (2.19). Combining (2.28) – (2.30),

$$\begin{aligned}
\delta q(\eta_{t+1}) &= \left(\tilde{q}^{\text{nb}}_{t+1}\right)^{-1} \odot \tilde{q}^{\text{nb}}_{t} \odot \delta q(\eta_t) \odot \delta q(T\omega_t) \\
&= (\delta q(T\hat{\omega}_t))^{-1} \odot \delta q(\eta_t) \odot \delta q(T\omega_t) \\
&\approx \begin{pmatrix} 1 \\ -\frac{T}{2}\hat{\omega}_t \end{pmatrix}^{\text{L}} \begin{pmatrix} 1 \\ \frac{T}{2}\omega_t \end{pmatrix}^{\text{R}} \delta q(\eta_t) \\
&= \begin{pmatrix} 1 \\ -\frac{T}{2}\left(\omega_t + e_{\omega,t}\right) \end{pmatrix}^{\text{L}} \begin{pmatrix} 1 \\ \frac{T}{2}\omega_t \end{pmatrix}^{\text{R}} \delta q(\eta_t),
\end{aligned} \tag{2.31}$$

where we used the definition (2.25), the gyroscope measurement model (2.14) and the definition of the inverse quaternion as

$$q^{-1} = \begin{pmatrix} q_0 \\ -q_v \end{pmatrix}. \tag{2.32}$$

Note that in (2.32) we implicitly assume that the norm of the quaternion q is equal to one. For a more general definition, see e.g. Hol (2011); Törnqvist (2008). Defining

$$M \triangleq \begin{pmatrix} 1 \\ -\frac{T}{2}\left(\omega_t + e_{\omega,t}\right) \end{pmatrix}^{L} \begin{pmatrix} 1 \\ \frac{T}{2}\omega_t \end{pmatrix}^{R}, \tag{2.33}$$

and using the first-order approximation from (2.26), (2.31) can be written as

$$\begin{pmatrix} 1 \\ \frac{\eta_{t+1}}{2} \end{pmatrix} \approx M \begin{pmatrix} 1 \\ \frac{\eta_t}{2} \end{pmatrix}. \tag{2.34}$$

Hence, the dynamic model can be written as

$$\eta_{t+1} = f_t(\eta_t, y_{\omega,t}, e_{\omega,t}) \approx 2M_{21} + M_{22}\eta_t, \tag{2.35}$$

where M_{21} and M_{22} denote the $(2,1)$ and $(2,2)$ components of the matrix M, respectively, with

$$M_{21} = -\tfrac{T}{2}\left(\omega_t + e_{\omega,t}\right) + \left(\mathcal{I}_3 - \tfrac{T}{2}[(\omega_t + e_{\omega,t})\times]\right)\tfrac{T}{2}\omega_t, \tag{2.36a}$$

$$M_{22} = \tfrac{T^2}{4}\left(\omega_t + e_{\omega,t}\right)\omega_t^{\mathsf{T}} + \left(\mathcal{I}_3 - \tfrac{T}{2}[(\omega_t + e_{\omega,t})\times]\right)\left(\mathcal{I}_3 - \tfrac{T}{2}[\omega_t\times]\right). \tag{2.36b}$$

We assume that $\hat{\eta}_t = 0$ and hence that the EKF time update affects the linearization point directly, i.e. $\hat{\eta}_{t+1} = 0$ and

$$\hat{q}^{\text{nb}}_{t+1|t} = \hat{q}^{\text{nb}}_{t|t} \odot \delta q(T\hat{\omega}_t), \tag{2.37a}$$

$$P_{t+1|t} = A_t P_{t|t} A_t^{\mathsf{T}} + G_t Q G_t^{\mathsf{T}}, \tag{2.37b}$$

where $\hat{q}^{\text{nb}}_{t|t}$ denotes the EKF estimate of the linearization point and

$$\begin{aligned} A_t &= \left.\frac{\partial f_t(\eta_t, y_{\omega,t}, e_{\omega,t})}{\partial \eta_t}\right|_{\eta_t=\hat{\eta}_t, e_{\omega,t}=0} \\ &= \tfrac{T^2}{4}\hat{\omega}_t\hat{\omega}_t^{\mathsf{T}} + \left(\mathcal{I}_3 - \tfrac{T}{2}[\hat{\omega}_t\times]\right)\left(\mathcal{I}_3 - \tfrac{T}{2}[\hat{\omega}_t\times]\right) \\ &\approx \mathcal{I}_3 - T[\hat{\omega}_t\times], \end{aligned} \tag{2.38}$$

$$\begin{aligned} G_t &= \left.\frac{\partial f_t(\eta_t, y_{\omega,t}, e_{\omega,t})}{\partial e_{\omega,t}}\right|_{\eta_t=\hat{\eta}_{t|t}, e_{\omega,t}=0} \\ &= -T\mathcal{I}_3 + \tfrac{T^2}{4}[\hat{\omega}_t\times] \\ &\approx -T\mathcal{I}_3. \end{aligned} \tag{2.39}$$

Note that the approximations in (2.38) and (2.39) are not required, but are used for notational convenience.

Measurement update

In the measurement update of the EKF, the state η_t is updated using the accelerometer and magnetometer measurements. Hence, the measurement equations (2.15) and (2.16) need to be formulated in terms of the state η_t. For this, it is possible to write

$$\mathcal{R}(q^{\text{nb}}_t) = \mathcal{R}(\tilde{q}^{\text{nb}}_t \odot \delta q(\eta^{\text{b}}_t)) = \mathcal{R}(\tilde{q}^{\text{nb}}_t)\mathcal{R}(\delta q(\eta^{\text{b}}_t)), \tag{2.40}$$

where $\mathcal{R}(q)$ denotes the rotation matrix representation of the quaternion q. Using the relation between a rotation matrix and a quaternion (2.4) and the first order approximation (2.26) of the quaternion describing the orientation error,

$$\begin{aligned} \mathcal{R}(\delta q(\eta^{\text{b}}_t)) &= (\delta q)_v\,(\delta q)_v^{\mathsf{T}} + \delta q_0^2\mathcal{I}_3 + 2\delta q_0[(\delta q)_v\times] + [(\delta q)_v\times]^2 \\ &= \tfrac{\eta_t\eta_t^{\mathsf{T}}}{4} + \mathcal{I}_3 + [\eta_t\times] + \tfrac{1}{4}[\eta_t\times]^2 \\ &\approx \mathcal{I}_3 + [\eta_t\times], \end{aligned} \tag{2.41}$$

where for notational simplicity we have omitted the explicit dependence of δq on η^{b}_t and the superscript b on the η_t.

Using (2.40) and (2.41), the accelerometer measurement equation (2.15) can be written in terms of the state η^{b}_t as

$$\begin{aligned} y_{\text{a},t} &= \left(\mathcal{R}(q^{\text{nb}}_t)\right)^{\mathsf{T}}(a^{\text{n}}_t - g^{\text{n}}) + e_{\text{a},t} \\ &\approx -\left(\mathcal{R}(q^{\text{nb}}_t)\right)^{\mathsf{T}} g^{\text{n}} + e_{\text{a},t} \\ &= -\left(\mathcal{R}(\delta q(\eta^{\text{b}}_t))\right)^{\mathsf{T}}\left(\mathcal{R}(\tilde{q}^{\text{nb}}_t)\right)^{\mathsf{T}} g^{\text{n}} + e_{\text{a},t} \\ &\approx -\left(\mathcal{I}_3 - [\eta^{\text{b}}_t\times]\right)\tilde{R}^{\text{bn}}_t g^{\text{n}} + e_{\text{a},t} \\ &= -\tilde{R}^{\text{bn}}_t g^{\text{n}} - [\tilde{R}^{\text{bn}}_t g^{\text{n}}\times]\eta^{\text{b}}_t + e_{\text{a},t}, \end{aligned} \tag{2.42}$$

where $\tilde{R}^{\text{bn}}_t$ is the rotation matrix representation of $\tilde{q}^{\text{bn}}_t$.

The magnetometer measurement equation (2.16) can be written in terms of the state η_t^{b} as

$$\begin{aligned} y_{\mathrm{m},t} &= \mathcal{R}(q_t^{\mathrm{nb}})^{\mathsf{T}} m^{\mathrm{n}} + e_{\mathrm{m},t} \\ &= \mathcal{R}(\delta q(\eta_t^{\mathrm{b}}))^{\mathsf{T}} \left(\mathcal{R}(\tilde{q}_t^{\mathrm{nb}})\right)^{\mathsf{T}} m^{\mathrm{n}} + e_{\mathrm{m},t} \\ &\approx \left(\mathcal{I}_3 - [\eta_t^{\mathrm{b}} \times]\right) \tilde{R}_t^{\mathrm{bn}} m^{\mathrm{n}} + e_{\mathrm{m},t} \\ &= \tilde{R}_t^{\mathrm{bn}} m^{\mathrm{n}} - [\eta_t^{\mathrm{b}} \times] \tilde{R}_t^{\mathrm{bn}} m^{\mathrm{n}} + e_{\mathrm{m},t} \\ &= \tilde{R}_t^{\mathrm{bn}} m^{\mathrm{n}} + [\tilde{R}_t^{\mathrm{bn}} m^{\mathrm{n}} \times] \eta_t^{\mathrm{b}} + e_{\mathrm{m},t}. \end{aligned} \tag{2.43}$$

The EKF measurement update equations can hence be written as

$$\hat{\eta}_t = P_{t|t-1} C_t^{\mathsf{T}} \left(C_t P_{t|t-1} C_t^{\mathsf{T}} + R\right)^{-1} \left(y_t - \hat{y}_{t|t-1}\right), \tag{2.44a}$$

$$\tilde{P}_{t|t} = P_{t|t-1} - P_{t|t-1} C_t^{\mathsf{T}} \left(C_t P_{t|t-1} C_t^{\mathsf{T}} + R\right)^{-1} C_t P_{t|t-1}, \tag{2.44b}$$

with

$$\begin{aligned} y_t &= \begin{pmatrix} y_{\mathrm{a},t} \\ y_{\mathrm{m},t} \end{pmatrix}, \quad \hat{y}_{t|t-1} = \begin{pmatrix} -\hat{R}_{t|t-1}^{\mathrm{bn}} g^{\mathrm{n}} \\ \hat{R}_{t|t-1}^{\mathrm{bn}} m^{\mathrm{n}} \end{pmatrix}, \\ C_t &= \begin{pmatrix} -[\hat{R}_{t|t-1}^{\mathrm{bn}} g^{\mathrm{n}} \times] & [\hat{R}_{t|t-1}^{\mathrm{bn}} m^{\mathrm{n}} \times] \end{pmatrix}. \end{aligned} \tag{2.45}$$

Note that we do not use a double subscript for the state $\hat{\eta}_t$ since the state is not updated in the time update of the filter. The covariance after the measurement update is denoted as $\tilde{P}_{t|t}$ since $P_{t|t}$ will be determined in the subsequent relinearization step.

Relinearization

After the measurement update, the orientation deviation $\hat{\eta}_t$ is non-zero. In obtaining the EKF time update equations, however, we assumed that the state η_t was equal to zero. Hence, to not violate this assumption, we need to update the linearization point and reset the state after the measurement update. In our algorithm, we consider the relinearization as the "measurement update" for the linearization point, i.e. we assume that we update the estimate of the linearization point $\hat{q}_{t|t-1}^{\mathrm{nb}}$ to $\hat{q}_{t|t}^{\mathrm{nb}}$.

Defining the reset state as χ_t, we model the relinearization as

$$\chi_t = g_t(\eta_t). \tag{2.46}$$

Note the similarity with the EKF time update. Similar to the dynamic model $f_t(\,\cdot\,)$ we now have a function $g_t(\,\cdot\,)$ relating the current linearization point η_t to a new linearization point χ_t. The two linearization points are related by

$$\hat{q}_{t|t}^{\mathrm{nb}} \odot \delta q(\chi_t) = \hat{q}_{t|t-1}^{\mathrm{nb}} \odot \delta q(\eta_t). \tag{2.47}$$

and hence

$$\delta q(\chi_t) = \underbrace{\left(\hat{q}^{\text{nb}}_{t|t}\right)^{-1} \odot \hat{q}^{\text{nb}}_{t|t-1}}_{\triangleq (\delta q(a))^{-1}} \odot \delta q(\eta_t). \tag{2.48}$$

Assuming that χ, η and a are small, we can use the first-order approximation (2.26) and rewrite (2.48) as

$$\begin{pmatrix} 1 \\ \frac{\chi_t}{2} \end{pmatrix} = \begin{pmatrix} 1 \\ -\frac{a}{2} \end{pmatrix}^{\mathsf{L}} \begin{pmatrix} 1 \\ \frac{\eta_t}{2} \end{pmatrix}, \tag{2.49}$$

and the relinearization model can be written as

$$\chi_t = g_t(\eta_t) \approx -a + \left(\mathcal{I}_3 - \tfrac{1}{2}[a\times]\right)\eta_t. \tag{2.50}$$

Hence, the Jacobian of the relinearization can be determined as

$$J_t = \left.\frac{\partial g_t(\eta_t)}{\partial \eta_t}\right|_{\eta_t=\hat{\eta}_t} \approx \mathcal{I}_3 - \tfrac{1}{2}[a\times]. \tag{2.51}$$

Since the relinearization step is used to reset the state, we choose $\hat{\chi}_t = \begin{pmatrix} 0 & 0 & 0 \end{pmatrix}^{\mathsf{T}}$, i.e. $a = \hat{\eta}_t$. This leads to the following relinearization equations

$$\hat{q}^{\text{nb}}_{t|t} = \hat{q}^{\text{nb}}_{t|t-1} \odot \delta q(\hat{\eta}_t), \tag{2.52a}$$

$$P_{t|t} = J_t \tilde{P}_{t|t} J_t^{\mathsf{T}}, \quad J_t = \mathcal{I}_3 - \tfrac{1}{2}[\hat{\eta}_t\times]. \tag{2.52b}$$

The resulting EKF is summarized in Algorithm 2.

2.3 Smoothing

An alternative approach to obtain a MAP estimate of the state is to solve the problem (1.2) as a smoothing problem. Using such an approach, an estimate of the state vector $x_{1:N}$ using the measurements $y_{1:N}$ is obtained for instance using nonlinear optimization techniques (Boyd and Vandenberghe, 2004; Nocedal and Wright, 2006).

Optimization problems iteratively compute a smoothing estimate $\hat{x}_{1:N}$. An advantage of solving the state estimation problem using an optimization approach is that a relinearization is done after each iteration in the optimization problem. Hence, optimization problems can better handle nonlinearities than an EKF. It is also possible to include for instance constraints or non-Gaussian noise assumptions in the optimization problem.

The representation of the orientation in terms of an orientation deviation from a linearization point is particularly suitable for a smoothing implementation because of its low state dimension. Also, it does not require imposing a norm 1 constraint as is the case for quaternions.

As will be discussed in more detail in Chapter 3, solving optimization problems

Algorithm 2 EKF with orientation error states

1. Time update

$$\hat{q}^{\text{nb}}_{t+1|t} = \tilde{q}^{\text{nb}}_{t|t} \odot \delta q(T\hat{\omega}_t), \tag{2.53a}$$

$$P_{t+1|t} = A_t P_{t|t} A_t^{\mathsf{T}} + GQG^{\mathsf{T}}, \tag{2.53b}$$

with

$$A_t = I_3 - T[\hat{\omega}_t \times], \quad G = T\mathcal{I}_3, \quad Q = \Sigma_\omega.$$

2. Measurement update

$$\hat{\eta}_t = P_{t|t-1} C_t^{\mathsf{T}} \left(C_t P_{t|t-1} C_t^{\mathsf{T}} + R \right)^{-1} \left(y_t - \hat{y}_{t|t-1} \right) \tag{2.54a}$$

$$\tilde{P}_{t|t} = P_{t|t-1} - P_{t|t-1} C_t^{\mathsf{T}} \left(C_t P_{t|t-1} C_t^{\mathsf{T}} + R \right)^{-1} C_t P_{t|t-1}, \tag{2.54b}$$

with

$$y_t = \begin{pmatrix} y_{\text{a},t} \\ y_{\text{m},t} \end{pmatrix}, \quad \hat{y}_{t|t-1} = \begin{pmatrix} -\hat{R}^{\text{bn}}_{t|t-1} g^{\text{n}} \\ \hat{R}^{\text{bn}}_{t|t-1} m^{\text{n}} \end{pmatrix},$$

$$C_t = \begin{pmatrix} -[\hat{R}^{\text{bn}}_{t+1|t} g^{\text{n}} \times] & [\hat{R}^{\text{bn}}_{t+1|t} m^{\text{n}} \times] \end{pmatrix}, \quad R = \begin{pmatrix} \Sigma_{\text{a}} & 0 \\ 0 & \Sigma_{\text{m}} \end{pmatrix}.$$

3. Relinearize

$$\hat{q}^{\text{nb}}_{t|t} = \hat{q}^{\text{nb}}_{t|t-1} \odot \begin{pmatrix} \cos \frac{\|\hat{\eta}_t\|}{2} \\ \frac{\hat{\eta}_t}{\|\hat{\eta}_t\|} \sin \frac{\|\hat{\eta}_t\|}{2} \end{pmatrix}, \tag{2.55a}$$

$$P_{t|t} = J_t \tilde{P}_{t|t} J_t^{\mathsf{T}}, \tag{2.55b}$$

with

$$J_t = \mathcal{I}_3 - \tfrac{1}{2}[\hat{\eta}_t \times].$$

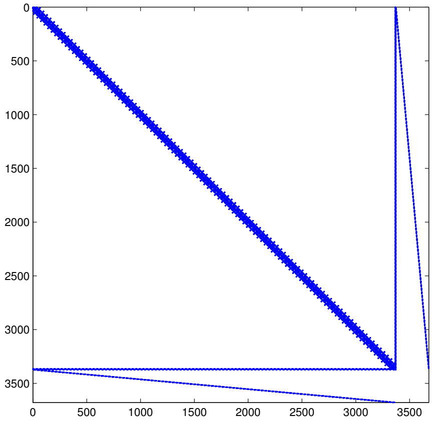

Figure 2.2: *Sparseness pattern of the matrix that needs to be inverted to solve the motion capture problem in Paper C. The parts of the matrix that are non-zero are depicted in blue. The diagonal line represents the non-zero elements due to the dynamic and measurement models. The horizontal and vertical lines represent the sensor biases which we modeled as constants. The outermost diagonal lines represent the constraints based on the assumption that the body segments remain attached to each other at all times. Only* 0.56% *of the elements in the matrix are non-zero.*

typically involves inversion of a matrix. For smoothing applications, this matrix grows with the number of measurements $y_{1:N}$ and the number of states $x_{1:N}$ and can hence be of fairly large dimension. Due to the specific structure of the state-space models, however, the number of non-zero elements in the matrix is typically relatively small, i.e. the matrix is sparse. This is because the state is modeled only in terms of the state at the previous time. Matrices that are sparse, and specifically matrices whose non-zero elements are ordered according to certain patterns, can be inverted efficiently (Boyd and Vandenberghe, 2004).

In Paper C we use an optimization approach to solve an inertial motion capture problem. It estimates the body's 6D pose using information from a number of sensors attached to the body. The inertial measurements from these sensors are combined with the assumption that the body segments remain attached to each other at all times. This leads to a large optimization problem. However, as illustrated in Figure 2.2, the matrix that needs to be inverted to solve the optimization problem is very sparse and structured and can hence be inverted efficiently.

2.4 Particle filters

An alternative state estimation technique is the *particle filter* (PF) (Gordon et al., 1993; Doucet and Johansen, 2011). Contrary to EKFs, PFs do not rely on a linear approximation of the dynamic and measurement functions in the state-space model. Hence, they can successfully be used for state estimation using nonlinear models. PFs use N particles to represent different hypotheses as

$$\hat{p}^N(x_t \mid y_{1:t}) = \sum_{t=1}^{N} w_t^i \delta_{x_t^i}(x_t), \tag{2.56}$$

where w_t^i denotes the weight of particle i at time t. In case the state-space model contains a conditionally linear Gaussian substructure, a *Rao-Blackwellized particle filter* (RBPF) (Schön et al., 2005) can be used instead. The RBPF treats the conditionally linear states using a KF, thereby reducing the dimension of the state vector used in the PF.

In this section we will not give a general description of a particle filter. Good descriptions can be found in for instance Doucet and Johansen (2011). Instead, we focus on two subproblems of relevance to Paper D. In Section 2.4.1 we will discuss the problem of using a PF to represent the state in a partially unobservable state-space model. In Section 2.4.2 we will discuss how a point estimate can be obtained from a PF describing a multimodal distribution.

2.4.1 Representing a circle of possible sensor positions

In Paper D, we use an RBPF to estimate the sensor's position and orientation using the magnetic field induced by a magnetic coil as a source of position information. Since the magnetic field strength is proportional to the distance to the coil, information about the magnetic field strength leads to information about the distance of the sensor to the coil. Hence, a sphere of possible position estimates is obtained. Based on the assumption that the inclination is known from the accelerometer measurements and assuming that the sensor is above the coil, the possible positions are reduced to a circle. Hence, the state-space model can be said to be unobservable, with the unobservable space in the shape of a circle. Although you would theoretically expect the particles in a PF to represent the unobservable space, i.e. you would expect a circle of particles, in practice this is not the case for a finite number of particles, as illustrated in Example 2.1.

Example 2.1: Particle filter estimating a partially unobservable state

Consider the following state-space model

$$x_{t+1} = x_t + v_t, \tag{2.57a}$$

$$y_t = \sqrt{x_{t,1}^2 + x_{t,2}^2} + e_t, \tag{2.57b}$$

where x_t is a 2-dimensional state and $x_{t,i}$ denotes the i^{th} component of x_t. We model $v_t \sim \mathcal{N}(0, Q)$ and $e_t \sim \mathcal{N}(0, R)$. For our simulations we choose $Q = 1 \times 10^{-4}\mathcal{I}_2$ and $R = 1 \times 10^{-4}$ and we use $N = 500$ particles.

According to the dynamic model (2.57a), the state x_t remains approximately constant. The measurement model (2.57b) provides information about the state x_t, but any position on a circle with radius y_t is equally likely. Hence, if we initialize the particles on a circle as in the left plot in Figure 2.3, we would expect the parti-

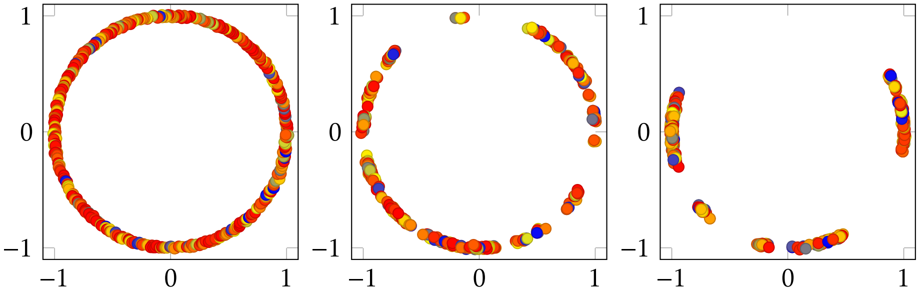

Figure 2.3: *Particles of the* PF *used to estimate the state x_t in Example 2.1. Left: the particles at $t = 1$. The colors indicate the particles' weights. Middle: the particles at $t = 50$. Right: particles at $t = 500$.*

cles to remain spread out over the circle. However, as depicted in the middle and right plots in Figure 2.3, as time progresses, the particles start clustering more and more on parts of the circle. How soon this clustering happens depends for instance on the particular choices of Q, R and the number of particles N.

Note that although in Example 2.1 the particles at later time steps do not represent the whole circle, they do still give good estimates of *a* solution. The hypotheses only don't include *all* solutions. The problem illustrated in Example 2.1 is a special case of particle degeneracy. As discussed in Lindsten (2013), after a certain time all particles will share a common ancestor at $t = 1$. This results in all particles being clustered at one part of the circle.

2.4.2 Obtaining a point estimate

A particle filter uses N particles and weights to represent the filtering density. Each particle is assigned a weight w indicating how likely this hypothesis is. In practice, however, one often wants to represent the estimated state as a point estimate. For this, the weighted mean of the particles is commonly used. As argued in Driessen and Boers (2008); Saha et al. (2009), for some applications the weighted mean is not the most informative point estimate. An important example of this are multi-modal distributions where the point estimate based on the weighted mean is uninformative. For the Example 2.1, the weighted mean at the initial time point is clearly uninformative, since it is the circle's origin. Driessen and Boers (2008); Saha et al. (2009) therefore derive a MAP estimate for the particle filter, a so-called PF-MAP. Saha et al. (2013) derives a MAP estimate for a particle smoother. In Paper D we determine the position and orientation of an IMU in a magnetically disturbed environment using an RBPF. To determine a MAP estimate for the RBPF, the definition of the PF-MAP estimate needs to be extended. We will therefore in this section first introduce the PF-MAP as derived by Driessen and Boers (2008); Saha et al. (2009). Subsequently, we will introduce the RBPF-MAP. We use this RBPF-MAP in Paper D to determine a point estimate of the estimated sensor position to compare this to estimates from an optical reference system.

PF-MAP

In this section we will summarize the derivation of the PF-MAP introduced in Driessen and Boers (2008); Saha et al. (2009). The PF-MAP obtains a MAP estimate of the state at each time instance from the particles in the PF. The MAP estimate is defined as

$$\hat{x}_{t|t}^{\text{MAP}} = \arg\max_{x_t} \; p(x_t \mid y_{1:t}), \tag{2.58}$$

i.e. it maximizes the posterior (filtering) density. Using Bayes' rule and the Markov property, this posterior density can be written as

$$p(x_t \mid y_{1:t}) = \frac{p(y_t \mid x_t)p(x_t \mid y_{1:t-1})}{p(y_t \mid y_{1:t-1})} \propto p(y_t \mid x_t)p(x_t \mid y_{1:t-1}), \tag{2.59}$$

where the denominator can be neglected since it is independent of x_t. The MAP estimate can hence be written as

$$\hat{x}_{t|t}^{\text{MAP}} = \arg\max_{x_t} \; p(y_t \mid x_t)p(x_t \mid y_{1:t-1}). \tag{2.60}$$

The predictive density $p(x_t \mid y_{1:t-1})$ can be rewritten through marginalization as

$$p(x_t \mid y_{1:t-1}) = \int p(x_t \mid x_{t-1})p(x_{t-1} \mid y_{1:t-1}) \, dx_{t-1}. \tag{2.61}$$

This density is in the particle filter approximated as

$$p(x_t \mid y_{1:t-1}) \approx \sum_{j=1}^{N} p(x_t \mid x_{1:t-1}^j) w_{t-1}^j, \tag{2.62}$$

where w_{t-1}^j denotes the weight of particle j at time $t-1$. The MAP estimate can be obtained by substituting (2.62) into (2.60)

$$\hat{x}_{t|t}^{\text{MAP}} = \arg\max_{x_t} \; p(y_t \mid x_t) \sum_{j=1}^{N} p(x_t \mid x_{1:t-1}^j) w_{t-1}^j. \tag{2.63}$$

To obtain the MAP estimate, (2.63) can be solved using optimization techniques as discussed in e.g. Boyd and Vandenberghe (2004); Nocedal and Wright (2006). An alternative is to use the PF-MAP. It approximates the MAP estimate as

$$\hat{x}_{t|t}^{\text{PF-MAP}} = \arg\max_{x_t^i} \; p(y_t \mid x_t^i) \sum_{j=1}^{N} p(x_t^i \mid x_{1:t-1}^j) w_{t-1}^j, \tag{2.64}$$

i.e. it selects the particle with the highest density. Note that computation of the PF-MAP estimate is of the order of N^2 and it is hence quite expensive.

RBPF-MAP

An RBPF splits the state vector in (2.8) into a nonlinear state x_t^{n} and a conditionally linear state x_t^{l} as

$$
\begin{aligned}
x_{t+1}^{\mathrm{n}} &= f_t^{\mathrm{n}}(x_t^{\mathrm{n}}) + A_t^{\mathrm{n}}(x_t^{\mathrm{n}})x_t^{\mathrm{l}} + v_t^{\mathrm{n}}, && \text{(2.65a)}\\
x_{t+1}^{\mathrm{l}} &= f_t^{\mathrm{l}}(x_t^{\mathrm{n}}) + A_t^{\mathrm{l}}(x_t^{\mathrm{n}})x_t^{\mathrm{l}} + v_t^{\mathrm{l}}, && \text{(2.65b)}\\
y_t &= h_t(x_t^{\mathrm{n}}) + C_t(x_t^{\mathrm{n}})x_t^{\mathrm{l}} + e_t, && \text{(2.65c)}
\end{aligned}
$$

with $Q = \begin{pmatrix} Q^{\mathrm{nn}} & Q^{\mathrm{nl}} \\ \left(Q^{\mathrm{nl}}\right)^{\mathsf{T}} & Q^{\mathrm{ll}} \end{pmatrix}$. Note that for notational simplicity we here consider a slightly less general model than in (2.8). Note also that in this section we will switch notation from the rest of the chapter and use the superscript n for "nonlinear" instead of "navigation frame". In this section we will derive the MAP for the RBPF in a similar way as the PF-MAP was derived in the previous section.

Following (2.58)–(2.60), and explicitly introducing the nonlinear and linear states,

$$
x_t = \begin{pmatrix} x_t^{\mathrm{n}} \\ x_t^{\mathrm{l}} \end{pmatrix}, \tag{2.66}
$$

the MAP estimate can be written as

$$
\begin{aligned}
\hat{x}_{t|t}^{\mathrm{MAP}} &= \underset{x_t^{\mathrm{n}}, x_t^{\mathrm{l}}}{\arg\max}\; p(x_t^{\mathrm{n}}, x_t^{\mathrm{l}} \mid y_{1:t}) \\
&= \underset{x_t^{\mathrm{n}}, x_t^{\mathrm{l}}}{\arg\max}\; p(y_t \mid x_t^{\mathrm{n}}, x_t^{\mathrm{l}}) p(x_t^{\mathrm{n}}, x_t^{\mathrm{l}} \mid y_{1:t-1}).
\end{aligned} \tag{2.67}
$$

The predictive density can for the case of a RBPF be rewritten as

$$
p(x_t^{\mathrm{n}}, x_t^{\mathrm{l}} \mid y_{1:t-1}) = \int p(x_t^{\mathrm{n}}, x_t^{\mathrm{l}} \mid x_{t-1}^{\mathrm{l}}, x_{t-1}^{\mathrm{n}}) p(x_{1:t-1}^{\mathrm{n}}, x_{t-1}^{\mathrm{l}} \mid y_{1:t-1})\, dx_{t-1}^{\mathrm{l}} dx_{1:t-1}^{\mathrm{n}}, \tag{2.68}
$$

where, using Bayes' rule,

$$
p(x_{1:t-1}^{\mathrm{n}}, x_{t-1}^{\mathrm{l}} \mid y_{1:t-1}) = p(x_{t-1}^{\mathrm{l}} \mid x_{1:t-1}^{\mathrm{n}}, y_{1:t-1}) p(x_{1:t-1}^{\mathrm{n}} \mid y_{1:t-1}). \tag{2.69}
$$

Here,

$$
p(x_{t-1}^{\mathrm{l}} \mid x_{1:t-1}^{\mathrm{n}}, y_{1:t-1}) = \mathcal{N}\left(x_{t-1}^{\mathrm{l}}; \hat{x}_{t-1|t-1}^{\mathrm{l}}(x_{1:t-1}^{\mathrm{n}}), P_{t-1|t-1}^{\mathrm{l}}(x_{1:t-1}^{\mathrm{n}})\right), \tag{2.70}
$$

and $p(x_{1:t-1}^{\mathrm{n}} \mid y_{1:t-1})$ can be recognized as the particles' weights. This leads to

$$
\begin{aligned}
p(x_t^{\mathrm{n}}, x_t^{\mathrm{l}} \mid y_{1:t-1}) \approx \sum_{j=1}^{N} \int & p(x_t^{\mathrm{n},j}, x_t^{\mathrm{l},j} \mid x_{t-1}^{\mathrm{l},j}, x_{t-1}^{\mathrm{n},j}) \\
& \mathcal{N}\left(x_{t-1}^{\mathrm{l}}; \hat{x}_{t-1|t-1}^{\mathrm{l},j}, P_{t-1|t-1}^{\mathrm{l},j}\right) w_{t-1}^{j}\, dx_{t-1}^{\mathrm{l}},
\end{aligned} \tag{2.71}
$$

where we have introduced short-hand notation

$$\hat{x}^{\mathrm{l},j}_{t-1|t-1} \triangleq \hat{x}^{\mathrm{l}}_{t-1|t-1}(x^{\mathrm{n},j}_{1:t-1}), \tag{2.72a}$$

$$P^{\mathrm{l},j}_{t-1|t-1} \triangleq P^{\mathrm{l}}_{t-1|t-1}(x^{\mathrm{n},j}_{1:t-1}). \tag{2.72b}$$

The integral is computed similarly to the time update in a Kalman filter, see e.g. Lindsten and Schön (2013); Törnqvist (2008); Gustafsson (2012),

$$p(x^{\mathrm{n}}_t, x^{\mathrm{l}}_t \mid y_{1:t-1}) \approx \sum_{j=1}^{N} w^j_{t-1} \mathcal{N}\left(x_t; \bar{x}^j_{t|t-1}, \bar{P}^j_{t|t-1}\right), \tag{2.73}$$

with

$$\bar{x}^j_{t|t-1} = \begin{pmatrix} f^{\mathrm{n}}_{t-1}(x^{\mathrm{n},j}_{t|t-1}) \\ f^{\mathrm{l}}_{t-1}(x^{\mathrm{n},j}_{t|t-1}) \end{pmatrix} + \begin{pmatrix} A^{\mathrm{n}}_{t-1}(x^{\mathrm{n},j}_{t|t-1}) \\ A^{\mathrm{l}}_{t-1}(x^{\mathrm{n},j}_{t|t-1}) \end{pmatrix} x^{\mathrm{l},j}_{t-1|t-1}, \tag{2.74a}$$

$$\bar{P}^j_{t|t-1} = \begin{pmatrix} A^{\mathrm{n}}_{t-1}(x^{\mathrm{n},j}_{t|t-1}) \\ A^{\mathrm{l}}_{t-1}(x^{\mathrm{n},j}_{t|t-1}) \end{pmatrix} P^j_{t-1|t-1} \begin{pmatrix} A^{\mathrm{n}}_{t-1}(x^{\mathrm{n},j}_{t|t-1}) \\ A^{\mathrm{l}}_{t-1}(x^{\mathrm{n},j}_{t|t-1}) \end{pmatrix}^{\mathsf{T}} + Q. \tag{2.74b}$$

Substituting (2.73) into (2.67), we obtain

$$\hat{x}^{\mathrm{MAP}}_{t|t} = \underset{x^{\mathrm{n}}_t, x^{\mathrm{l}}_t}{\arg\max}\; p(y_t \mid x^{\mathrm{n}}_t, x^{\mathrm{l}}_t) \sum_{j=1}^{N} w^j_{t-1} \mathcal{N}\left(x_t; \bar{x}^j_{t|t-1}, \bar{P}^j_{t|t-1}\right). \tag{2.75}$$

This can again be solved by any optimization technique, but it can also be solved approximately by optimizing over the finite set of particles, i.e.

$$\hat{x}^{\text{RBPF-MAP}}_{t|t} = \underset{x^{\mathrm{n},i}_t, x^{\mathrm{l},i}_t}{\arg\max}\; p(y_t \mid x^{\mathrm{n},i}_t, x^{\mathrm{l},i}_t) \sum_{j=1}^{N} w^j_{t-1} \mathcal{N}\left(x^i_t; \bar{x}^j_{t|t-1}, \bar{P}^j_{t|t-1}\right). \tag{2.76}$$

As can be seen, this is very similar to the PF-MAP results. This expression is used in Paper D.

3

Sensor calibration

In the pose estimation algorithms discussed in Chapter 2, we implicitly assumed that the sensors were properly calibrated. In this chapter, we will instead focus on the problem of sensor calibration. Hence, we will assume that our models contain unknown model parameters that need to be determined from data. The process of determining a model from data is commonly referred to as *system identification*. In our problems, we typically know the model structure but to calibrate the sensor, certain model/calibration parameters need to be estimated. This is called *grey-box system identification* (Bohlin, 2006).

We formulate the sensor calibration problem as an ML problem, where based on N measurements $y_{1:N} = \{y_1, \ldots, y_N\}$ we find the sensor calibration parameters θ that maximize the likelihood function (1.3). The ML problem (1.3) is repeated here for the reader's convenience,

$$\hat{\theta}^{\text{ML}} = \operatorname*{arg\,max}_{\theta \in \Theta} \; p_\theta(y_{1:N}), \tag{3.1}$$

where $\Theta \subseteq \mathbb{R}^{n_\theta}$. Using the fact that the logarithm is a monotonic function, (3.1) has the following equivalent formulation,

$$\hat{\theta}^{\text{ML}} = \operatorname*{arg\,min}_{\theta \in \Theta} \; -\log p_\theta(y_{1:N}). \tag{3.2}$$

An example of a sensor calibration problem is the magnetometer calibration problem which is the topic of Paper A. In this paper, we calibrate the magnetometer for the presence of magnetic disturbances rigidly attached to the sensor, for magnetometer sensor errors and for misalignment between the magnetometer and the inertial sensor axes. In Chapter 2 we modeled the magnetometer measurements $y_{\mathrm{m},t}$ as (2.16). For the reader's convenience, we repeat the model

$$y_{\mathrm{m},t} = R_t^{\mathrm{bn}} m^{\mathrm{n}} + e_{\mathrm{m},t}, \tag{3.3a}$$

where R_t^{bn} denotes the matrix rotating the local magnetic field m^{n} from the navigation frame n to the body frame b and $e_{\mathrm{m},t}$ is assumed to be Gaussian noise. The measurement model (3.3a) was discussed in more detail in Section 2.2.2. In Paper A, we instead model the magnetometer measurements as

$$y_{\mathrm{m},t} = D R_t^{\mathrm{bn}} m^{\mathrm{n}} + o + e_{\mathrm{m},t}, \tag{3.3b}$$

where D denotes the calibration matrix and o denotes the offset vector. The calibration matrix D and the offset vector o are both part of the parameter vector θ determined in the calibration algorithm presented in Paper A. When the model parameters D and o have been determined, they can be used to correct the magnetometer measurements, i.e. they can be used to calibrate the magnetometer. Without magnetometer calibration, the orientation estimation algorithms discussed in Chapter 2 give inaccurate heading estimates for instance when the magnetometer is attached to a metallic object.

In this chapter, we will provide background to the sensor calibration problems in Papers A and B. In Section 3.1, we will first discuss the nonlinear optimization techniques we use to solve our sensor calibration problems, i.e. to obtain ML estimates of the sensor calibration parameters. In Sections 3.2 and 3.3, we subsequently discuss two different cases of sensor calibration. In Section 3.2 we discuss parameter estimation in a static sensor model. In Section 3.3, we instead focus on obtaining an ML estimate of the sensor calibration parameters in a state-space model. In that case, it is necessary to know the state to estimate the sensor calibration parameters. Hence, both the state and the calibration parameters need to be estimated to calibrate the sensor.

3.1 Nonlinear optimization techniques

To obtain an ML estimate, an optimization problem is solved which finds a locally minimizing argument (3.2). The specific form of the minimization problem depends on the model assumptions. However, in general it can be said that the parameters are chosen such that they best describe the data. Hence, defining the predicted measurements to be $\hat{y}(\theta)$, we try to minimize the difference

$$\epsilon_t(\theta) = y_t - \hat{y}_t(\theta) \tag{3.4}$$

according to a criterion which is based on the PDF $p_\theta(y_{1:N})$. The function that needs to be minimized is denoted the cost function. Examples of cost functions can be found in Examples 3.1 and 3.2 for the cases of Gaussian and Cauchy distributed noise, respectively. The Cauchy distribution is a special case of the Student's-t distribution (Bishop, 2006). The Gaussian and Cauchy distributions will both be used in Part II of this thesis. More background about these distributions will be given in Section 3.2.

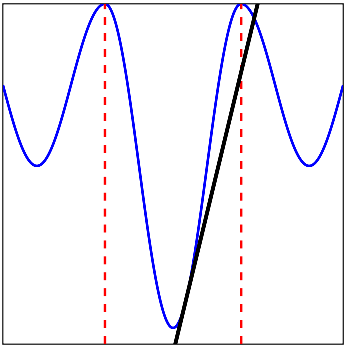

Figure 3.1: *Blue: example of a cost function with multiple local minima. Black: example gradient. If we use the gradient information to find a direction in which the function decreases, any starting point between the two red dashed lines will lead us to the global minimum.*

In our models, $\hat{y}_t$ typically depends nonlinearly on θ. Hence, our problems typically have multiple (local) minima and proper initialization of the optimization problem is of essence. An example of a cost function is depicted in Figure 3.1. Since we aim at minimizing the cost function, it can intuitively be understood that we want our algorithm to step in a direction in which the objective function decreases. Hence, gradient information can be used to find a search direction. The cost function in Figure 3.1 has one global minimum, but also has two other local minima. If we use the gradient information to find a direction in which the function decreases, any starting point between the two red dashed lines will lead us to the global minimum. Starting points outside these two lines, however, would lead us to one of the other local minima instead. Initialization is therefore important for our problems to converge to the desired minimum and considerable effort is put into obtaining good initial estimates in Papers A and B.

Optimization algorithms based on only gradient information typically converge very slowly (Nocedal and Wright, 2006). Hence, most algorithms make use of both the gradient and an (approximate) Hessian to find the step direction. The general structure of the optimization algorithms used in this thesis is summarized in Algorithm 3. They start from an initial estimate $\hat{\theta}_0$ and update their estimate $\hat{\theta}$ until convergence.

Different types of algorithms use different (approximate) Hessians in Algorithm 3. A first type are the Newton methods which use the exact Hessian. A second commonly used approach uses a positive definite approximation of the Hessian as in (3.7b) and (3.10b). A third approach are the quasi-Newton methods. Quasi-Newton methods estimate the Hessian based on the change of the gradient (Nocedal and Wright, 2006). Hence, they do not require the user to supply any analytical (approximate) Hessian. An example of a quasi-Newton method is the Broyden-Fletcher-Goldfarb-Shanno (BFGS) method which is used in Paper A to determine the magnetometer calibration parameters.

Example 3.1: Gaussian PDF with known and constant variance

For the scalar case of a Gaussian PDF with a known and constant variance σ^2

$$p_\theta(y_{1:N}) = \left(\frac{1}{\sqrt{2\pi\sigma^2}}\right)^N \exp\left(-\sum_{t=1}^{N} \frac{\epsilon_t^2}{2\sigma^2}\right), \tag{3.5}$$

with ϵ_t as defined in (3.4). Taking the logarithm of (3.5) and omitting constant terms, leads to the optimization problem

$$\hat{\theta}^{\mathrm{ML}} = \arg\min_{\theta\in\Theta} V(\theta) = \arg\min_{\theta\in\Theta} \tfrac{1}{2}\sum_{t=1}^{N} \epsilon_t^2. \tag{3.6}$$

Note that in our problems, (3.6) can not be solved explicitly since we assume that ϵ depends nonlinearly on θ. To solve the optimization problem (3.6) we typically need the gradient ∇V and an approximate Hessian H which in the case of a Gaussian are given by

$$\nabla V = \sum_{t=1}^{N} \epsilon_t \frac{\partial \epsilon_t}{\partial \theta}, \tag{3.7a}$$

$$H \approx \sum_{t=1}^{N} \left(\frac{\partial \epsilon_t}{\partial \theta}\right)^{\mathsf{T}} \frac{\partial \epsilon_t}{\partial \theta}. \tag{3.7b}$$

Example 3.2: Cauchy PDF with known and constant scale parameter

For the scalar case of a Cauchy PDF with a known and constant scale parameter γ,

$$p_\theta(y_{1:N}) = \prod_{t=1}^{N} \frac{1}{\pi\gamma^2}\left(1 + \left(\frac{\epsilon_t}{\gamma}\right)^2\right)^{-1}. \tag{3.8}$$

Taking the logarithm of (3.8) and omitting constant terms, leads to the optimization problem

$$\hat{\theta}^{\mathrm{ML}} = \arg\min_{\theta\in\Theta} V(\theta) = \arg\min_{\theta\in\Theta} \sum_{t=1}^{N} \log\left(1 + \left(\frac{\epsilon_t}{\gamma}\right)^2\right). \tag{3.9}$$

The gradient ∇V and a positive definite approximation of the Hessian are given by

$$\nabla V = \sum_{t=1}^{N} 2\frac{\frac{\partial \epsilon_t}{\partial \theta}\epsilon_t}{\gamma^2 + \epsilon_t^2}, \tag{3.10a}$$

$$H \approx \sum_{t=1}^{N} 2\frac{\left(\frac{\partial \epsilon_t}{\partial \theta}\right)^{\mathsf{T}} \frac{\partial \epsilon_t}{\partial \theta}}{\gamma^2 + \epsilon_t^2}. \tag{3.10b}$$

Algorithm 3 Obtaining an ML estimate

```
1. Find/choose an initial estimate $\hat{\theta}_0$
2. Set $i = 0$ and repeat,
    (a) Determine the gradient $\nabla V_i$ and the (approximate) Hessian $H_i$ of the cost function.
    (b) Determine a search direction $p$ according to,
            $p_i = -H_i^{-1} \nabla V_i.$   (3.11)
    (c) Determine a step length $\alpha_i$ and update $\hat{\theta}_i$
            $\hat{\theta}_{i+1} = \hat{\theta}_i + \alpha_i p_i.$   (3.12)
    (d) Set $i := i + 1$ and repeat from Step 2a until convergence.
```

3.2 Model parameters in the sensor models

In this section, we focus on determining model parameters in static sensor models. We model the measurements as

$$y_t = h_t(\theta) + e_t, \tag{3.13}$$

where $h_t(\,\cdot\,)$ is a possibly nonlinear function of the parameters θ and the noise e_t is assumed to be additive.

An example of such a model is used in Paper B where we model the UWB measurements as

$$y_{\mathrm{u},mk} = \tau_k + \|r_m^{\mathrm{n}} - t_k^{\mathrm{n}}\|_2 + \Delta\tau_m + e_{\mathrm{u},mk}, \tag{3.14}$$

where τ_k is the time of transmission of pulse k, t_k^{n} is the position of the transmitter at the time of transmitting the k^{th} pulse expressed in the navigation frame n, r_m^{n} is the position of the m^{th} receiver and $\Delta\tau_m$ is the clock-offset of the m^{th} receiver. The UWB calibration algorithm estimates the parameter vector θ, defined as

$$\theta = \left(\{t_k^{\mathrm{n}}, \tau_k\}_{k=1}^{K}, \{r_m^{\mathrm{n}}, \Delta\tau_m\}_{m=1}^{M}\right). \tag{3.15}$$

The choice of the noise distribution e_t in (3.13) influences the likelihood function in (3.1) and hence the optimization problem (3.2). The most commonly used noise model assumes that e_t is zero-mean Gaussian noise. The noise of the inertial sensors and the magnetometers can typically be assumed to be Gaussian (Titterton and Weston, 1997; Hol, 2011). Hence, the Gaussian cost function and its gradient and approximate Hessian as given in Example 3.1 are frequently used in Part II of this thesis.

For the UWB measurements considered in Paper B, however, we expect a small number of measurements to be delayed due to multipath and/or NLOS conditions. A Gaussian PDF is depicted in blue in the left plot in Figure 3.2. As can be seen, the likelihood far away from the mean is small and the log likelihood cost function (right plot) far away from the mean is large. Hence, the presence of outliers is not well described by a Gaussian distribution. In Paper B, we instead use a Cauchy distribution to allow for the presence of outliers. The Cauchy PDF

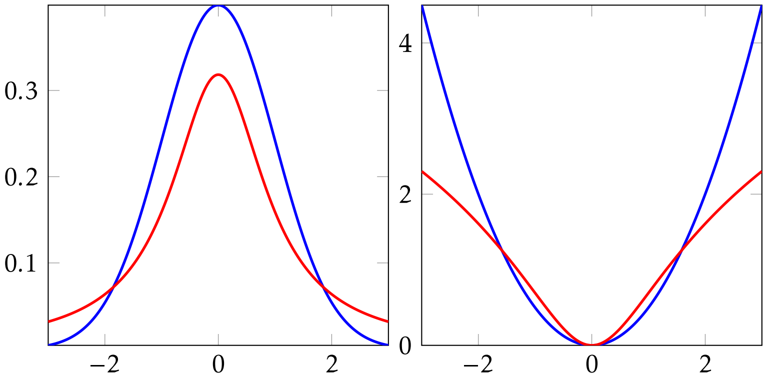

Figure 3.2: *Left:* PDF *of a* $\mathcal{N}(0,1)$ *distribution (blue) and a Cauchy*$(0,1)$ *distribution (red). Right: log likelihood cost function of the* PDF $\mathcal{N}(0,1)$ *(blue) and of the* PDF *Cauchy*$(0,1)$ *(red).*

and its log likelihood cost function are depicted in red in Figure 3.2. The PDF has heavy tails (left plot) and its log likelihood cost function (right plot) hence does not severely punish the presence of outliers. To only allow for time *delays* of the UWB pulses, in Paper B we assume that the noise is asymmetrically distributed, with a Cauchy distribution on one side and a Gaussian distribution on the other. In Example 3.3 we will illustrate the difference in handling outliers between a Gaussian and a Cauchy distribution.

Example 3.3: Parameter estimation with/without measurement outliers

Consider the problem of estimating the parameter θ in the following regression problem

$$y_t = \theta t + e_t. \tag{3.16}$$

Assuming $e_t \sim \mathcal{N}(0,1)$ and $\theta = 0.2$ we simulate the measurements depicted in Figure 3.3. In the left plot, 50 measurements y_t are simulated at $t = -25, \ldots, 25$. In the right plot, we assume the presence of two outliers, $y_t = 20$ at $t = -15$ and $y_t = -20$ at $t = 15$. An estimate of the parameter θ is obtained both assuming a Gaussian ($\hat{\theta}^{\text{G}}$) and a Cauchy distribution ($\hat{\theta}^{\text{C}}$) for the noise e_t (see Examples 3.1 and 3.2, respectively). The lines drawn with the estimated parameters $\hat{\theta}^{\text{G}}$ and $\hat{\theta}^{\text{C}}$ show that the presence of the outliers has a greater impact on the estimate $\hat{\theta}^{\text{G}}$ than on the estimate $\hat{\theta}^{\text{C}}$. This is due to the heavy tails of the Cauchy distribution, as shown in Figure 3.2.

3.3 Model parameters in a state-space model

In (3.3) we described the magnetometer measurement function used in Paper A to account for the case that the magnetometer is uncalibrated. Comparing (3.3b)

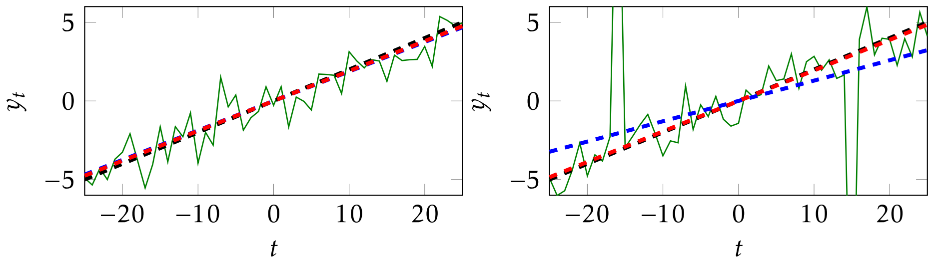

Figure 3.3: *Measurements y_t (green) with (dashed black) the line θt (see (3.16)), (dashed blue) the line $\hat{\theta}_G t$ and (dashed red) $\hat{\theta}_C t$. Left: 50 measurements at $t = -25, \dots, 25$. Right: 50 measurements at $t = -25, \dots, 25$, but at $t = -15$ and $t = 15$, we assume two measurement outliers $y_t = 20$ and $y_t = -20$, respectively.*

to (3.13), we note that there is a fundamental difference. The model (3.13) consists of only known quantities and model parameters. However, the model (3.3b) consists of both known quantities, model parameters and states R_t^{nb} from a state-space model (1.1).

To fully define the magnetometer calibration problem, we therefore need to include the state-space model and determine D and o from

$$R_{t+1}^{\text{nb}} = f_t(R_t^{\text{nb}}, y_{\omega,t}, e_{\omega,t}), \tag{3.17a}$$

$$y_{\text{a},t} = -R_t^{\text{bn}} g^{\text{n}} + e_{\text{a},t}, \tag{3.17b}$$

$$y_{\text{m},t} = D R_t^{\text{bn}} m^{\text{n}} + o + e_{\text{m},t}, \tag{3.17c}$$

where we denote the state vector representing the orientation as R_t^{nb}. Note that we implicitly assume that the state is parametrized by either a quaternion as in Algorithm 1 or by an orientation deviation from a linearization point as in Algorithm 2.

Equivalently to (3.4), we want to estimate the predicted measurements $\hat{y}_t(\theta)$ from the model. The predicted measurements in (3.17), however, depend on the states. Hence, using conditional probabilities and the fact that the logarithm is a monotonic function, we have the following equivalent formulation of (3.2),

$$\hat{\theta}^{\text{ML}} = \operatorname*{arg\,min}_{\theta \in \Theta} - \sum_{t=1}^{N} \log p_\theta(y_t \mid y_{1:t-1}), \tag{3.18}$$

where we use the convention that $y_{1:0} \triangleq \emptyset$. In case the state-space model is nonlinear, there is typically no closed form solution available for the one step ahead predictor $p_\theta(y_t \mid y_{1:t-1})$ in (3.18). In Paper A, we assume that the noise is Gaussian and approximate the one step ahead predictor using an EKF, see also Section 2.2. The result is

$$p_\theta(y_t \mid y_{1:t-1}) \approx \mathcal{N}\left(y_t \mid \hat{y}_{t|t-1}(\theta), S_t(\theta)\right), \tag{3.19}$$

where, $\hat{y}_{t|t-1}$ and S_t are estimated using an EKF. Inserting (3.19) into (3.18) and neglecting all constants results in the following optimization problem,

$$\min_{\theta \in \Theta} \frac{1}{2} \sum_{t=1}^{N} \left(\|y_t - \hat{y}_{t|t-1}(\theta)\|^2_{S_t^{-1}(\theta)} + \log\det S_t(\theta) \right). \tag{3.20}$$

As discussed in Section 3.1, we solve our optimization problems using the gradient and the (approximate) Hessian of the cost function. For the cases discussed in Section 3.2, these expressions can be obtained relatively easy as shown in Examples 3.1 and 3.2. For the cost function (3.20), however, it is less straightforward to obtain an expression for the gradient and the Hessian. Using the time and measurement update equations (2.9) and (2.11) for a scalar parameter θ, the Jacobian can be derived to be

$$\frac{\partial \hat{y}_{t+1|t}}{\partial \theta} = C_t \frac{\partial \hat{x}_{t+1|t}}{\partial \theta} + \frac{\partial C_t}{\partial \theta} \hat{x}_{t+1|t} \tag{3.21a}$$

$$\frac{\partial \hat{x}_{t+1|t}}{\partial \theta} = \frac{\partial A_t}{\partial \theta} \hat{x}_{t|t} + A_t \frac{\partial \hat{x}_{t|t}}{\partial \theta} \tag{3.21b}$$

$$\frac{\partial \hat{x}_{t|t}}{\partial \theta} = \frac{\partial \hat{x}_{t|t-1}}{\partial \theta} + \frac{\partial}{\partial \theta} \left(P_{t|t-1} C_t^{\mathsf{T}} \left(C_t P_{t|t-1} C_t^{\mathsf{T}} + R \right)^{-1} \left(y_t - \hat{y}_{t|t-1} \right) \right) \tag{3.21c}$$

$$\frac{\partial P_{t|t-1}}{\partial \theta} = \frac{\partial}{\partial \theta} \left(A_{t-1} P_{t-1|t-1} A_{t-1}^{\mathsf{T}} + G_{t-1} Q G_{t-1}^{\mathsf{T}} \right) \tag{3.21d}$$

$$\vdots \tag{3.21e}$$

As can be seen from (3.21), the expression for the gradient of the objective function in (3.20) is defined recursively using the EKF time and measurement equations. Its computation is hence more involved than in the case discussed in Section 3.2. In Åström (1980); Segal and Weinstein (1989), different approaches are discussed to determine analytical gradients of the objective function in (3.20). They, however, consider the case of a linear state-space model. In our problems, we use an EKF implementation where the matrices A_t, C_t and G_t are based on linear approximations of the dynamic and measurement model. Hence, these methods only lead to approximate gradients of the objective function. Because of this, in Paper A we solve (3.20) using numerical gradients and a Hessian estimated using a BFGS algorithm. This approach is computationally quite expensive, but the computations of the gradients can easily be parallelized.

4

Concluding remarks

In Part I of this thesis, we have given an introduction to the four papers that will be presented in Part II. In Chapter 1, the different sensors that are used throughout the thesis were introduced together with the subject of probabilistic modeling. Chapter 2 subsequently focused on pose estimation using inertial sensors and magnetometers, introducing relevant background material for Papers A – D in Part II. The subject of sensor calibration was discussed in Chapter 3. It provides background to the magnetometer calibration problem discussed in Paper A and the calibration of the UWB setup in Paper B. In this chapter, we will summarize the contributions of this thesis in Section 4.1 and discuss possible directions for future work in Section 4.2.

4.1 Summary of the contributions

The main contributions of the thesis are within the domain of position and orientation (pose) estimation using inertial sensors in combination with additional (sensor) information. Since using uncalibrated sensors for pose estimation would lead to inaccurate estimates, we focus both on pose estimation algorithms and on sensor calibration. The problems are formulated based on probabilistic models of the sensor information and the model assumptions. The pose estimation algorithms are solved using MAP estimation while the calibration problems are solved using ML algorithms.

4.1.1 Sensor calibration

Sensor calibration problems are addressed in Papers A and B. In Paper A, we consider the problem of combining the inertial sensors with a magnetometer for orientation estimation. The magnetometer is not assumed to be calibrated. We present a practical calibration algorithm that calibrates the magnetometer for the presence of magnetic disturbances rigidly attached to the sensor, for magnetometer sensor errors and for misalignment between the inertial and the magnetometer sensor axes. Using the calibrated magnetometer measurements to estimate the sensor's orientation is experimentally shown to lead to significantly improved heading estimates.

Paper B focuses both on calibration and on state estimation. It addresses the problem of combining TOA measurements from a UWB system with inertial measurements for 6D pose estimation. We use a setup where a number of UWB receivers are placed in an indoor environment and move a UWB transmitter through the measurement volume. To be able to obtain position information from the UWB measurements, it is imperative that accurate estimates of the receivers' positions and clock offsets are known. To avoid the typically labor-intensive and time-consuming process of surveying the receivers' positions, we present an easy-to-use calibration method. We model the UWB measurements assuming an asymmetric heavy-tailed noise distribution, which naturally handles measurement outliers due to multipath and/or NLOS conditions.

4.1.2 Pose estimation

After the UWB calibration discussed in Section 4.1.1, the UWB system considered in Paper B can be used for pose estimation of a subject wearing inertial sensors and UWB transmitters walking through the environment. We present a tightly-coupled sensor fusion approach to combine the inertial measurements with the TOA measurements. It is shown to lead to accurate pose estimates as compared to data from an optical reference system.

Paper C discusses the problem of inertial human body motion capture, where a multitude of body segments are equipped with IMUs as shown in Figure 1.5. Relative position and orientation estimates are obtained using the inertial measurements together with a biomechanical model, which models the body in terms of connected body segments. The problem is formulated as a MAP problem and is solved using optimization-based techniques. As a proof-of-concept we apply our algorithm to a lower body configuration, illustrating that the estimates are drift-free and match the joint angles from an optical reference system.

Paper D presents an approach for 6D pose estimation where inertial measurements are complemented with magnetometer measurements assuming that a model (map) of the magnetic field is available. In our experimental study, the magnetic field is generated by a magnetic coil, giving rise to a magnetic field that we can model analytically. The experimental results show that accurate position estimates can be obtained in the vicinity of the coil, where the magnetic field is strong.

4.2 Future work

In this section we will discuss ideas for future work for each of the papers. In Section 4.2.1 we will first discuss ideas for future work in the field of sensor calibration, related to Paper A. Subsequently, in Section 4.2.2 we will first discuss ideas for future work in the field of pose estimation, related to Papers B – D.

4.2.1 Sensor calibration

In Paper A we show that our calibration algorithm leads to significantly improved heading estimates based on measurements from two different commercially available IMUs. An interesting line of future work is to apply the magnetometer calibration algorithm to inertial and magnetometer measurements from a smartphone. Smartphones typically use their own magnetometer calibration algorithm, thereby complicating the testing of other calibration algorithms. However, as of Android API level 18 (Jelly Bean MR2), it is possible to log uncalibrated magnetometer data. Hence, it is be possible to apply our calibration algorithm to measurements from a smartphone.

Another possible direction for future work extends the calibration algorithm to also be able to include GPS measurements in outdoor applications. In that case, the extended Kalman filter (EKF) providing the measurement predictions to the ML problem as discussed in Section 3.3 would have to be extended to include at least a position and a velocity state. The additional GPS information should significantly help in calibrating the magnetometer. However, the algorithm would be computationally more expensive due to the additional states in the EKF.

The calibration algorithm is now formulated as a batch, offline, method. It would be interesting to extend it to an online approach. Using this approach, it might be possible to automatically recalibrate the sensor once it enters a different magnetic environment.

4.2.2 Pose estimation

Paper B uses a heavy-tailed asymmetric noise distribution to represent the presence of outliers in the UWB measurements. This distribution is used both in the UWB calibration algorithm and in our approach to determine the transmitter's position using UWB multilateration. In future work we are planning to extend the sensor fusion algorithm which combines the UWB measurements with inertial measurements to also make use of the heavy-tailed asymmetric noise distribution. We plan to implement the sensor fusion algorithm as an optimization problem similar to our approach in Paper C. Using an optimization formulation, different noise assumptions can straightforwardly be used.

In Paper C, we apply our motion capture algorithm to a lower body configuration consisting of 7 IMUs places on the feet, lower legs, upper legs and pelvis. An obvious direction of future work would of course be to include more body segments.

The algorithm relies on knowledge about the position and orientation of the sensors on the body. This information can be regarded as calibration parameters. We plan to extend the approach to also estimate these calibration parameters.

In Paper C, we focus only on estimating body's *relative* pose. To estimate its *absolute* position, it is possible to include foot step detection, see e.g. Callmer (2013). It would also be possible to combine the approaches in Papers B and C and use UWB measurements to estimate the position of the body.

Paper D discusses the problem of pose estimation assuming a known magnetic field map. In experiments, we have used a magnetic coil to generate a known magnetic field. We have also been working on an approach to estimate the magnetic field map (Wahlström et al., 2013). An interesting line of research would be to combine both approaches. The ultimate goal would then be to do *simultaneous localization and mapping* (SLAM) where we simultaneously build a magnetic map of the environment and localize the sensor in the environment.

Bibliography

M. Angermann, M. Frassl, M. Doniec, B. J. Julian, and P. Robertson. Characterization of the indoor magnetic field for applications in localization and mapping. In *Proceedings of the IEEE International Conference on Indoor Positioning and Indoor Navigation (IPIN)*, pages 1–9, Sydney, Australia, Nov 2012.

K. J. Åström. Maximum likelihood and prediction error methods. *Automatica*, 16(5):551–574, 1980.

C. M. Bishop. *Pattern recognition and machine learning*. Springer, 2006.

T. Bohlin. *Practical Grey-box Process Identification; Theory and Appications*. Springer, 2006.

S. Boyd and L. Vandenberghe. *Convex Optimization*. Cambridge University Press, 2004.

J. Callmer. *Autonomous Localization in Unknown Environments*. PhD thesis, Linköping University, Sweden, June 2013.

J. L. Crassidis, F. L. Markley, and Y. Cheng. A survey of nonlinear attitude estimation methods. *Journal of Guidance, Control, and Dynamics*, 30(1):12–28, 2007.

A. Doucet and A. M. Johansen. A tutorial on particle filtering and smoothing: Fifteen years later. In *The Oxford Handbook of Nonlinear Filtering*. Oxford University Press, 2011.

H. Driessen and Y. Boers. MAP estimation in particle filter tracking. In *IET Seminar on Target Tracking and Data Fusion: Algorithms and Applications*, pages 41–45, 2008.

M. Frassl, M. Angermann, M. Lichtenstern, P. Robertson, B. J. Julian, and M. Doniec. Magnetic maps of indoor environments for precise localization of legged and non-legged locomotion. In *Proceedings of the IEEE/RSJ International Conference on Intelligent Robots and Systems (IROS)*, pages 913–920, Tokyo, Japan, Nov 2013.

N. J. Gordon, D. J. Salmond, and A. F. M. Smith. Novel approach to nonlinear/non-Gaussian Bayesian state estimation. In *IEE Proceedings on Radar and Signal Processing*, volume 140, pages 107–113, 1993.

S. Grzonka. *Mapping, State Estimation, and Navigation for Quadrotors and Human-Worn Sensor Systems*. PhD thesis, Freiburg University, Germany, September 2011.

F. Gustafsson. *Statistical Sensor Fusion*. Studentlitteratur, 2012.

W. R. Hamilton. On quaternions; or on a new system of imaginaries in algebra. *Philosophical Magazine*, xxv, 1844.

J. D. Hol. *Sensor Fusion and Calibration of Inertial Sensors, Vision, Ultra-Wideband and GPS*. PhD thesis, Linköping University, Sweden, June 2011.

J. D. Hol, F. Dijkstra, H. Luinge, and T. B. Schön. Tightly coupled UWB/IMU pose estimation. In *Proceedings of the IEEE International Conference on Ultra-Wideband (ICUWB)*, pages 688–692, Vancouver, Canada, September 2009.

J. D. Hol, T. B. Schön, and F. Gustafsson. Ultra-wideband calibration for indoor positioning. In *Proceedings of the IEEE International Conference on Ultra-Wideband (ICUWB)*, pages 1–4, Nanjing, China, September 2010.

R. E. Kalman. A new approach to linear filtering and prediction problems. *Journal of basic Engineering*, 82(1):35–45, 1960.

M. Kok and T. B. Schön. Maximum likelihood calibration of a magnetometer using inertial sensors. In *Proceedings of the 19th World Congress of the International Federation of Automatic Control (accepted for publication)*, Cape Town, South Africa, August 2014a.

M. Kok and T. B. Schön. Magnetometer calibration using inertial sensors. *Preprint*, 2014b.

M. Kok, J. D. Hol, T. B. Schön, F. Gustafsson, and H. Luinge. Calibration of a magnetometer in combination with inertial sensors. In *Proceedings of the 15th International Conference on Information Fusion*, Singapore, July 2012.

M. Kok, N. Wahlström, T. B. Schön, and F. Gustafsson. MEMS-based inertial navigation based on a magnetic field map. In *Proceedings of the 38th International Conference on Acoustics, Speech, and Signal Processing (ICASSP)*, pages 6466–6470, Vancouver, Canada, May 2013.

M. Kok, J. D. Hol, and T. B. Schön. An optimization-based approach to human body motion capture using inertial sensors. In *Proceedings of the 19th World Congress of the International Federation of Automatic Control (accepted for publication)*, Cape Town, South Africa, August 2014a.

M. Kok, J. D. Hol, and T. B. Schön. Indoor positioning using ultra-wideband and inertial measurements. *Preprint*, 2014b.

J. Kronander, J. Dahlin, D. Jönsson, M. Kok, T. B. Schön, and J. Unger. Real-time video based lighting using GPU raytracing. In *Proceedings of the 2014 European Signal Processing Conference (EUSIPCO)*, Lisbon, Portugal, September 2014. (submitted, pending review).

J. B. Kuipers. *Quaternions and Rotation Sequences: a primer with applications to orbits, aerospace, and virtual reality*. Princeton University Press, 1999.

F. Lindsten. *Particle filters and Markov chains for learning of dynamical systems*. PhD thesis, Linköping University, Sweden, 2013.

F. Lindsten and T. B. Schön. Backward simulation methods for Monte Carlo statistical inference. *Foundations and Trends in Machine Learning*, 6(1):1–143, 2013.

L. Ljung. *System Identification, Theory for the User*. Prentice Hall PTR, 2nd edition, 1999.

H. J. Luinge. *Inertial Sensing of Human Movement*. PhD thesis, University of Twente, Enschede, the Netherlands, October 2002.

F. L. Markley. Attitude error representations for Kalman filtering. *Journal of guidance, control, and dynamics*, 26(2):311–317, 2003.

J. Nocedal and S. J. Wright. *Numerical Optimization*. Springer Series in Operations Research, 2nd edition, 2006.

J. B. Rawlings and D. Q. Mayne. *Model Predictive Control: Theory and Design*. Nob Hill Publishing, 2009.

S. Saha, Y. Boers, H. Driessen, P. K. Mandal, and A. Bagchi. Particle based MAP state estimation: A comparison. In *Proceedings of the 12th International Conference on Information Fusion*, pages 278–283, July 2009.

S. Saha, P. Mandal, A. Bagchi, Y. Boers, and H. Driessen. Particle based smoothed marginal MAP estimation for general state space models. *IEEE Transactions on Signal Processing*, 61(2):264–273, 2013.

T. B. Schön, F. Gustafsson, and P. J. Nordlund. Marginalized particle filters for mixed linear/nonlinear state-space models. *IEEE Transactions on Signal Processing*, 53(7):2279–2289, 2005.

M. Segal and E. Weinstein. A new method for evaluating the log-likelihood gradient, the Hessian, and the Fisher information matrix for linear dynamic systems. *IEEE Transactions on Information Theory*, 35(3):682–687, 1989.

M. D. Shuster. A survey of attitude representations. *The Journal of the Astronautical Sciences*, 41(4):439–517, oct–dec 1993.

D. H. Titterton and J. L. Weston. *Strapdown inertial navigation technology*. IEE radar, sonar, navigaton and avionics series 5. Peter Peregrinus LTd. on behalf of the Institution of Electrical Engineers, 1997.

D. Törnqvist. *Estimation and Detection with Applications to Navigation*. PhD thesis, Linköping University, November 2008. Thesis No. 1216.

N. Wahlström, M. Kok, T. B. Schön, and F. Gustafsson. Modeling magnetic fields using Gaussian processes. In *Proceedings of the 38th International Conference on Acoustics, Speech, and Signal Processing (ICASSP)*, pages 3522–3526, Vancouver, Canada, May 2013.

O. J. Woodman. *Pedestrian localisation for indoor environments*. PhD thesis, University of Cambridge, United Kingdom, September 2010.

Xsens Technologies B.V. `http://www.xsens.com`, Accessed on April 24, 2014.

Part II

Publications

Paper A

Magnetometer calibration using inertial sensors

Authors: Manon Kok and Thomas B. Schön

Edited version of the paper:

M. Kok and T. B. Schön. Magnetometer calibration using inertial sensors. *Preprint*, 2014b.

Earlier versions of this work were presented in

M. Kok and T. B. Schön. Maximum likelihood calibration of a magnetometer using inertial sensors. In *Proceedings of the 19th World Congress of the International Federation of Automatic Control (accepted for publication)*, Cape Town, South Africa, August 2014a,

M. Kok, J. D. Hol, T. B. Schön, F. Gustafsson, and H. Luinge. Calibration of a magnetometer in combination with inertial sensors. In *Proceedings of the 15th International Conference on Information Fusion*, Singapore, July 2012.

Magnetometer calibration using inertial sensors

Manon Kok⋆ and Thomas B. Schön†

⋆Dept. of Electrical Engineering,
Linköping University,
SE–581 83 Linköping, Sweden
manko@isy.liu.se

†Dept. of Information Technology
Uppsala University,
SE-751 05 Uppsala, Sweden
thomas.schon@uu.se

Abstract

In this work we present a practical calibration algorithm that calibrates a magnetometer using inertial sensors. The calibration corrects for magnetometer sensor errors, for the presence of magnetic disturbances and for misalignment between the magnetometer and the inertial sensor axes. It is based on a maximum likelihood formulation and is formulated as an offline method. It is shown to give good results using data from two different commercially available sensor units. Using the calibrated magnetometer measurements in combination with the inertial sensors to determine orientation, is shown to lead to significantly improved heading estimates.

1 Introduction

Nowadays, magnetometers and inertial sensors (accelerometers and gyroscopes) are widely available in for instance dedicated sensor units and smartphones. In the case of low or zero acceleration, the accelerometer measurements are dominated by the gravity component. Hence, they can be used to estimate the inclination of the sensor. When no magnetic disturbances are present, the magnetometer measures a constant local magnetic field vector. This vector points to the magnetic north and can hence be used for heading estimation. Inertial sensors and magnetometers have successfully been used to obtain accurate 3D orientation estimates, see e.g. Gustafsson (2012); Hol (2011). For this, however, it is imperative that the sensors are properly calibrated and that the sensor axes are aligned. This calibration is specifically of concern for the magnetometer, which needs recalibration whenever it is placed in a (magnetically) different environment. When the magnetic disturbance is a result of the mounting of the magnetometer onto a magnetic object, the magnetometer can be calibrated to compensate for the presence of this disturbance.

In this work, we present a magnetometer calibration algorithm that calibrates a magnetometer using inertial sensors. It is formulated as a maximum likeli-

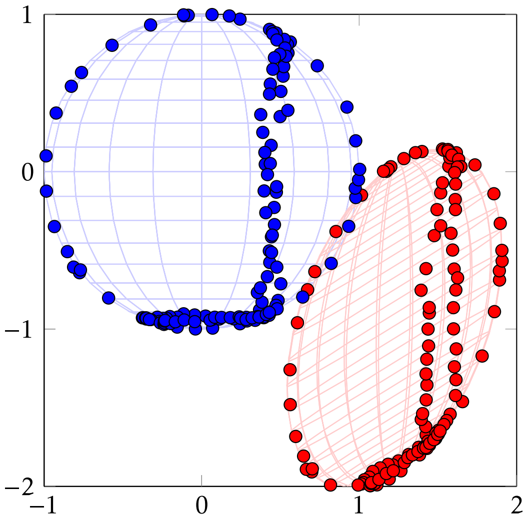

Figure 1: *Example calibration results with an ellipsoid of magnetometer data before calibration (red) and a unit sphere of data after calibration (blue).*

hood problem. The algorithm calibrates the magnetometer for the presence of magnetic disturbances, for magnetometer sensor errors and for misalignment between the magnetometer and the inertial sensor axes. Using the calibrated magnetometer measurements to estimate the sensor's orientation is experimentally shown to lead to significantly improved heading estimates.

To perform the calibration, the sensor needs to be rotated in all possible orientations. A perfectly calibrated magnetometer would measure rotated versions of the local magnetic field vector. Hence, the magnetometer data would lie on a sphere. In practice, however, the magnetometer will often measure an ellipsoid of data instead. The calibration maps the ellipsoid of the data to a sphere of data as illustrated in Figure 1. The alignment of the inertial and magnetometer sensor axes is included by determining the orientation of the sphere. Since we are interested in improving the heading estimates, the actual magnitude of the local magnetic field is of no concern. Hence we assume without loss of generality that the norm is equal to 1, i.e. the sphere in Figure 1 is a unit sphere.

Mounting of the sensor often severely limits its rotational freedom, for instance in cases of mounting it onto a boat or a car (Wu et al., 2013a,b). Magnetometer calibration algorithms, however, generally rely on the assumption that the magnetometer's rotation is "sufficiently" excited, i.e. that measurements on a sufficiently large part of the ellipsoid in Figure 1 are available. A secondary contribution of this paper is a quantification of how much rotation is needed to solve the calibration problem. This is quantified based on an identifiability analysis, deriving how much rotation is needed in case of perfect measurements.

Magnetometer calibration approaches typically regard the problem as an ellipse fitting problem, see e.g. Alonso and Shuster (2002); Gebre-Egziabher et al. (2006); Renaudin et al. (2010). Ellipse fitting problems can map the data to a sphere, but can not determine the rotation of the sphere. This rotation is, however, of interest when calibrating the magnetometer for improved heading estimation in combination with inertial sensors. To solve this problem, recent approaches include a second step in the calibration algorithm to determine this misalignment (Vasconcelos et al., 2011; Li and Li, 2012; Salehi et al., 2012; Bonnet et al., 2009). Typically, accelerometer measurements from periods of fairly low accelerations have been used for this, disregarding the gyroscope measurements. Troni and Whitcomb (2013) use the gyroscope measurements to determine the misalignment. Our algorithm uses a conceptually similar approach to determine an initial estimate for the non-convex maximum likelihood problem. We will analyze the quality of the initial estimate and the maximum likelihood estimate in terms of their heading accuracy, both for experimental and simulated data. Based on this analysis, we will show that significant heading accuracy improvements can be obtained using our maximum likelihood algorithm.

2 Problem formulation

Our magnetometer calibration algorithm is formulated as a problem of determining the sensor's orientation in the presence of unknown model parameters θ. It can hence be considered to be a grey-box system identification problem. It makes use of a nonlinear state space model

$$x_{t+1} = f_t(x_t, u_t, \theta) + G_t(x_t)v_t(\theta), \tag{1a}$$

$$y_t = h_t(x_t, \theta) + e_t(\theta), \tag{1b}$$

where the state $x_t \in \mathbb{R}^{n_x}$ represents the sensor's orientation. The dynamic model is denoted by $f_t(\,\cdot\,)$ and depends on measured inputs u_t. The measurements $y_t \in \mathbb{R}^{n_y}$ are modeled by a function $h_t(\,\cdot\,)$. Finally, v_t and e_t represent mutually independent process and measurement noise, respectively, and $G_t(\,\cdot\,)$ describes how the noise v_t affects the state x_t. The dependence on the parameter vector θ is explicitly indicated in (1). The exact details of the model are introduced in Section 3.

The calibration problem is formulated as a maximum likelihood (ML) problem. Hence, the parameters θ are found by maximizing the likelihood function,

$$\widehat{\theta}^{\text{ML}} = \arg\max_{\theta \in \Theta} \; p_\theta(y_{1:N}), \tag{2}$$

where $y_{1:N} = \{y_1, \ldots, y_N\}$ and $\Theta \subseteq \mathbb{R}^{n_\theta}$. Using conditional probabilities and the fact that the logarithm is a monotonic function we have the following equivalent formulation of (2),

$$\widehat{\theta}^{\text{ML}} = \operatorname*{arg\,min}_{\theta \in \Theta} - \sum_{t=1}^{N} \log p_\theta(y_t \mid y_{1:t-1}), \tag{3}$$

where we use the convention that $y_{1:0} \triangleq \emptyset$. The ML estimator (3) enjoys well-understood theoretical properties including strong consistency, asymptotic normality, and asymptotic efficiency (Ljung, 1999).

The state space model (1) is nonlinear, implying that there is no closed form solution available for the one step ahead predictor $p_\theta(y_t \mid y_{1:t-1})$ in (3). This can systematically be handled using sequential Monte Carlo methods (e.g. particle filters and particle smoothers), see e.g. Schön et al. (2011); Lindsten and Schön (2013). However, for the magnetometer calibration problem it is sufficient to make use of a more pragmatic approach; we simply approximate the one step ahead predictor using an extended Kalman filter (EKF). The result is

$$p_\theta(y_t \mid y_{1:t-1}) \approx \mathcal{N}\left(y_t \mid \widehat{y}_{t|t-1}(\theta), S_t(\theta)\right), \tag{4}$$

where $\mathcal{N}\left(y_t \mid \widehat{y}_{t|t-1}(\theta), S_t(\theta)\right)$ denotes the probability density function for the Gaussian random variable y_t with mean value $\widehat{y}_{t|t-1}(\theta)$ and covariance $S_t(\theta)$. Here, $S_t(\theta)$ is the residual covariance from the EKF (Gustafsson, 2012). Inserting (4) into (3) and neglecting all constants results in the following optimization problem,

$$\min_{\theta \in \Theta} \frac{1}{2} \sum_{t=1}^{N} \|y_t - \widehat{y}_{t|t-1}(\theta)\|^2_{S_t^{-1}(\theta)} + \log \det S_t(\theta), \tag{5}$$

which we can solve for the unknown parameters θ. The problem (5) is non-convex, implying that a good initial value for θ is required.

3 Models

The state space model (1) describes the sensor's orientation in terms of the gyroscope measurements $y_{\omega,t}$, the accelerometer measurements $y_{\text{a},t}$ and the magnetometer measurements $y_{\text{m},t}$. The orientation is represented from the body frame b to the navigation frame n, expressed using a unit quaternion q_t^{nb}. The body frame b is the coordinate frame of the inertial sensor, having its origin in the center of the accelerometer triad and its axes aligned with the inertial sensor axes. The navigation frame n is aligned with the earth's gravity and the local magnetic field.

As discussed in Section 2, we estimate the orientation using an extended Kalman filter (EKF). Orientations are commonly represented using unit quaternions, see e.g. Hamilton (1844); Kuipers (1999). A possible implementation of the EKF hence uses a quaternion as a 4-dimensional state vector (Gustafsson, 2012; Kok and Schön, 2014a). The downside of this implementation is that care must be taken that the norm of the quaternion is conserved. Also, the state covariance matrix is represented by a 4×4 matrix. Due to the norm 1 constraint on the quaternions, this matrix is rank deficient. However, the state covariance matrix estimated by the EKF is full rank due to linearization errors. To avoid problems due to the norm constraint of the quaternion, we use an implementation of the EKF, which is sometimes called a multiplicative EKF (Markley, 2003; Crassidis et al., 2007; Hol, 2011). Here, a 3-dimensional state vector represents the orientation deviation from a linearization point. The linearization point is represented using a unit quaternion.

3.1 Dynamic model

The dynamic model (1a) describes the orientation q^{nb} in terms of the angular velocity ω as

$$q^{\mathrm{nb}}_{t+1} = q^{\mathrm{nb}}_t \odot \exp \tfrac{T}{2}\omega_t. \tag{6}$$

Here, $\odot$ denotes a quaternion multiplication and the exponential of a vector a is defined as the following 4-dimensional vector (Hol, 2011)

$$\exp a = \begin{pmatrix} \cos \|a\|_2 & \frac{a^{\mathsf{T}}}{\|a\|_2} \sin \|a\|_2 \end{pmatrix}^T . \tag{7}$$

An estimate of the angular velocity ω_t can obtained from the measurement $y_{\omega,t}$, which is modeled as

$$y_{\omega,t} = \omega_t + \delta_\omega + v_{\omega,t}. \tag{8}$$

Here, δ_ω denotes the gyroscope bias and $v_{\omega,t} \sim \mathcal{N}(0, \Sigma_\omega)$. The gyroscope measurements are hence used as an input to the dynamic model.

3.2 Accelerometer measurement model

The measurement model (1b) entails the accelerometer measurements and the magnetometer measurements. The accelerometer measurements $y_{\mathrm{a},t}$ are modeled as

$$y_{\mathrm{a},t} = R^{\mathrm{bn}}_t (a^{\mathrm{n}}_t - g^{\mathrm{n}}) + e_{\mathrm{a},t} \approx -R^{\mathrm{bn}}_t g^{\mathrm{n}} + e_{\mathrm{a},t}, \tag{9}$$

where a^{n}_t denotes the sensor's acceleration in the navigation frame, g^{n} denotes the earth's gravity and the accelerometer noise is assume to be $e_{\mathrm{a},t} \sim \mathcal{N}(0, \Sigma_{\mathrm{a}})$. The matrix R^{bn}_t is the rotation matrix representation of the quaternion $q^{\mathrm{bn}}_t = (q^{\mathrm{nb}}_t)^c$, where c denotes the quaternion conjugate (Hol, 2011). As indicated in (9), we assume the sensor's acceleration to be approximately zero.

3.3 Magnetometer measurement model

In the case of a perfectly calibrated magnetometer, the magnetometer measures the local magnetic field and its measurements $y_{\mathrm{m},t}$ will therefore lie on a sphere with a radius equal to the local magnetic field m^{n}, i.e.

$$y_{\mathrm{m},t} = m^{\mathrm{b}}_t = R^{\mathrm{bn}}_t m^{\mathrm{n}}. \tag{10}$$

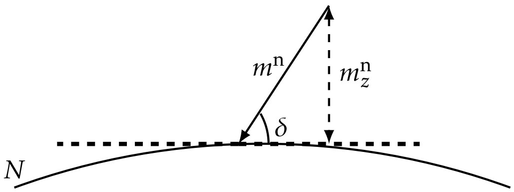

Figure 2: *Schematic of a part of the earth where the earth magnetic field* m^{n} *makes an angle* δ *with the horizontal plane. The vertical component of* m^{n} *is denoted by* m_z^{n}*. The location of the magnetic north is indicated with an* N*.*

In outdoor environments, the local magnetic field is equal to the local earth magnetic field. Its horizontal component points towards the earth's magnetic north pole. The ratio between the horizontal and vertical component depends on the location on the earth and can be expressed in terms of the dip angle δ. Figure 2 schematically depicts part of the earth and illustrates the definition of the dip angle and the vertical component m_z^{n}. In indoor environments, the magnetic field can locally be assumed to be constant and points towards a local magnetic north. Note that this is not necessarily the earth's magnetic north pole. Choosing the navigation frame n such that the x-axis is pointing towards the local magnetic north, the local magnetic field m^{n} is given by

$$m^{\mathrm{n}} = \begin{pmatrix} \sqrt{1-(m_z^{\mathrm{n}})^2} & 0 & m_z^{\mathrm{n}} \end{pmatrix}^T, \tag{11a}$$

$$= \begin{pmatrix} \cos\delta & 0 & -\sin\delta \end{pmatrix}^T. \tag{11b}$$

Note that, as described in Section 1, we assume without loss of generality that the norm of the local magnetic field is equal to one.

In the remainder of this section we will introduce our magnetometer measurement model. This will result in a model where the magnetometer measurements can be described in terms of a 3 × 3 calibration matrix D and a 3 × 1 offset vector o according to

$$y_{\mathrm{m},t} = DR_t^{\mathrm{bn}} m^{\mathrm{n}} + o + e_{\mathrm{m},t}, \tag{12}$$

with $e_{\mathrm{m},t} \sim \mathcal{N}(0, \Sigma_{\mathrm{m}})$. We will first introduce the different parts of the model. Subsequently, the model assumptions will be addressed.

Magnetometer sensor errors

One reason for why magnetometer calibration is necessary is the presence of sensor errors in the magnetometer. These errors are sensor-specific and can differ for each magnetometer. They can be subdivided into four components, see e.g. Gebre-Egziabher et al. (2006); Renaudin et al. (2010); Vasconcelos et al. (2011).

1. Non-orthogonality of the magnetometer axes, represented by a matrix C_{no}.
2. Presence of a zero bias or null shift, implying that the magnetometer will measure a non-zero magnetic field even if the magnetic field is zero, defined

by o_{zb}.

3. Difference in sensitivity of the three magnetometer axes, represented by a diagonal matrix C_{sc}.
4. Presence of noise in the magnetometer measurements. We will assume this noise to be independently and identically distributed (i.i.d.) Gaussian noise and it will be denoted by $e_{\text{m},t}$.

We can therefore rewrite (10) to include the magnetometer sensor errors as

$$y_{\text{m},t} = C_{\text{sc}} C_{\text{no}} m_t^{\text{b}} + o_{\text{zb}} + e_{\text{m},t}. \tag{13}$$

Presence of magnetic disturbances

Inertial sensors and magnetometers are often used to estimate an object's orientation. The IMU is then rigidly attached to the object so that its orientation reflects the object's orientation. These objects, however, frequently contain ferromagnetic material. Examples of this are applications where we are interested in the orientation of a car or a smartphone.

In the vicinity of magnetic materials, a magnetometer will not only measure the local magnetic field, but also additional magnetic field components. These additional magnetic field components consist of hard and soft iron effects. Hard iron effects are due to permanent magnetization of the magnetic material and lead to a constant offset o_{hi} of the ellipsoid of data. Soft iron effects are due to magnetization of the material as a result of an external magnetic field and will therefore depend on the orientation of the material with respect to the local magnetic field. We model this in terms of a 3×3 matrix C_{si}.

Extending (13) to also include the model of the magnetic disturbances introduced above, results in

$$y_{\text{m},t} = C_{\text{sc}} C_{\text{no}} \left(C_{\text{si}} m_t^{\text{b}} + o_{\text{hi}} \right) + o_{\text{zb}} + e_{\text{m},t}. \tag{14}$$

Magnetometer and inertial sensor axes alignment

When calibrating the magnetometer to obtain better orientation estimates, it is important that the magnetometer and inertial sensor axes are aligned. Introducing a rotation matrix R_{im} describing the misalignment between the inertial sensors and the magnetometer in (14) results in

$$y_{\text{m},t} = C_{\text{sc}} C_{\text{no}} \left(C_{\text{si}} R_{\text{im}} m_t^{\text{b}} + o_{\text{hi}} \right) + o_{\text{zb}} + e_{\text{m},t}. \tag{15}$$

Resulting magnetometer measurement model

To obtain a correct calibration, it is not necessary to identify all individual contributions of the different components in (15). Instead, they can be combined into a 3×3 distortion matrix D and a 3×1 offset vector o where

$$D = C_{\mathrm{sc}} C_{\mathrm{no}} C_{\mathrm{si}} R_{\mathrm{im}}, \tag{16a}$$

$$o = C_{\mathrm{sc}} C_{\mathrm{no}} o_{\mathrm{hi}} + o_{\mathrm{zb}}, \tag{16b}$$

leading to the resulting magnetometer measurement model (12). In deriving the model we have made two important assumptions.

First, the calibration matrix D and offset vector o in (16) are assumed to be time-independent. This implies that we assume that the magnetic distortions are constant and rigidly attached to the sensor. Also, the inertial and the magnetometer sensor axes are assumed to be rigidly attached to each other, i.e. their misalignment is represented by a constant rotation matrix. Additionally, in our algorithm we will assume that their misalignment can be described by a rotation matrix, i.e. that their axes are not mirrored with respect to each other.

Second, the local magnetic field m^{n} is assumed to be constant. In outdoor environments, this typically is a physically reasonable assumption. In indoor environments, however, the local magnetic field can differ in different locations in the building and care should be taken to fulfill the assumption.

3.4 Parameter vector

The parameter vector θ to be estimated in (5) consists of the calibration matrix D, the offset vector o and the local earth magnetic field m^{n} as discussed in Section 3.3. Furthermore, the gyroscope bias δ_ω introduced in Section 3.1 and the noise covariance matrices Σ_ω, Σ_{a} and Σ_{m} of the three sensors are treated as unknown parameters to be estimated from data. The different components of the unknown parameters θ therefore consist of

$$D \in \mathbb{R}^{3\times 3}, \tag{17a}$$

$$o \in \mathbb{R}^{3}, \tag{17b}$$

$$m^{\mathrm{n}} \in \{\mathbb{R}^3 : \|m^{\mathrm{n}}\|_2^2 = 1, m_x^{\mathrm{n}} > 0, m_y^{\mathrm{n}} = 0\}, \tag{17c}$$

$$\delta_\omega \in \mathbb{R}^{3}, \tag{17d}$$

$$\Sigma_\omega \in \{\mathbb{R}^{3\times 3} : \Sigma_\omega \succeq 0, \Sigma_\omega = \Sigma_\omega^{\mathsf{T}}\}, \tag{17e}$$

$$\Sigma_{\mathrm{a}} \in \{\mathbb{R}^{3\times 3} : \Sigma_{\mathrm{a}} \succeq 0, \Sigma_{\mathrm{a}} = \Sigma_{\mathrm{a}}^{\mathsf{T}}\}, \tag{17f}$$

$$\Sigma_{\mathrm{m}} \in \{\mathbb{R}^{3\times 3} : \Sigma_{\mathrm{m}} \succeq 0, \Sigma_{\mathrm{m}} = \Sigma_{\mathrm{m}}^{\mathsf{T}}\}, \tag{17g}$$

where m_x^{n} and m_y^{n} denote the x- and y- component of m^{n}, respectively. The notation $\Sigma \succeq 0$ denotes the assumption that the matrix Σ is positive semi-definite.

Although (17c) and (17e) – (17g) suggest that constrained optimization is needed, it is possible to circumvent this via suitable reparametrizations. The covariance matrices can be parametrized in terms of their Cholesky factorization, leading to only 6 parameters for each 3×3 covariance matrix. The local magnetic field can be parametrized using only one parameter as in (11). Note that in our algorithm we prefer using the representation (11a) for the initialization, but the representation (11b) for the maximum likelihood problem (5). Although the latter parametrization does not account for the constraint $m_x^{\mathrm{n}} > 0$, this is of no concern due to proper initialization.

4 Finding good initial estimates

Since the optimization problem is non-convex, the parameter vector θ introduced in Section 3.4 needs proper initialization. An initial estimate $\widehat{\theta_0}$ is obtained using a three-step method. As a first step, the gyroscope bias δ_ω and the noise covariances of the inertial sensors Σ_ω, Σ_{a} and of the magnetometer Σ_{m} are initialized. This can be done using a short batch of stationary data. Another option is to initialize them based on prior sensor information. As a second step, described in Section 4.1, an ellipse fitting problem is solved using the magnetometer data. As described in Section 1, this can map the ellipsoid of data to a sphere but it can not determine the rotation of the sphere. The rotation of the sphere is therefore determined in a third step of the initialization. This step also determines an initial estimate of the local magnetic field.

4.1 Ellipse fitting

As discussed in Section 1, we assume without loss of generality that the norm of the local magnetic field $\|m^{\mathrm{n}}\|$ is equal to 1. Based on this assumption we would expect all measurements to lie on the unit sphere,

$$\begin{aligned} \|m^{\mathrm{n}}\|_2^2 - 1 &= \|R_t^{\mathrm{bn}} m^{\mathrm{n}}\|_2^2 - 1 \\ &= \|D^{-1}\left(y_{\mathrm{m},t} - o - e_{\mathrm{m},t}\right)\|_2^2 - 1 = 0. \end{aligned} \tag{18}$$

In practice, the measurements are corrupted by noise and the equality (18) does not hold exactly. The ellipse fitting problem can therefore be written as

$$y_{\mathrm{m},t}^{\mathsf{T}} A y_{\mathrm{m},t} + b^{\mathsf{T}} y_{\mathrm{m},t} + c \approx 0, \tag{19}$$

with

$$A \triangleq D^{-\mathsf{T}} D^{-1}, \tag{20a}$$

$$b \triangleq -2 o^{\mathsf{T}} D^{-\mathsf{T}} D^{-1}, \tag{20b}$$

$$c \triangleq o^{\mathsf{T}} D^{-\mathsf{T}} D^{-1} o. \tag{20c}$$

Assuming that the matrix A is positive definite, this can be recognized as the definition of an ellipsoid with parameters A, b and c (see e.g. Gander et al. (1994)). We can rewrite (19) as a linear relation of the parameters as

$$M\xi \approx 0, \tag{21}$$

with

$$M = \begin{pmatrix} y_{\mathrm{m},1} \otimes y_{\mathrm{m},1} & y_{\mathrm{m},1} & 1 \\ y_{\mathrm{m},1} \otimes y_{\mathrm{m},2} & y_{\mathrm{m},2} & 1 \\ \vdots & \vdots & \vdots \\ y_{\mathrm{m},N} \otimes y_{\mathrm{m},N} & y_{\mathrm{m},N} & 1 \end{pmatrix}, \quad \xi = \begin{pmatrix} \operatorname{vec} A \\ b \\ c \end{pmatrix}, \tag{22}$$

where $\otimes$ denotes the Kronecker product and vec denotes the vectorization operator. This problem has infinitely many solutions and without constraining the length of the vector ξ, the trivial solution $\xi = 0$ would be obtained. A possible approach to solve the ellipse fitting problem is to make use of a singular value decomposition (Gander et al., 1994; Kok et al., 2012). This approach inherently poses a length constraint on the vector ξ, assuming that its norm is equal to 1. It does, however, not guarantee positive definiteness of the matrix A. Although positive definiteness of A is not guaranteed, there are only very few practical scenarios in which the estimated matrix A will not be positive definite. A non-positive definite matrix A can for instance be obtained in cases of very limited rotation of the sensor. The problem of allowing a non-positive definite matrix A can be circumvented by solving the ellipse fitting problem as a semidefinite program (Calafiore, 2002; Boyd and Vandenberghe, 2004)

$$\begin{aligned} \min_{A,b,c} \quad & \tfrac{1}{2} \| M \begin{pmatrix} \operatorname{vec} A \\ b \\ c \end{pmatrix} \|_2^2, \\ \text{s.t.} \quad & \operatorname{Tr} A = 1, \\ & A \in \mathcal{S}_{++}^{3\times 3}, \end{aligned} \tag{23}$$

where $\mathcal{S}_{++}^{3\times 3}$ denotes the set of 3×3 positive definite symmetric matrices. By constraining the trace of the matrix A, (23) avoids the trivial solution of $\xi = 0$. The problem (23) is a convex optimization problem and therefore has a globally optimal solution and does not require an accurate initial guess of the parameter vector ξ. The optimization problem can easily be formulated and efficiently solved using software packages like YALMIP (Löfberg, 2004) or CVX (Grant and Boyd, 2013).

Initial estimates of the calibration matrix D and offset vector o can be obtained from the estimated $\widehat{A}, \widehat{b}, \widehat{c}$ as

$$\alpha = \left(\tfrac{1}{4} \widehat{b}^{\mathsf{T}} \widehat{A}^{-1} \widehat{b} - \widehat{c} \right)^{-1}, \tag{24a}$$

$$\widetilde{D}_0^{\mathsf{T}} \widetilde{D}_0 = \alpha \widehat{A}^{-1}, \tag{24b}$$

$$\widehat{o}_0 = \tfrac{1}{2} \widehat{A}^{-1} \widehat{b}, \tag{24c}$$

where $\widehat{o}_0$ denotes the initial estimate of the offset vector o. From (24b) it is not possible to uniquely determine the initial estimate of the calibration matrix D. We determine an initial estimate of the calibration matrix D using a Cholesky decomposition, leading to a lower triangular $\widetilde{D}_0$. However, any $\widetilde{D}_0 U$ where $U U^{\mathsf{T}} = \mathcal{I}_3$ will also fulfill (24b). As described in Section 3.3, we assume that the sensor axes of the inertial sensors and the magnetometers are related by a rotation, implying that we restrict the matrix U to be a rotation matrix. The initial estimate $\widehat{D}_0$ can therefore be defined in terms of $\widetilde{D}_0$ as

$$\widehat{D}_0 = \widetilde{D}_0 R_{\mathrm{D}}. \tag{25}$$

The unknown rotation matrix R_{D} will be determined in Section 4.2.

4.2 Determine misalignment of the inertial and magnetometer sensor axes

The third step of the initial estimation aims at determining the misalignment between the inertial and magnetometer sensor axes. It also determines an initial estimate of the local magnetic field $\widehat{m}_0^{\mathrm{n}}$. These estimates are obtained by combining the magnetometer with the inertial sensor measurements. The approach is based on the fact that the inner product of two vectors is invariant under rotation. The two vectors considered here are the vertical $v^{\mathrm{n}} = \begin{pmatrix} 0 & 0 & 1 \end{pmatrix}^{\mathsf{T}}$ and the local magnetic field m^{n}. Hence, it is assumed that the inner product of the vertical v_t^{b} in the body frame b,

$$v_t^{\mathrm{b}} = R_t^{\mathrm{bn}} v^{\mathrm{n}}, \tag{26a}$$

and the local magnetic field m_t^{b} in the body frame,

$$m_t^{\mathrm{b}} = R_{\mathrm{D}}^{\mathsf{T}} \widetilde{D}_0^{-1} \left(y_{\mathrm{m},t} - \widehat{o}_0 \right), \tag{26b}$$

is constant. The matrix R_{D} in (26b) denotes the rotation needed to align the inertial and magnetometer sensor axes. The rotation matrices R_t^{nb} in (26a) can be estimated using an EKF. This EKF can not use the magnetometer measurements, since they have not properly been calibrated yet. It can therefore not be expected to result in accurate heading estimates. However, to determine the vertical v_t^{b}, only the sensor's inclination is of concern, which can be determined using the inertial measurements only.

The inner product between the vertical and the local magnetic field is equal to m_z^{n} (recall Figure 2. Using the assumption that this is invariant under rotation leads to the following minimization problem

$$\begin{aligned} \min_{R_{\mathrm{D}}, m_{z,0}^{\mathrm{n}}} \quad & \tfrac{1}{2} \sum_{t=1}^{N} \| m_{z,0}^{\mathrm{n}} - (v^{\mathrm{n}})^{\mathsf{T}} R_t^{\mathrm{nb}} R_{\mathrm{D}}^{\mathsf{T}} \widetilde{D}_0^{-1} \left(y_{\mathrm{m},t} - \widehat{o}_0 \right) \|_2^2 \\ \text{s.t.} \quad & R_{\mathrm{D}} \in SO(3), \end{aligned} \tag{27}$$

where $SO(3)$ refers to the special orthogonal group in three dimensions. The rotation matrix can be parametrized using an orientation deviation from a linearization point as described in Section 3. Hence, (27) can be solved as an unconstrained optimization problem.

Based on these results and (25) we obtain the initial estimates

$$\widehat{D}_0 = \widetilde{D}_0^{-1} \widehat{R}_{\mathrm{D}}, \tag{28a}$$

$$\widehat{m}_0^{\mathrm{n}} = \begin{pmatrix} \sqrt{1 - \left(\widehat{m}_{z,0}^{\mathrm{n}}\right)^2} & 0 & \widehat{m}_{z,0}^{\mathrm{n}} \end{pmatrix}^{\mathsf{T}}. \tag{28b}$$

Hence, we have obtained an initial estimate $\widehat{\theta}_0$ of the parameter vector θ as introduced in Section 3.4.

5 Calibration algorithm

The initial estimate from Section 4 can be used as a starting point to obtain a maximum likelihood estimate of the parameters θ in (5). The resulting calibration algorithm is described in Algorithm 1.

The actual optimization problem (5) is solved in Step 2b of Algorithm 1. It uses a Broyden-Fletcher-Goldfarb-Shanno (BFGS) method using damped BFGS updating (Nocedal and Wright, 2006). Since the predicted measurement $\widehat{y}_{t|t-1}$ and the residual covariance S_t are determined using an EKF, determining the gradient of the objective function (5) is not straightforward. Possible approaches are discussed in Åström (1980); Segal and Weinstein (1989) for the case of linear models. In the case of nonlinear models, however, they only lead to approximate gradients. Because of this, our approach uses numerical gradients, requiring running $n_\theta + 1$ EKFs each iteration. Although this is computationally rather expensive, the computation of the numerical gradients can be parallelized.

Algorithm 1 Magnetometer and inertial calibration

```
1. Determine an initial parameter estimate $\widehat{D}_0, \widehat{o}_0, \widehat{m}_0^{\mathrm{n}}, \widehat{\delta}_{\omega,0}, \widehat{\Sigma}_{\omega,0}, \widehat{\Sigma}_{\mathrm{a},0}, \widehat{\Sigma}_{\mathrm{m},0}$ using three steps
   (a) Initialize $\widehat{\delta}_{\omega,0}, \widehat{\Sigma}_{\omega,0}, \widehat{\Sigma}_{\mathrm{a},0}, \widehat{\Sigma}_{\mathrm{m},0}$.
   (b) Obtain an initial $\widetilde{D}_0$ and $\widehat{o}_0$ based on ellipse fitting (see Section 4.1).
   (c) Obtain initial $\widehat{D}_0, \widehat{o}_0$ and $\widehat{m}_0^{\mathrm{n}}$ by initial determination of the sensor axis misalignment (see Section 4.2).
2. Set $i = 0$ and repeat,
   (a) Run the EKF using the current estimates $\widehat{D}_i, \widehat{o}_i, \widehat{m}_i^{\mathrm{n}}, \widehat{\delta}_{\omega,i}, \widehat{Q}_i = \widehat{\Sigma}_{\omega,i}, \widehat{R}_i = \begin{pmatrix} \widehat{\Sigma}_{\mathrm{a},i} & 0_{3\times3} \\ 0_{3\times3} & \widehat{\Sigma}_{\mathrm{m},i} \end{pmatrix}$ and obtain $\{\widehat{y}_{t|t-1}\}_{t=1}^{N}, S_{1:N}$.
   (b) Determine $\widehat{\theta}_{i+1}$ using the numerical gradient of the objective function in (5), its approximate Hessian and a line search algorithm.
   (c) Obtain $\widehat{D}_{i+1}, \widehat{o}_{i+1}, \widehat{m}_{i+1}^{\mathrm{n}}, \widehat{\delta}_{\omega,i+1}, \widehat{\Sigma}_{\omega,i+1}, \widehat{\Sigma}_{\mathrm{a},i+1}, \widehat{\Sigma}_{\mathrm{m},i+1}$ from $\widehat{\theta}_{i+1}$.
   (d) Set $i := i + 1$ and repeat from Step 2a until convergence.
```

6 Minimum rotation needed

For magnetometer calibration, the sensor needs to be rotated in all possible orientations so the magnetometer measurements describe (a part of) an ellipsoid. Work on magnetometer calibration generally assumes that the sensor can be "sufficiently" rotated for the calibration parameters to be identified. Often, however, magnetometers are mounted in such a way that their movement is more or less constrained to the 2D plane (Wu et al., 2013a,b). We will study how much rotation is actually needed to solve the magnetometer calibration problem using an identifiability analysis. Here, we will assume noise-free and bias-free inertial measurements and noise-free magnetometer measurements. Note that because of these assumptions, our analysis provides a lower bound on the number of measurements needed to identify the calibration parameters. In most applications with limited rotational freedom, rotations around the z-axis are possible, while rotations around the other axes are constrained. We therefore ask the question of how much rotation around the x- and y-axes is needed in addition to rotation around the z-axis. We are hence interested in when a subset of the parameters θ, namely the calibration parameters $\theta_{\mathrm{c}} = \begin{pmatrix} \operatorname{vec} D & o^{\mathsf{T}} & m_z^{\mathrm{n}} \end{pmatrix}^{\mathsf{T}}$, become identifiable.

6.1 Identifiability analysis

Identifiability analysis can be performed by studying local observability of an extended system (Walter, 1982). The extended system consists of the state variables $x_{1:K}$ during a certain time period (see (1a)) and the parameters θ. For our problem, the size of this problem can be reduced by recognizing that assuming noise-free and bias-free gyroscope measurements, the orientation difference between two time steps can be determined from (6). Furthermore, assuming perfect accelerometer measurements combined with the assumption in (9), the inclination at each time step is known. Since the magnetometer measurements are assumed to be uncalibrated, the initial heading denoted by ψ can not be assumed to be known. Based on this knowledge we can reduce our observability analysis to the study of the calibration parameters θ_{c} and the initial heading ψ.

Discrete-time observability analysis considers the system of equations

$$y_{\mathrm{m},1} = D R_1^{\mathrm{bn}}(\psi) m^{\mathrm{n}} + o = h_{\mathrm{m}}(R_1^{\mathrm{bn}}, \psi, \theta_{\mathrm{c}}), \tag{29a}$$

$$y_{\mathrm{m},2} = D R_2^{\mathrm{bn}}(\psi) m^{\mathrm{n}} + o = h_{\mathrm{m}}(R_2^{\mathrm{bn}}, \psi, \theta_{\mathrm{c}}), \tag{29b}$$

$$\vdots$$

$$y_{\mathrm{m},K} = D R_K^{\mathrm{bn}}(\psi) m^{\mathrm{n}} + o = h_{\mathrm{m}}(R_K^{\mathrm{bn}}, \psi, \theta_{\mathrm{c}}). \tag{29c}$$

The parameters θ_{c} and ψ are said to be *locally identifiable* if there exists an $R_{1:K}^{\mathrm{bn}}$ such that we can solve for θ_{c} and ψ in (29).

Due to the nonlinear nature of (29) it is typically hard to analyze it directly. Instead, observability is often studied by considering a linearized version of (29), making use of the Jacobian

$$\mathcal{J}(\theta_\mathrm{c}, \psi) = \begin{pmatrix} \nabla h_\mathrm{m}(R_1^\mathrm{bn}, \psi, \theta_\mathrm{c}) \\ \nabla h_\mathrm{m}(R_2^\mathrm{bn}, \psi, \theta_\mathrm{c}) \\ \vdots \\ \nabla h_\mathrm{m}(R_K^\mathrm{bn}, \psi, \theta_\mathrm{c}) \end{pmatrix}, \tag{30}$$

where ∇ denotes the derivative with respect to θ_c and ψ. If (30) is full rank, i.e. equal to 14, for all θ_c, ψ, the parameters are said to be *locally weakly identifiable* (Nijmeijer and van der Schaft, 1990).

The Jacobian $\mathcal{J}(\theta_\mathrm{c}, \psi)$ can be built by stacking different measurements on top of each other. For notational simplicity, we consider 90° rotations around the axes. Note that the analysis is equally valid for any other amount of rotation. For rotations of 0°, 90° and −90° around the z-axis, 90° and −90° around the x-axis and 90° and −90° around the y-axis, the Jacobian is given by

$$\mathcal{J}(\theta_\mathrm{c}, \psi) = \begin{array}{c} \left(\begin{array}{cccccc} m_x \mathrm{c}_\psi \mathcal{I}_3 & m_x \mathrm{s}_\psi \mathcal{I}_3 & m_z \mathcal{I}_3 & \mathcal{I}_3 & D_3 + (D_1 \mathrm{c}_\psi + D_2 \mathrm{s}_\psi)\frac{\partial m_x}{\partial m_z} & (D_2 \mathrm{c}_\psi - D_1 \mathrm{s}_\psi) m_x \\ -m_x \mathrm{s}_\psi \mathcal{I}_3 & m_x \mathrm{c}_\psi \mathcal{I}_3 & m_z \mathcal{I}_3 & \mathcal{I}_3 & D_3 + (D_2 \mathrm{c}_\psi - D_1 \mathrm{s}_\psi)\frac{\partial m_x}{\partial m_z} & -(D_1 \mathrm{c}_\psi + D_2 \mathrm{s}_\psi) m_x \\ m_x \mathrm{s}_\psi \mathcal{I}_3 & -m_x \mathrm{c}_\psi \mathcal{I}_3 & m_z \mathcal{I}_3 & \mathcal{I}_3 & D_3 + (D_1 \mathrm{s}_\psi - D_2 \mathrm{c}_\psi)\frac{\partial m_x}{\partial m_z} & (D_1 \mathrm{c}_\psi + D_2 \mathrm{s}_\psi) m_x \\ \hdashline m_x \mathrm{c}_\psi \mathcal{I}_3 & -m_z \mathcal{I}_3 & m_x \mathrm{s}_\psi \mathcal{I}_3 & \mathcal{I}_3 & -D_2 + (D_1 \mathrm{c}_\psi + D_3 \mathrm{s}_\psi)\frac{\partial m_x}{\partial m_z} & (D_3 \mathrm{c}_\psi - D_1 \mathrm{s}_\psi) m_x \\ m_x \mathrm{c}_\psi \mathcal{I}_3 & m_z \mathcal{I}_3 & -m_x \mathrm{s}_\psi \mathcal{I}_3 & \mathcal{I}_3 & D_2 + (D_1 \mathrm{c}_\psi - D_3 \mathrm{s}_\psi)\frac{\partial m_x}{\partial m_z} & -(D_3 \mathrm{c}_\psi + D_1 \mathrm{s}_\psi) m_x \\ \hdashline m_z \mathcal{I}_3 & m_x \mathrm{s}_\psi \mathcal{I}_3 & -m_x \mathrm{c}_\psi \mathcal{I}_3 & \mathcal{I}_3 & D_1 + (D_2 \mathrm{s}_\psi - D_3 \mathrm{c}_\psi)\frac{\partial m_x}{\partial m_z} & (D_2 \mathrm{c}_\psi + D_3 \mathrm{s}_\psi) m_x \\ -m_z \mathcal{I}_3 & m_x \mathrm{s}_\psi \mathcal{I}_3 & m_x \mathrm{c}_\psi \mathcal{I}_3 & \mathcal{I}_3 & -D_1 + (D_2 \mathrm{s}_\psi + D_3 \mathrm{c}_\psi)\frac{\partial m_x}{\partial m_z} & (D_2 \mathrm{c}_\psi - D_3 \mathrm{s}_\psi) m_x \end{array}\right) \\ \underbrace{\hphantom{m_x \mathrm{c}_\psi \mathcal{I}_3 \quad -m_x \mathrm{s}_\psi \mathcal{I}_3 \quad -m_x \mathrm{c}_\psi \mathcal{I}_3}}_{\operatorname{vec} D} \quad \underbrace{\hphantom{\mathcal{I}_3}}_{o} \quad \underbrace{\hphantom{-D_1 + (D_2 \mathrm{s}_\psi + D_3 \mathrm{c}_\psi)\frac{\partial m_x}{\partial m_z}}}_{m_z} \quad \underbrace{\hphantom{-(D_3 \mathrm{c}_\psi + D_1 \mathrm{s}_\psi) m_x}}_{\psi} \end{array}, \tag{31}$$

where D_i denotes the i^th column of the matrix D and the superscript n for the local magnetic field m^n is omitted. The notation c_ϕ and s_ϕ denotes $\cos\phi$ and $\sin\phi$, respectively. For clarity, the contributions of the different rotation axes are separated by dashed lines. For each column it is explicitly indicated which part of the derivative with respect to the parameters θ_c, ψ it represents.

The rank of (31) can be studied for subsets of its rows. Considering only rotations around the z-axis, i.e. the first three rows in (31), $\operatorname{rank} \mathcal{J}(\theta_\mathrm{c}, \psi) = 9$ as long as $m_x^\mathrm{n} \neq 0$ (the calibration is not performed on the magnetic north or south pole). The matrix will not gain any rank from adding more measurements around the z-axis. The minimum amount of measurements around the different axes that lead to $\operatorname{rank} \mathcal{J}(\theta_\mathrm{c}, \psi) = 14$ is summarized in Table 1. For instance, in case the calibration is not performed on the equator or on one of the magnetic poles, it is enough to supplement the 3 measurements around the z-axis with two measurements around another axis. Hence, this leads to three possible combinations as represented by the three columns in Table 1 under "elsewhere". On the equator, however, for the calibration parameters to be identifiable it is necessary to have at least one measurement from rotation around the y-axis. Hence, there are only

Table 1: *Summary of how many measurements (i.e. lower bound) around which axes are needed for identifiability of the calibration parameters θ_c and the initial heading ψ.*

$\mathcal{J}(\theta_c, \psi)$ **full rank**	**Pole**	**Equator**		**Elsewhere**		
#meas z-axis	–	3	3	3	3	3
#meas x-axis	–	0	1	1	0	2
#meas y-axis	–	2	1	1	2	0

two possible combinations for the lower bound for identifiability. Note that on the magnetic poles, the calibration parameters are identifiable from a finite set of measurements, as discussed in Kok and Schön (2014a). However, the initial heading ψ is not identifiable at these locations since the local magnetic field here consists of a vertical component only. The results in Table 1 are valid under very mild conditions on the calibration matrix D. A sufficient condition for this is that $\det D \neq 0$.

6.2 Quality of the estimates

The identifiability analysis above was performed assuming 90° rotations between each measurement. The same result holds, however, for any other difference in rotations. Although the amount of rotation does not influence the identifiability of the calibration parameters, it will indeed influence the quality of the estimates. This can be understood in terms of the condition number (Kailath et al., 2000), i.e. the ratio between the maximum and minimum singular value of the Jacobian (31). Any singular values being zero implies that θ_c is not identifiable, but a smaller condition number also implies that certain parameters are more difficult to estimate. Figure 3 shows the singular values of the Jacobian in (31) for different amounts of rotation. Five measurements are considered, corresponding to three measurements around the z-axis, one around the x-axis and one around the y-axis for $D = \mathcal{I}_3$, $o = \begin{pmatrix} 0 & 0 & 0 \end{pmatrix}^\mathsf{T}$ and the local magnetic field m^n equal to that in Linköping, Sweden. The amount of rotation between the measurements is assumed to be equal for all four differences and is varied between 0° (red) and 90° (blue). As can be seen, the larger the amount of rotation, the smaller the condition number of (31).

It can hence be concluded that rotation around the z-axis only is never enough to identify the calibration parameters θ_c. The parameters will, however, become identifiably already with very little excitation in the other directions as summarized in Table 1. More excitation around the different axes will always lead to better estimates as can be concluded from Figure 3.

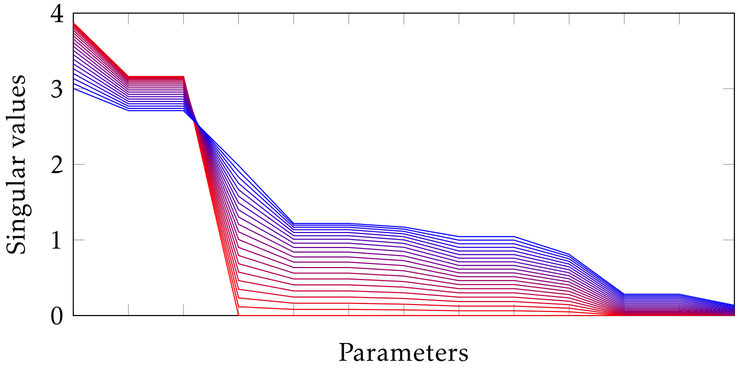

Figure 3: *Singular values of the Jacobian in* (31) *for small rotation ranges (red) to large rotation ranges (blue).*

7 Experiments and results

7.1 Experimental setup

Experiments have been performed using two commercially available inertial measurements units (IMUs), an Xsens MTi-100 (Xsens Technologies B.V., 2013) and a Trivisio Colibri Wireless IMU (Trivisio Prototyping GmbH, 2014). The experimental setup of both experiments can be found in Figure 4. The experiment with the Xsens IMU was performed outdoors to ensure a homogeneous local magnetic field. The experiment with the Trivisio IMU was performed indoors. However, the experiment was performed relatively far away from any magnetic materials such that the local magnetic field is as homogenous as possible. The Xsens IMU was placed in an aluminum block with right angles which can be used to rotate the sensor 90° to verify the heading results. For both sensors, inertial and magnetometer measurements were collected at 100 Hz.

7.2 Calibration results

For calibration, the IMU needs to be slowly rotated such that the assumption of zero acceleration is reasonably valid. This leads to an ellipsoid of magnetometer data as depicted in red in Figures 1 and 5. Note that for plotting purposes the data has been downsampled to 1 Hz. To emphasize the deviation of the norm from 1, the norm of the magnetometer data is depicted in red in Figure 6.

For the experiment with the Xsens IMU, the following calibration matrix $\widehat{D}$ and offset vector $\widehat{o}$ are found

$$\widehat{D} = \begin{pmatrix} 0.74 & -0.13 & 0.01 \\ -0.12 & 0.68 & 0.01 \\ -0.03 & 0.43 & 1.00 \end{pmatrix}, \quad \widehat{o} = \begin{pmatrix} 1.36 \\ 1.22 \\ -0.94 \end{pmatrix}, \tag{32}$$

using Algorithm 1. Applying the calibration result to the magnetometer data

Figure 4: *Left: experimental setup where a calibration experiment is performed outdoors. An Xsens MTi-100 IMU (orange box) together with a magnetic disturbance is placed in a aluminum block. Right: experimental setup using a Trivisio IMU (black box). A phone is used as a source of magnetic disturbance. To avoid saturation of the magnetometer, the phone is not attached directly to the IMU.*

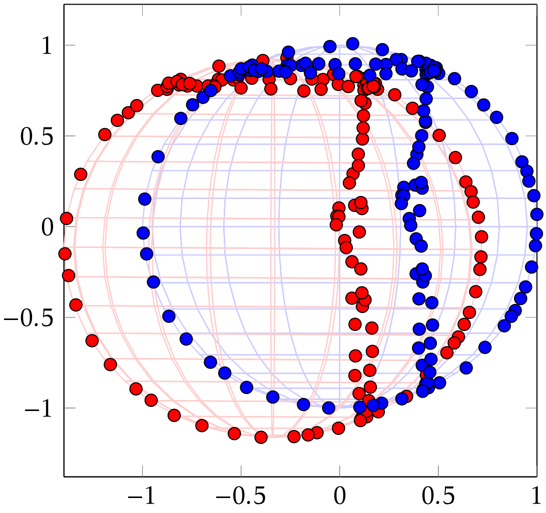

Figure 5: *Calibration results from the experiment with the Trivisio IMU. The ellipsoid of magnetometer data (red) lies on a unit sphere after calibration (blue).*

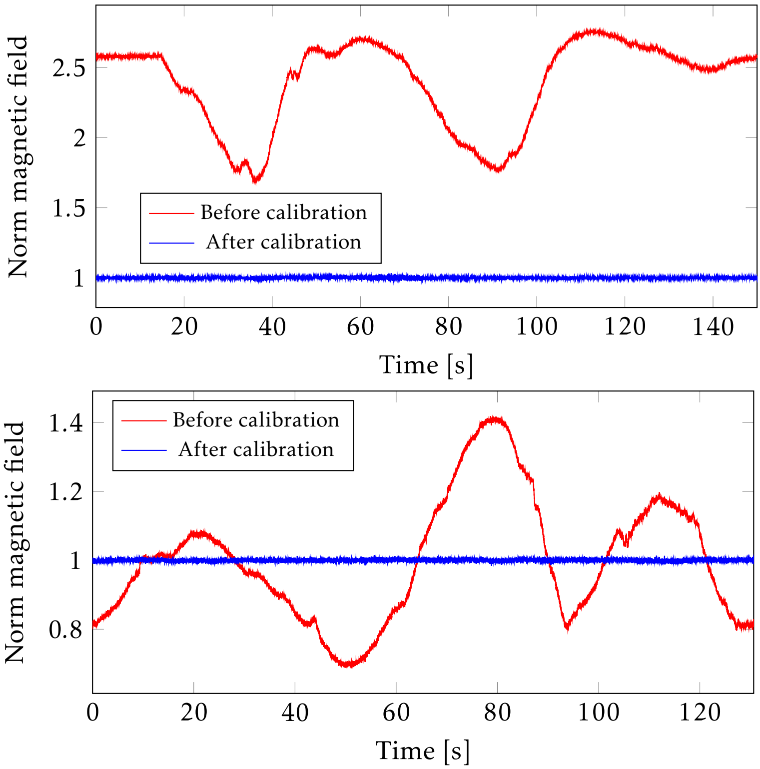

Figure 6: *Norm of the magnetic field measurements before (red) and after (blue) calibration for (top) the experiment with the Xsens IMU and for (bottom) the experiment with the Trivisio IMU.*

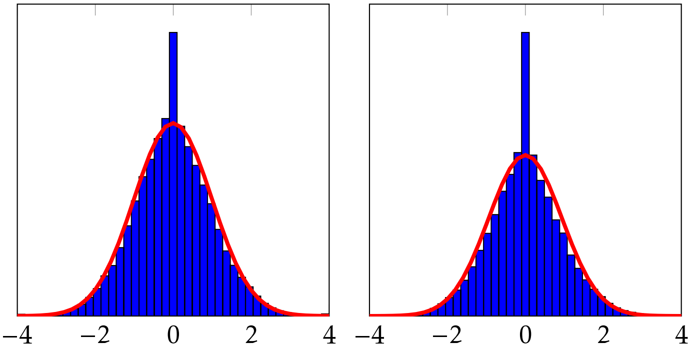

Figure 7: *Histogram of the normalized residuals* $S_t^{-1/2}(y_t - \widehat{y}_{t|t-1})$ *from the EKF after calibration for the original data set (left) and for a second data set (right) for the experiments performed with the Xsens IMU. A Gaussian distribution (red) is fitted to the data.*

leads to the unit sphere of data in blue in Figure 1. The norm of the magnetometer data after calibration can indeed be seen to lie around 1, as depicted in blue in Figure 6.

As a measure of the calibration quality, we analyze the normalized residuals $S_t^{-1/2}(y_t - \widehat{y}_{t|t-1})$ after calibration from the EKF. In the case of correct calibrated parameters that sufficiently model the magnetic disturbances, we expect the normalized residuals to be normally distributed with zero mean and standard deviation 1. According to Figure 7 this is more or less the case.

To analyze if the calibration is also valid for a different data set with the same experimental setup, the calibrated parameters have been used on a second data set. Figures of the ellipsoid of magnetometer data and the sphere of calibrated magnetometer data are not included since they look very similar to Figures 1 and 6. The normalized residuals $S_t^{-1/2}(y_t - \widehat{y}_{t|t-1})$ of this second data set, however, can be found in Figure 7 (right plot). They can be seen to still look fairly $\mathcal{N}(0, 1)$. From these results it can be concluded that the calibration can well be applied to other data sets if the same magnetic disturbance is present.

The Trivisio IMU outputs the magnetometer data in microtesla. Since our algorithm scales the calibrated measurements to a unit norm, the obtained $\widehat{D}$ and offset vector $\widehat{o}$ from Algorithm 1 are in this case of much larger magnitude,

$$\widehat{D} = \begin{pmatrix} 61.74 & 0.59 & 0.09 \\ -1.01 & 60.74 & 0.23 \\ -0.39 & 0.06 & 60.80 \end{pmatrix}, \quad \widehat{o} = \begin{pmatrix} -19.77 \\ -1.68 \\ -6.98 \end{pmatrix}. \tag{33}$$

The sphere of calibrated data and its norm can be found in blue in Figures 5 and 6. Note that for plotting purposes, the magnetometer data before calibration is scaled down such that its mean lies around 1. The obtained $\widehat{D}$ and $\widehat{o}$ are scaled accordingly to plot the red ellipsoid in Figure 5. The normalized residu-

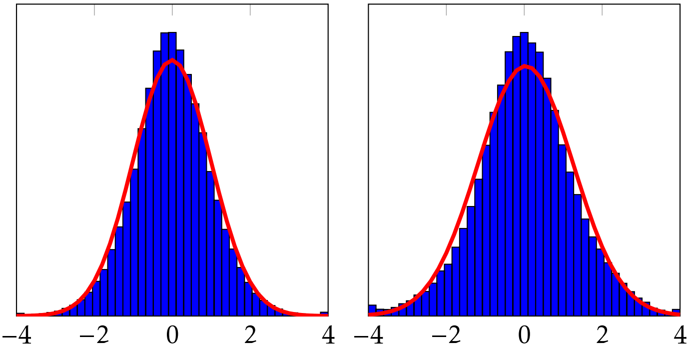

Figure 8: *Histogram of the normalized residuals* $S_t^{-1/2}(y_t - \widehat{y}_{t|t-1})$ *from the EKF after calibration for the original data set (left) and for a second data set (right) for the experiments performed with the Trivisio IMU. A Gaussian distribution (red) is fitted to the data.*

als $S_t^{-1/2}(y_t - \widehat{y}_{t|t-1})$ of the EKF using both the original and a second data set are depicted in Figure 8 and can be seen to be more or less $\mathcal{N}(0, 1)$.

From these results we can conclude that Algorithm 1 gives good magnetometer calibration results for experimental data from two different commercially available IMUs. A good fit of the ellipsoid of data to a sphere is obtained and the algorithm seems to give good estimates analyzed in terms of its normalized residuals. Since magnetometer calibration is generally done to obtain improved heading estimates, it is important to also interpret the quality of the calibration in terms of the resulting heading estimates. In Section 7.3 this will be done based on experimental results. The heading performance will also be analyzed based on simulations in Section 8.

7.3 Heading estimation

An important goal of magnetometer calibration is to facilitate good heading estimates. To check the quality of the heading estimates after calibration, the block in which the Xsens sensor was placed (shown in Figure 4) is rotated around all axes. This block has right angles and it can therefore be placed in 24 orientations that differ from each other by a 90° rotation. The calibrated magnetometer data of this experiment is shown in Figure 9. Orientation estimates are determined by computing the mean value of 500 magnetometer and accelerometer samples in each orientation and using the accelerometer to estimate the sensor's inclination and the magnetometer data to estimate its heading. After calibration, we expect the difference of the estimated heading between each subsequent rotation to be 90°. Note that when rotating around an axis, the sensor is always rotated back to its initial position, enabling the computation of 4 orientation differences per rotation axis. Table 2 reports the deviation from 90° between two subsequent rotations. Note that the metal object causing the magnetic disturbance as shown

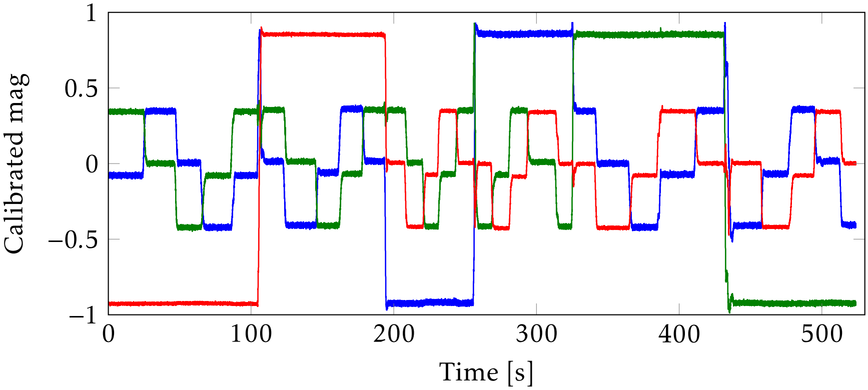

Figure 9: *Calibrated magnetometer data of an experiment rotating the sensor into 24 different sensor orientations where the blue, green and red lines represent the data from the x-, y- and z-axis of the magnetometer, respectively.*

in Figure 4 physically prevents the setup from being properly placed in all orientations around the y-axis. Rotation around the y-axis with the y-axis pointing upwards has therefore not been included in Table 2.

Our experiment investigates both the absolute heading errors and the improvement of the heading estimates over the ones obtained after the initial calibration, i.e. Step 1 in Algorithm 1. In Table 2 we therefore include both the orientation errors using the initial parameter estimates $\widehat{D}_0$ (28a) and $\widehat{o}_0$ (24c) and the orientation errors using maximum likelihood parameter estimates $\widehat{D}$ and $\widehat{o}$ (32) obtained using Algorithm 1. As can be seen, the deviation from 90° is small, indicating that good heading estimates are obtained after calibration. Also, the heading estimates using the initial parameter estimates are already fairly good. The mean orientation error is reduced from 1.28° for the initial estimate to 0.76° for the maximum likelihood estimate. The maximum error is reduced from 4.36° for the initial estimate to 2.48° for the maximum likelihood estimate. Note that the results of maximum likelihood estimate are slightly better than the results previously reported by Kok and Schön (2014a). This can be attributed to the fact that we now use orientation error states instead of the quaternion states in the EKF (see Section 3). This results in slightly better estimates, but also in a smoother convergence of the optimization problem. The quality of the heading estimates is studied further in Section 8 based on a simulation study.

8 Simulated heading accuracy

Magnetometer calibration is typically performed to improve the heading estimates. It is, however, difficult to check the heading accuracy experimentally. One way is to do it is as in Section 7.3. There we are, however, limited to doing the

Table 2: *Difference in estimated heading between two subsequent rotations around the sensor axes using calibrated magnetometer data. The values represent the deviation in degrees from 90°. Included are both the results using the maximum likelihood (ML) estimates from Algorithm 1 and the results using initial estimates from Step 1 in the algorithm.*

z-axis				**x-axis**				**y-axis**	
z up		**z down**		**x up**		**x down**		**y down**	
ML	**init**	**ML**	**init**	**ML**	**init**	**ML**	**init**	**ML**	**init**
0.11	0.36	0.69	1.34	0.22	0.16	0.86	1.01	0.18	1.57
0.22	0.90	2.48	4.36	0.07	0.20	1.57	1.45	0.29	0.76
0.46	1.52	1.53	3.57	0.97	0.94	0.61	0.71	0.20	0.78
0.30	0.94	1.92	2.40	0.29	0.59	1.78	1.70	0.50	0.45

heading validation on a different data set and we have a limited number of available data points. To get more insight into the orientation accuracy that is gained by executing all of Algorithm 1, compared to just its initialization phase (Step 1 in the algorithm), we engage in a simulation study. In this study we focus on the root mean square (RMS) heading error for different simulated sensor qualities (in terms of the noise covariances and the gyroscope bias) and different magnetic field disturbances (in terms of different values for the calibration matrix D and offset vector o).

In our simulation study, we assume that the local magnetic field is equal to that in Linköping, Sweden. The calibration matrix D, the offset vector o and the sensor properties in terms of the gyroscope bias and noise covariances are all sampled from a uniform distribution. The parameters of the distributions from which the sensor properties are sampled are chosen as physically reasonable values as considered from the authors' experience. The noise covariance matrices Σ_ω, Σ_a and Σ_m are assumed to be diagonal with three different values on the diagonal. The calibration matrix D is assumed to consist of three parts,

$$D = D_\mathrm{diag} D_\mathrm{skew} D_\mathrm{rot}, \tag{34}$$

where D_diag is a diagonal matrix with elements D_{11}, D_{22}, D_{33} and D_rot is a rotation matrix around the angles ψ, θ, ϕ. The matrix D_skew models the non-orthogonality of the magnetometer axes as

$$D_\mathrm{skew} = \begin{pmatrix} 1 & 0 & 0 \\ \sin\zeta & \cos\zeta & \\ -\sin\eta & \cos\eta\sin\rho & \cos\eta\cos\rho \end{pmatrix}, \tag{35}$$

where the angles ζ, η, ρ represent the different non-orthogonality angles. The exact simulation conditions are summarized in Table 3.

The simulated data consists of 100 samples of stationary data and subsequently 300 samples for rotation around all three axes. It is assumed that the rotation is exactly around the origin of the accelerometer triad, resulting in zero acceleration

Table 3: *Settings used in the Monte Carlo simulation.*

$\boldsymbol{D}$			$\boldsymbol{o}$
$\boldsymbol{D}_{\text{diag}}$	$\boldsymbol{D}_{\text{skew}}$	$\boldsymbol{D}_{\text{rot}}$	
D_{11}, D_{22}, D_{33} $\in \mathcal{U}(0.5, 1.5)$	ζ, η, ρ $\in \mathcal{U}(-30°, 30°)$	ψ, θ, ϕ $\in \mathcal{U}(-10°, 10°)$	o_1, o_2, o_3 $\in \mathcal{U}(-1, 1)$

$\boldsymbol{\delta_\omega}$	$\boldsymbol{\Sigma_\omega}$	$\boldsymbol{\Sigma}_{\text{a}}$	$\boldsymbol{\Sigma}_{\text{m}}$
$\delta_{\omega,1}, \delta_{\omega,2}, \delta_{\omega,3}$ $\in \mathcal{U}(-1, 1)$	$\Sigma_{\omega,1}, \Sigma_{\omega,2}, \Sigma_{\omega,3}$ $\in \mathcal{U}(10^{-3}, 10^{-2})$	$\Sigma_{\text{a},1}, \Sigma_{\text{a},2}, \Sigma_{\text{a},3}$ $\in \mathcal{U}(10^{-3}, 10^{-1})$	$\Sigma_{\text{m},1}, \Sigma_{\text{m},2}, \Sigma_{\text{m},3}$ $\in \mathcal{U}(10^{-3}, 10^{-1})$

during the rotation. The first 100 samples are used to obtain an initial estimate of the gyroscope bias $\widehat{\delta}_{\omega,0}$ by computing the mean of the stationary gyroscope samples. The covariance matrices $\widehat{\Sigma}_{\omega,0}$, $\widehat{\Sigma}_{\text{a},0}$ and $\widehat{\Sigma}_{\text{m},0}$ are initialized based on the covariance of these first 100 samples. The initial estimate then consists of these initial estimates $\widehat{\delta}_{\omega,0}$, $\widehat{\Sigma}_{\omega,0}$, $\widehat{\Sigma}_{\text{a},0}$, $\widehat{\Sigma}_{\text{m},0}$ and the initial calibration matrix $\widehat{D}_0$ (28a), the initial offset vector $\widehat{o}_0$ (24c) and the initial estimate of the local magnetic field m^{n}_0 (28b).

To study the heading accuracy, the EKF as described in Section 3 is run with both the initial parameter values $\widehat{\theta}_0$ and their maximum likelihood values $\widehat{\theta}_{\text{ML}}$. The orientation errors are computed using

$$\Delta q_t = \widehat{q}^{\text{nb}}_t \odot \left(q^{\text{nb}}_{\text{ref},t}\right)^c, \tag{36}$$

where $\odot$ denotes a quaternion multiplication, the superscript denotes the quaternion conjugate c (see e.g. (Hol, 2011)), and Δq_t denotes the orientation error encoded as a unit quaternion. It is computed from the orientation $\widehat{q}^{\text{nb}}_t$ estimated by the EKF and the ground truth orientation $q^{\text{nb}}_{\text{ref},t}$. Computing the orientation errors in this way is equivalent to subtracting Euler angles in the case of small angles. However, it avoids subtraction problems due to ambiguities in the Euler angles representation. To interpret the orientation errors Δq_t, they are converted to Euler angles. We focus our analysis on the heading error, i.e. the third component of the Euler angles.

The RMS of the heading error is plotted for 150 Monte Carlo simulations in Figure 10. As can be seen, the heading RMSE using the estimate of the calibration parameters from Algorithm 1 is consistently small. The heading RMSE based on the initialization phase in Step 1 of the algorithm, however, has a significantly larger spread. This clearly shows that orientation accuracy can be gained by executing all of Algorithm 1. Note that in all simulations, analysis of the norm of the calibrated magnetometer measurements as done in Figure 6 does not indicate that the ML estimate is to be prefered over the estimate from the initialization phase. Hence, analysis of the norm of the calibrated magnetometer measurements does not seem to be a sufficient analysis to determine the quality of the calibration in the case when the calibration is performed to improve the heading estimates.

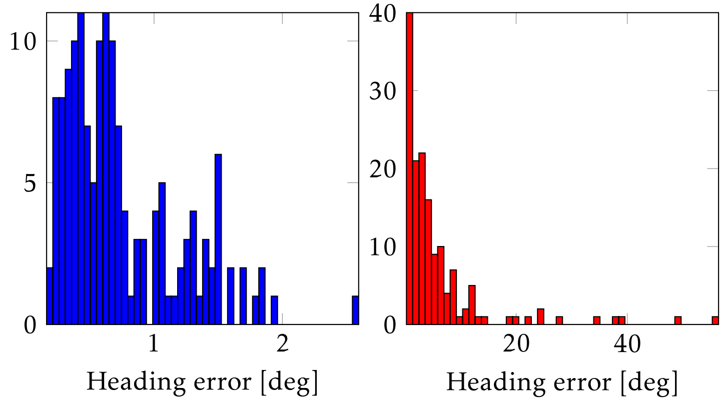

Figure 10: *Histogram of the heading RMSE using (left, blue) the maximum likelihood parameter estimate from Algorithm 1 and (right, red) the initial parameter estimate from Step 1 in the algorithm. Note the different scales in the two plots.*

9 Conclusions

We have developed a practical algorithm to calibrate a magnetometer using inertial sensors. It calibrates the magnetometer for the presence of magnetic disturbances, for magnetometer sensor errors and for misalignment between the inertial and magnetometer sensor axes. The problem is formulated as a maximum likelihood problem. The algorithm is shown to perform well on real data collected with two different commercially available inertial measurement units.

In future work the approach can be extended to include GPS measurements. In that case it is not necessary to assume that the acceleration is zero. The algorithm can hence be applied to a wider range of problems, like for instance the flight test example discussed in Kok et al. (2012). The computational cost of the algorithm would, however, increase, since to facilitate the inclusion of the GPS measurements the state vector in the EKF needs to be extended.

Acknowledgements

This work is supported by MC Impulse, a European Commission, FP7 research project and CADICS, a Linnaeus Center funded by the Swedish Research Council (VR). The authors would like to thank Laurens Slot, Dr. Henk Luinge and Dr. Jeroen Hol from Xsens Technologies and Dr. Gustaf Hendeby from Linköping University for their support in collecting the data sets and for interesting discussions.

Bibliography

R. Alonso and M. D. Shuster. Complete linear attitude-independent magnetometer calibration. *The Journal of the Astronautical Sciences*, 50(4):477–490, 2002.

K. J. Åström. Maximum likelihood and prediction error methods. *Automatica*, 16(5):551–574, 1980.

S. Bonnet, C. Bassompierre, C. Godin, S. Lesecq, and A. Barraud. Calibration methods for inertial and magnetic sensors. *Sensors and Actuators A: Physical*, 156(2):302–311, 2009.

S. Boyd and L. Vandenberghe. *Convex Optimization*. Cambridge University Press, 2004.

G. Calafiore. Approximation of n-dimensional data using spherical and ellipsoidal primitives. *IEEE Transactions on Systems, Man, and Cybernetics—Part A: Systems and Humans*, 32(2):269–278, 2002.

J. L. Crassidis, F. L. Markley, and Y. Cheng. A survey of nonlinear attitude estimation methods. *Journal of Guidance, Control, and Dynamics*, 30(1):12–28, 2007.

W. Gander, G. H. Golub, and R. Strebel. Least-squares fitting of circles and ellipses. *BIT Numerical Mathematics*, 34(4):558–578, 1994.

D. Gebre-Egziabher, G. H. Elkaim, J. D. Powell, and B. W. Parkinson. Calibration of strapdown magnetometers in magnetic field domain. *Journal of Aerospace Engineering*, 19(2):87–102, April 2006.

M. Grant and S. Boyd. CVX: Matlab software for disciplined convex programming, version 2.0 beta. `http://cvxr.com/cvx`, September 2013.

F. Gustafsson. *Statistical Sensor Fusion*. Studentlitteratur, 2012.

W. R. Hamilton. On quaternions; or on a new system of imaginaries in algebra. *Philosophical Magazine*, xxv, 1844.

J. D. Hol. *Sensor Fusion and Calibration of Inertial Sensors, Vision, Ultra-Wideband and GPS*. PhD thesis, Linköping University, Sweden, June 2011.

T. Kailath, A. H. Sayed, and B. Hassibi. *Linear estimation*. Prentice Hall, 2000.

M. Kok and T. B. Schön. Maximum likelihood calibration of a magnetometer using inertial sensors. In *Proceedings of the 19th World Congress of the International Federation of Automatic Control (accepted for publication)*, Cape Town, South Africa, August 2014a.

M. Kok and T. B. Schön. Magnetometer calibration using inertial sensors. *Preprint*, 2014b.

M. Kok, J. D. Hol, T. B. Schön, F. Gustafsson, and H. Luinge. Calibration of a magnetometer in combination with inertial sensors. In *Proceedings of the 15th International Conference on Information Fusion*, Singapore, July 2012.

J. B. Kuipers. *Quaternions and Rotation Sequences: a primer with applications to orbits, aerospace, and virtual reality*. Princeton University Press, 1999.

X. Li and Z. Li. A new calibration method for tri-axial field sensors in strap-down navigation systems. *Measurement Science and Technology*, 23(10), October 2012.

F. Lindsten and T. B. Schön. Backward simulation methods for Monte Carlo statistical inference. *Foundations and Trends in Machine Learning*, 6(1):1–143, 2013.

L. Ljung. *System Identification, Theory for the User*. Prentice Hall PTR, 2nd edition, 1999.

J. Löfberg. YALMIP: A toolbox for modeling and optimization in MATLAB. In *Proceedings of the IEEE International Symposium on Computer Aided Control Systems Design, 2004*, pages 284 – 289, Taipei, Taiwan, September 2004.

F. L. Markley. Attitude error representations for Kalman filtering. *Journal of guidance, control, and dynamics*, 26(2):311–317, 2003.

H. Nijmeijer and A. J. van der Schaft. *Nonlinear dynamical control systems*. Springer-Verlag, 1990.

J. Nocedal and S. J. Wright. *Numerical Optimization*. Springer Series in Operations Research, 2nd edition, 2006.

V. Renaudin, M. H. Afzal, and G. Lachapelle. Complete triaxis magnetometer calibration in the magnetic domain. *Journal of Sensors*, 2010.

S. Salehi, N. Mostofi, and G. Bleser. A practical in-field magnetometer calibration method for IMUs. In *Proceedings of the IROS Workshop on Cognitive Assistive Systems: Closing the Action-Perception Loop*, pages 39–44, Vila Moura, Portugal, October 2012.

T. B. Schön, A. Wills, and B. Ninness. System identification of nonlinear state-space models. *Automatica*, 47(1):39–49, 2011.

M. Segal and E. Weinstein. A new method for evaluating the log-likelihood gradient, the Hessian, and the Fisher information matrix for linear dynamic systems. *IEEE Transactions on Information Theory*, 35(3):682–687, 1989.

Trivisio Prototyping GmbH. `http://www.trivisio.com`, Accessed on March 20, 2014.

G. Troni and L. L. Whitcomb. Adaptive estimation of measurement bias in three-dimensional field sensors with angular-rate sensors: Theory and comparative experimental evaluation. In *Proceedings of Robotics: Science and Systems (RSS)*, Berlin, Germany, June 2013.

J. F. Vasconcelos, G. Elkaim, C. Silvestre, P. Oliveira, and B. Cardeira. Geometric approach to strapdown magnetometer calibration in sensor frame. *IEEE Transactions on Aerospace and Electronic Systems*, 47(2):1293–1306, April 2011.

E. Walter. *Identifiability of state space models*. Springer-Verlag, 1982.

Z. Wu, X. Hu, M. Wu, and J. Cao. Attitude-independent magnetometer calibration for marine magnetic surveys: regularization issue. *Journal of Geophysics and Engineering*, 10(4), June 2013a.

Z. Wu, X. Hu, M. Wu, and J. Cao. Constrained total least-squares calibration of three-axis magnetometer for vehicular applications. *Measurement Science and Technology*, 24(9), July 2013b.

Xsens Technologies B.V. `http://www.xsens.com`, Accessed on November 17, 2013.

Paper B

Indoor positioning using ultra-wideband and inertial measurements

Authors: Manon Kok, Jeroen D. Hol and Thomas B. Schön

Edited version of the paper:

M. Kok, J. D. Hol, and T. B. Schön. Indoor positioning using ultra-wideband and inertial measurements. *Preprint*, 2014b.

Indoor positioning using ultra-wideband and inertial measurements

Manon Kok[⋆], Jeroen D. Hol[†] and Thomas B. Schön[‡]

[⋆]Dept. of Electrical Engineering,
Linköping University,
SE–581 83 Linköping, Sweden
`manko@isy.liu.se`

[†]Xsens Technologies B.V.,
P.O. Box 559,
7500 AN Enschede, the Netherlands
`jeroen.hol@xsens.com`

[‡]Dept. of Information Technology
Uppsala University,
SE-751 05 Uppsala, Sweden
`thomas.schon@uu.se`

Abstract

In this work we present an approach to combine measurements from accelerometers and gyroscopes (inertial sensors) with time of arrival measurements from an ultra-wideband system for indoor positioning. Our algorithm uses a tightly-coupled sensor fusion approach and is shown to lead to accurate 6D pose (position and orientation) estimates as compared to data from an optical reference system. To be able to obtain position information from the ultra-wideband measurements, it is imperative that accurate estimates of the receivers' positions and clock offsets are known. Hence, we also present an easy-to-use algorithm to calibrate the ultra-wideband system. It is based on a maximum likelihood formulation and represents the ultra-wideband measurements assuming a heavy-tailed asymmetric noise distribution to account for measurement outliers. Using the heavy-tailed asymmetric noise distribution and the calibration results, it is shown that accurate position estimates can be obtained from the ultra-wideband measurements using a novel multilateration approach.

1 Introduction

In this work we present an indoor positioning approach using inertial sensors and time of arrival (TOA) measurements from an ultra-wideband (UWB) system. It uses a setup where a number of UWB receivers are placed in an indoor environment. A subject wearing inertial sensors and UWB transmitters walks through the environment, as shown in Figure 1. We aim at estimating the subject's 6D pose (position and orientation). To be able to obtain position information from

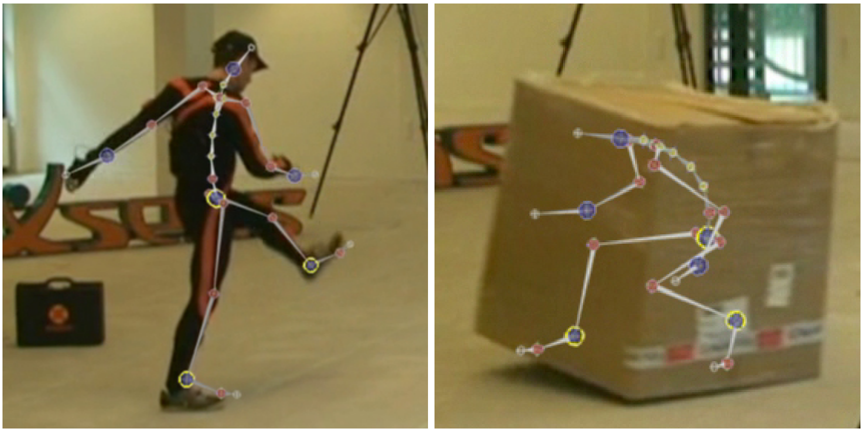

***Figure 1:** Example application showing a subject with* 17 *inertial sensors placed on the body and* 3 *UWB transmitters placed on the head and on the feet. As shown (right), the solution remains valid even in non-line-of-sight conditions.*

the UWB measurements, it is imperative that accurate estimates of the receivers' positions and clock offsets are known. To avoid the typically labor-intensive and time-consuming process of surveying the receivers' positions, we present an easy-to-use calibration method. Our previous solution presented in Hol et al. (2010) assumed "clean" measurements, i.e. it assumed that no outliers were present due to multipath and/or non-line-of-sight (NLOS) conditions. In this work, we instead model the UWB measurements assuming a heavy-tailed asymmetric noise distribution, thereby naturally handling outliers in the data. After calibration, the system can be used to estimate the subject's position. We present multilateration results using only the UWB measurements and sensor fusion results combining the UWB measurement with the inertial measurements. We will show that accurate results are obtained using both approaches, by comparing our results to an optical reference system.

Inertial sensors consist of accelerometers and gyroscopes measuring the sensor's acceleration and angular velocity. Their signals need to be integrated to obtain position and orientation estimates. These position and orientation estimates are accurate on a small time scale, but suffer from integration drift. Inertial sensors are well-suited for sensor fusion with positioning information, like for instance from a UWB setup. To the best of the author's knowledge there are only a few reports in the literature on how to combine UWB and inertial sensors. These include a hybrid 2D positioning tracking algorithm (Sczyslo et al., 2008) and an extended Kalman filter (EKF) for pedestrian tracking (Pittet et al., 2008). Both approaches are loosely coupled and only estimate a limited number of degrees of freedom. By a loosely coupled approach we refer to a solution where the measurements from one or several of the individual sensors are pre-processed before they are used to compute the final result. A tightly coupled approach on the other hand refers to an approach where all the measurements are used directly to compute the final result. This approach is for instance used in De Angelis et al. (2010); Hol et al. (2009).

UWB is a relatively new and promising radio technology with applications in radar, communication and localization. UWB technology typically makes use of impulse radio using very short pulses. These are typically in the order of 1 ns, resulting in a high spatial resolution. This characteristic makes UWB very suitable for localization purposes. It has successfully been applied in a wide variety of localization applications, such as industrial (Ubisense, 2014), healthcare (Time Domain, 2014; Gezici et al., 2005) and motion capture (Xsens Technologies B.V., 2013). UWB positioning accuracy is reported to be in the order of decimeters (Time Domain, 2014; Ubisense, 2014). Although UWB systems do not necessarily require line-of-sight visibility (Bellusci et al., 2011), the UWB measurements do suffer from multipath and NLOS conditions. Existing work typically assumes “clean” measurements without outliers.

In Section 2 we clearly formulate the problem and the sensors and their corresponding measurement models are then introduced in Section 3. In Section 4 we solve the multilateration problem using only UWB measurements. The UWB calibration problem is subsequently solved in Section 5. The solution to the sensor fusion problem, where we also make use of the inertial measurements can be found in Section 6. The experimental results and conclusion are then provided in Section 7 and Section 8, respectively.

2 Problem formulation

To be able to use the UWB measurements to estimate the transmitters’ positions, the receivers’ positions and clock offsets must be known. These are estimated in our calibration algorithm. Let us denote the model parameters estimated in the calibration algorithm as θ. The calibration algorithm computes a maximum likelihood (ML) estimate $\widehat{\theta}^{\mathrm{ML}}$. For a setup with $m = 1, \ldots, M$ receivers and $l = 1, \ldots, L$ transmitters, the UWB measurements are denoted $y_{\mathrm{u},mlk}$ for $k = 1, \ldots, K$ UWB pulses. We are interested in estimating the receivers’ *relative* positions and clock offsets. Hence, an arbitrary choice of a gravity-aligned UWB coordinate frame and the reference clock offset are used as constraints in the ML problem. The calibration algorithm therefore solves the problem as a constrained optimization problem

$$\begin{aligned} \widehat{\theta}^{\mathrm{ML}} = \operatorname*{arg\,max}_{\theta \in \Theta} \quad & \prod_{k=1}^{K} \prod_{l=1}^{L} \prod_{m=1}^{M} p_\theta(y_{\mathrm{u},mlk}), \\ \text{s.t.} \quad & A\theta = b. \end{aligned} \tag{1}$$

Since the UWB measurement function is nonlinear, the ML problem (1) is nonconvex and needs proper initialization. A two-step method for this will be used.

Using the obtained calibration, it is possible to use the UWB measurements to determine a transmitter's position via a multilateration approach. This approach regards each UWB pulse individually and solves the following optimization problem

$$\widehat{z}^{\mathrm{ML}} = \arg\max_{z} \prod_{m=1}^{M} p_z(y_{\mathrm{u},m}), \tag{2}$$

where z denotes the parameters estimated in the multilateration problem. Since the multilateration approach considers each pulse and each transmitter individually, the subscripts l and k of the UWB measurements have been omitted. The optimization problem (2) can be solved efficiently using a standard Gauss-Newton solver (Nocedal and Wright, 2006; Boyd and Vandenberghe, 2004).

It is also possible to use the UWB measurements together with inertial measurements in a sensor fusion approach. This approach aims at estimating the sensor's position and orientation (6D pose). Defining the state vector $x_{1:N}$ at times $t = 1, \dots, N$, the estimated state can be determined by solving a maximum a posteriori (MAP) problem,

$$\widehat{x}_{1:N}^{\mathrm{MAP}} = \arg\max_{x_{1:N}} \prod_{t=1}^{N} \prod_{l=1}^{L} \prod_{m=1}^{M} p(x_{1:N} \mid y_{\mathrm{u},mlt}, y_{\mathrm{a},t}, y_{\omega,t}). \tag{3}$$

Here, $y_{\mathrm{a},t}$ and $y_{\omega,t}$ denote the measurements from the inertial sensor. The time-evolution of the state is modeled using a dynamic model. To emphasize the time-dependency of the state, we have slightly changed our notation. The different pulses are denoted with a subscript t in (3) instead of with a subscript k as in (1).

3 Sensor models

The UWB and the inertial sensors are briefly introduced in this section, together with the models used in working with the measurements from these sensors. The UWB system is introduced in Section 3.1 and in Section 3.2 we describe how the measurements from the UWB system are modeled. Finally, the models used for the inertial sensors are described in Section 3.3.

3.1 The ultra-wideband system

A UWB system typically consists of a network of receivers which can track a large number of small, battery-powered inexpensive transmitters (Time Domain, 2014). UWB localization technologies can roughly be subdivided into three categories; 1. systems using time of arrival (TOA) measurements, 2. systems using angle of arrival measurements and 3. systems using signal strength measurements (Gezici et al., 2005; Sahinoglu et al., 2008). In this work we make use of TOA measurements. Hence, our UWB setup consists of a network of synchronized and stationary (rigidly fixed, mounted) receivers, all acquiring very precise TOA measurements of signals originating from a mobile transmitter. The setup is schematically depicted in Figure 2. The transmitter is also shown in Figure 3.

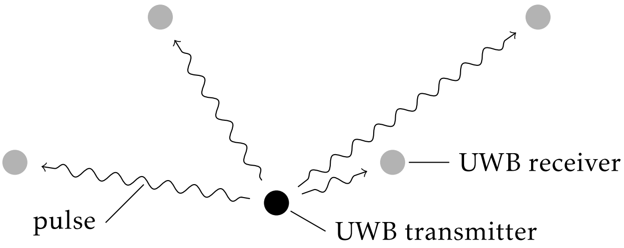

Figure 2: *The UWB setup consists of a number of stationary receivers making TOA measurements of signal pulses originating from a mobile transmitter.*

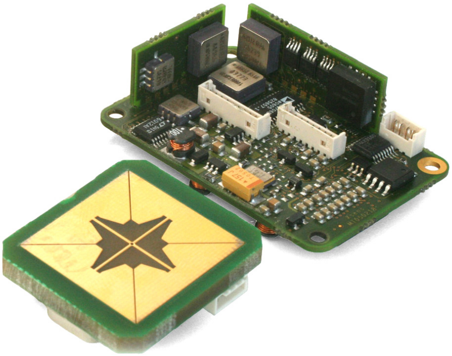

Figure 3: *Lower left: a UWB transmitter. The transmitter sends UWB pulses to the receivers as schematically depicted in Figure 2. Upper right: an IMU containing a 3-axis accelerometer and a 3-axis gyroscope.*

The transmitter's position is inferred from the time it takes for the UWB pulse to travel from the transmitter to a number of receivers. For this, it is important that the receivers' positions are known and that their clocks are synchronized. Although the receivers are synchronized to a central clock, they each have a small, constant clock offset due to for instance cable lengths. The receivers' positions and clock offsets are estimated in the calibration algorithm presented in Section 5.

The process of determining the transmitter position from TOA measurements is referred to as trilateration or, more accurately, *multilateration*. It is a well-studied topic and many algorithms have been reported in the literature, see e.g. Chan and Ho (1994); Gezici et al. (2005); Sayed et al. (2005); Sahinoglu et al. (2008). The low-cost transmitters in our setup have an inaccurate clock and can hence not provide accurate information concerning the time of transmission. A common multilateration technique is to eliminate the time of transmission by constructing time difference of arrival (TDOA) measurements from pairs of TOA measurements. The resulting set of hyperbolic equations can then be solved for position.

The drawback of this approach is that the constructed TDOA measurements are no longer independently distributed which complicates the calculations. In this work we use a well-known equivalent approach, treating the time of transmission as an unknown in the optimization problem (2).

Ideally, the signal travels directly from the transmitter to the different receivers. In that case, the TOA measurements are directly related to the distance traveled. In case the signal encounters a medium which delays or reflects the signal, the time of flight is prolonged and the pulse will be delayed. The majority of multilateration algorithms assume “clean” measurements without delays. The presence of non-zero delays severely affects the accuracy of the estimated position, giving rise to several ad hoc methods to detect which measurements are corrupted. Typically, multilateration is performed for a number of subsets of the measurements and the “best” solution is returned. In this work, however, we will explicitly model the possibility of delays using a heavy-tailed asymmetric distribution in the UWB measurement model.

3.2 Modeling the ultra-wideband measurements

The UWB setup consists of M receivers and N transmitters. The TOA measurements $y_{\mathrm{u},mlk}$ are modeled as

$$y_{\mathrm{u},mlk} = \tau_{lk} + \|r_m^{\mathrm{n}} - t_{lk}^{\mathrm{n}}\|_2 + \Delta\tau_m + e_{\mathrm{u},mlk}, \tag{4}$$

where τ_{lk} is the time of transmission of pulse k from transmitter l, t_{lk}^{n} is the position of transmitter l at the time of transmitting the k^{th} pulse, r_m^{n} is the position of the m^{th} receiver and $\Delta\tau_m$ is the clock-offset of the m^{th} receiver. The superscript n denotes the navigation frame. It is a local coordinate frame that is aligned with the earth's gravity and with the axes of the frame defined during the UWB calibration, as discussed in Section 2. Note that without loss of generality we assume all quantities to be expressed in meters.

Due to NLOS conditions and/or multipath we expect a model with $e_{\mathrm{u},mlk}$ i.i.d. Gaussian noise to be violated. More specifically, we expect a small number of measurements to be delayed. In Hol (2011) this was modeled by including a possibly non-zero delay in the measurement function (4). In a novel multilateration approach, the delays were assumed to be exponentially distributed. This was shown to lead to accurate position estimates, but it introduced M additional model parameters for each pulse k. In this work we will instead model the noise using the following asymmetric distribution

$$e_{\mathrm{u},mlk} \sim \begin{cases} \mathrm{Cauchy}(0,\gamma) & e_{\mathrm{u},mlk} \leq 0, \\ \mathcal{N}(0,\sigma^2) & e_{\mathrm{u},mlk} > 0. \end{cases} \tag{5}$$

As depicted in Figure 4, the Cauchy distribution (shown in blue) has heavy tails and therefore naturally allows for the presence of outliers. Since NLOS and multipath conditions only introduce time *delays*, we expect only outliers in one direction. Hence, we use the asymmetric probability density function (pdf) (5) depicted in red in Figure 4. This noise model will be used both for the calibration

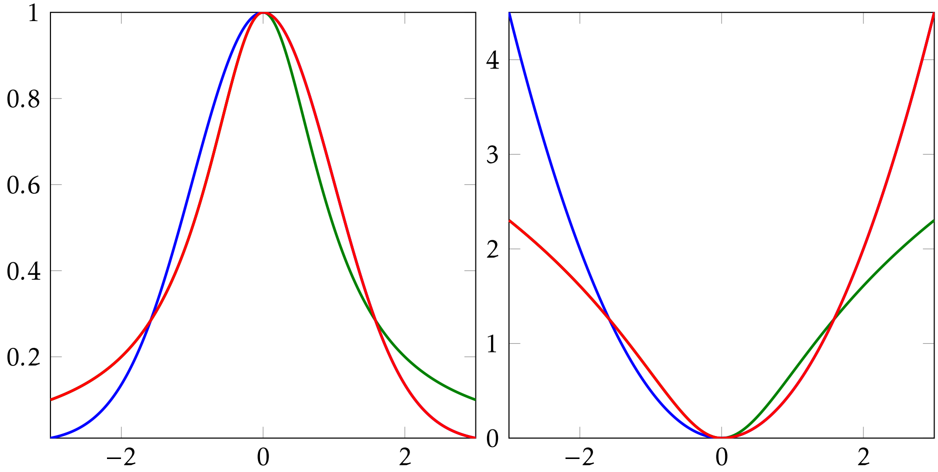

Figure 4: *Left: probability density function of an unnormalized* $\mathcal{N}(0,1)$ *distribution (blue), an unnormalized Cauchy*$(0,1)$ *distribution (green) and the asymmetric distribution* (5) *assuming* $\sigma = \gamma = 1$ *(red). Right: log likelihood cost function of the pdf* $\mathcal{N}(0,1)$ *(blue), of the pdf Cauchy*$(0,1)$ *(green) and the asymmetric cost function* (9) *assuming* $\sigma = \gamma = 1$ *(red).*

algorithm in Section 5 and the multilateration approach presented in Section 4. From the experimental results in Section 7.2 it will be shown that making use of the fact that the noise distribution is in fact asymmetric is specifically helpful in the presence of a large number of outliers.

3.3 Modeling the inertial measurements

An inertial measurement unit (IMU) containing a 3-axis accelerometer and a 3-axis gyroscope is shown in Figure 3. The inertial measurements are resolved in the body frame b. Its origin lies in the center of the accelerometer triad and its axes are aligned with the casing. The gyroscope measures the sensor's angular velocity ω_t. Its measurements $y_{\omega,t}$ are modeled as

$$y_{\omega,t} = \omega_t + \delta_{\omega,t} + e_{\omega,t}, \tag{6}$$

where $\delta_{\omega,t}$ denotes the gyroscope bias and $e_{\omega,t} \sim \mathcal{N}(0, \sigma_\omega^2)$. The accelerometer measures the external specific force f_t^{b} exerted on the sensor. It consists of the sensor's linear acceleration a_t^{n} and the gravity vector g^{n}, both resolved in the navigation frame n. The accelerometer measurements $y_{\mathrm{a},t}$ are modeled as

$$y_{\mathrm{a},t} = f_t^{\mathrm{b}} + \delta_{\mathrm{a},t} + e_{\mathrm{a},t} = R_t^{\mathrm{bn}} \left(a_t^{\mathrm{n}} - g^{\mathrm{n}}\right) + \delta_{\mathrm{a},t} + e_{\mathrm{a},t}, \tag{7}$$

where $\delta_{\mathrm{a},t}$ denotes the accelerometer bias and $e_{\mathrm{a},t} \sim \mathcal{N}(0, \sigma_\mathrm{a}^2)$. The rotation matrix R_t^{bn} represents the rotation from the navigation frame n to the body frame b.

4 Multilateration

As described in Section 3.1, the transmitter's position can be determined from TOA measurements. We formulate the multilateration problem as an ML problem (see (2)). Using the noise model (5), the fact that the logarithm is a monotonic function and neglecting constant terms, the resulting optimization problem is given by

$$\min_{t^{\mathrm{n}},\tau} \sum_{m=1}^{M} V_m, \tag{8}$$

where

$$V_m = \begin{cases} \log\left(1 + \left(\frac{e_{\mathrm{u},m}}{\gamma}\right)^2\right) & e_{\mathrm{u},m} \leq 0, \\ \frac{1}{2}\left(\frac{e_{\mathrm{u},m}}{\sigma}\right)^2 & e_{\mathrm{u},m} > 0. \end{cases} \tag{9}$$

Here, the noise $e_{\mathrm{u},m}$ is given by (4) and (5). Since multilateration only computes an estimate of the position of one transmitter based on data from one pulse, the subscripts k and l are omitted. The cost function (9) is depicted in Figure 4 and allows for negative outliers due to multipath and NLOS conditions. The multilateration problem can be solved when TOA measurements from at least 4 receivers are available. In case enough measurements are available, the initial condition of the optimization problem (8) is irrelevant.

5 Calibration

In the previous section, we assumed that the receivers' positions and their clock offsets were known. In this section, we will derive a calibration algorithm to determine the receivers' positions $\{r_m^{\mathrm{n}}\}_{m=1}^M$ and their clock offsets $\{\Delta\tau_m\}_{m=1}^M$ using the ML formulation stated in (1). This is done by moving a single transmitter through the measurement volume. The data collected in this way is denoted $\mathcal{D}_1$. The position of the transmitter $\{t_k^{\mathrm{n}}\}_{k=1}^K$ and the times of transmission of the pulses $\{\tau_k\}_{k=1}^K$ are assumed to be unknown. Hence, the parameter vector is

$$\theta = \left(\{t_k^{\mathrm{n}}, \tau_k\}_{k=1}^K, \{r_m^{\mathrm{n}}, \Delta\tau_m\}_{m=1}^M\right). \tag{10}$$

Note that compared to the UWB measurement model (4), we have omitted the subscript l since we assume the case of only a single transmitter. The calibration problem is non-convex and hence needs proper initialization. In Section 5.1, we introduce a two-step procedure to compute an initial estimate. In Section 5.2 we will then introduce the resulting calibration algorithm.

5.1 Computing an initial estimate

As a first step of the initial estimation, a second data set, denoted $\mathcal{D}_2$, is used to determine the receivers' positions and their clock offsets. This data set is collected using a number of transmitters attached to the receivers. Hence, the relative position of each transmitter with respect to the corresponding receiver is known and constant. It can be approximated to be $\delta^{\mathrm{n}}_{\mathrm{rt}}$. Since it is not necessary to walk through the measurement volume during the collection of this data set, the measurements in the data set $\mathcal{D}_2$ can typically be assumed to be outlier-free. Hence, $e_{\mathrm{u},mlk}$ in (4) can accurately be modeled using a Gaussian pdf. Assuming that the standard deviation of Gaussian is the same for all m, l and k, this leads to the following constrained least-squares problem

$$\begin{aligned}
\widehat{\theta}_1 = \arg\min_{\theta_1} \quad & \frac{1}{2}\sum_{m=1}^{M}\sum_{l=1}^{L}\sum_{k=1}^{K} e^2_{\mathrm{u},mlk}, && (11a)\\
\text{s.t.} \quad & A_m r^{\mathrm{n}}_m = 0, \qquad m = 1,2, && (11b)\\
& A_{\mathrm{h}} r^{\mathrm{n}}_{m,3} = h_m, \quad m = 1,\dots,M, && (11c)\\
& \Delta\tau_1 = 0, && (11d)\\
& r^{\mathrm{n}}_m - t^{\mathrm{n}}_m = \delta^{\mathrm{n}}_{\mathrm{rt}}, \quad m = 1,\dots,M, && (11e)
\end{aligned}$$

where

$$\theta_1 = \left(\{r^{\mathrm{n}}_m, \Delta\tau_m\}_{m=1}^{M}, \{t^{\mathrm{n}}_{l,\mathcal{D}_2}, \{\tau^{\mathrm{n}}_{lk,\mathcal{D}_2}\}_{k=1}^{K}\}_{l=1}^{L}\right). \tag{12}$$

Note that the subscript $\mathcal{D}_2$ on the (stationary) transmitter positions t^{n}_l and the times of transmission τ^{n}_{lk} is added to stress that these parameters are only relevant to the data $\mathcal{D}_2$. The constraint (11e) is used to incorporate the knowledge of the location of the transmitters with respect to the receivers. Note that we assume that each receiver has a transmitter attached to it, i.e. we have M constraints (11e). The constraint (11d) is used to define the reference clock offset as discussed in Section 2. The constraints (11b) and (11c) are used to define the UWB coordinate frame where the two receivers in (11b) define its origin and x-axis. Hence, the matrices A_m are given by

$$A_1 = \begin{pmatrix} e_1 & e_2 & e_3 \end{pmatrix}^{\mathsf{T}}, \quad A_2 = \begin{pmatrix} e_2 & e_3 \end{pmatrix}^{\mathsf{T}}, \tag{13}$$

where $\{e_i\}_{i=1}^{3}$ is the standard basis for $\mathbb{R}^3$. The horizontal plane and thereby the z-axis are defined by the constraint (11c) with

$$A_h = e_3^{\mathsf{T}}, \tag{14}$$

which sets the estimated receiver heights (denoted $r_{\mathrm{m},3}$) equal to the measured heights h_m. Note that it is not necessary for the calibration algorithm that all receiver heights are known. In Hol (2011); Hol et al. (2010) the optimization problem was therefore formulated with only a constraint on one of the receivers' heights. However, using the surveyed heights of all receiver's makes sure that the UWB coordinate system is gravity-aligned. This will be beneficial for our sensor fusion approach in Section 6.

The problem (11) is again a non-convex optimization problem and therefore requires a starting point. However, when started in an arbitrary disjoint receiver configuration, i.e. $r_i \neq r_j$, it converges to the correct configuration or a (partially) mirrored version. To prevent the latter from happening, we start the optimization (11) in a user-specified initial receiver configuration: a noisy, rotated and scaled estimate of the set of receiver positions. Note that the receiver positions and clock offsets estimated in (11) are biased since the constraints (11e) only hold approximately. However, they provide a viable starting point for the final calibration problem.

As a second step of the initialization, an initial estimate of the transmitter positions and the times of transmission are determined for the data set $\mathcal{D}_1$ in which a transmitter is moved around the volume. The parameters

$$\theta_2 = \left(\{t_k^{\mathrm{n}}, \tau_k\}_{k=1}^{K}\right) \tag{15}$$

are obtained by solving K multilateration problems, as discussed in Section 4.

We have hence obtained initial estimates of the receiver positions and clock offsets from (11), (12) and initial estimates of the transmitter positions and times of transmission from (15). These can be used as a starting point for the resulting calibration algorithm.

5.2 Resulting calibration algorithm

The resulting calibration algorithm uses the data set $\mathcal{D}_1$ in which a transmitter is moved around the measurement volume. To obtain an ML estimate of the parameter vector (10), the following constrained optimization problem is solved

$$\begin{aligned} \widehat{\theta}^{\mathrm{ML}} = \arg\min_{\theta} \quad & \sum_{k=1}^{K}\sum_{m=1}^{M} V_{mk}, && \text{(16a)}\\ \text{s.t.} \quad & A_m r_m^{\mathrm{n}} = 0, \qquad m = 1, 2, && \text{(16b)}\\ & A_h r_{m,3}^{\mathrm{n}} = h_m, \quad m = 1, \dots, M, && \text{(16c)}\\ & \Delta\tau_1 = 0, && \text{(16d)} \end{aligned}$$

where

$$V_{mk} = \begin{cases} \log\left(1 + \left(\frac{e_{\mathrm{u},mk}}{\gamma}\right)^2\right) & e_{\mathrm{u},mk} \leq 0,\\ \frac{1}{2}\left(\frac{e_{\mathrm{u},mk}}{\sigma}\right)^2 & e_{\mathrm{u},mk} > 0. \end{cases} \tag{17}$$

The optimization problem (16) looks very similar to the one used to obtain an initial estimate (11). However, in (16) we use data from $\mathcal{D}_1$, i.e. we do not assume any knowledge about the position of the transmitter. Also, since it is necessary to walk around with the transmitter, we assume that outliers can occur in the data and model this using the asymmetric noise distribution in (5). The resulting calibration algorithm is summarized in Algorithm 1.

6 Sensor fusion

In this section we describe our approach to combine UWB measurements with inertial measurements to estimate a subject's 6D pose. It is based on tightly coupled

Algorithm 1 Ultra-wideband calibration

```
1. Construct a setup consisting of $M$ stationary receivers.
2. Place $M$ transmitters in close proximity to the receiver antennas and collect a data set $\mathcal{D}_2$.
3. Solve (11) using the data $\mathcal{D}_2$ to obtain $\{r_{m,0}, \Delta\tau_{m,0}\}_{m=1}^{M}$. The optimization is initialized using a noisy, scaled and rotated estimate of the set of receiver positions $\{r_m\}_{m=1}^{M}$ provided by the user.
4. Collect a dataset $\mathcal{D}_2$ while moving a single transmitter through the measurement volume.
5. Apply multilateration (8) on $\mathcal{D}_2$ using the calibration values of Step 3 to obtain $\{t^{\mathrm{n}}_{k,0}, \tau_{k,0}\}_{k=1}^{K}$.
6. Solve (16) for $\mathcal{D}_2$. The optimization is started in
       $\theta_0 = \left(\{t_{k,0}, \tau_{k,0}\}_{k=1}^{K}, \{r_{m,0}, \Delta\tau_{m,0}\}_{m=1}^{M}\right),$
   using the results from Steps 3 and 5.
```

sensor fusion of the UWB and the inertial sensors.

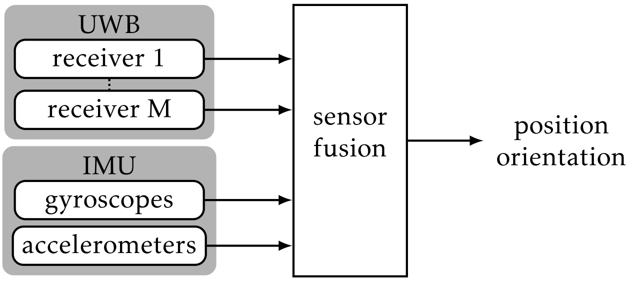

Figure 5: *Tightly coupled sensor fusion. The "raw" measurements from the UWB receivers and the IMU are directly used for sensor fusion.*

The tightly coupled sensor fusion approach uses the measurements directly to estimate the subject's pose, as schematically depicted in Figure 5. As can be seen, the UWB measurements are not preprocessed using for instance a multilateration approach. An advantage of a tightly coupled approach is that pre-processing of measurements typically results in a loss of information. This is mainly due to approximations of statistical distributions, but in extreme cases measurements are ignored, for instance when there are not enough TOA measurements for multilateration. By directly using the sensor measurements, maximal advantage is taken of the available information.

The state estimation problem is formulated as a MAP problem (3). We solve the MAP problem using an extended Kalman filter (EKF). The EKF handles the different sample rates and a varying number of measurements straightforwardly. It runs at the high data rate of the IMU and the UWB updates are only performed when measurements are available. Our EKF implementation does not model the UWB noise using the heavy-tailed asymmetric distribution (5). Instead, it uses a Gaussian noise assumption. Outliers from NLOS conditions and/or multipath violate the assumption that $e_{\mathrm{u},mk} \sim \mathcal{N}(0, \sigma^2)$. They can be detected using hypothesis testing on the residuals/innovations of the EKF. Tightly coupled sensor fusion can disregard the affected measurements while still utilizing the remaining ones and hence is well-suited for outlier rejection.

In the remainder of this section we will introduce the process and measurement models used in the EKF implementation. Starting with the process model, we can model the position, the velocity and the orientation of the IMU in terms of the sensor's acceleration and angular velocity. Hence, the inertial measurements are used as an input to the process model

$$\begin{aligned} p^{\mathrm{n}}_{t+1} &= p^{\mathrm{n}}_t + T v^{\mathrm{n}}_t + \tfrac{T^2}{2} a^{\mathrm{n}}_t, & \text{(18a)} \\ v^{\mathrm{n}}_{t+1} &= v^{\mathrm{n}}_t + T a^{\mathrm{n}}_t, & \text{(18b)} \\ q^{\mathrm{nb}}_{t+1} &= q^{\mathrm{nb}}_t \odot \exp(\tfrac{T}{2} \omega_t). & \text{(18c)} \end{aligned}$$

The sensor's position p^{n}_t and its velocity v^{n}_t are expressed in the navigation frame n. The acceleration a^{n}_t is estimated from (7) and T denotes the sampling interval. The orientation q^{nb}_t is expressed using a unit quaternion and is modeled in terms of the angular velocity ω_t estimated from (6). In (18c), $\odot$ denotes the quaternion product and exp denotes the vector exponential (Hol, 2011). The process of estimating position and orientation from the inertial measurements as in (18) is schematically depicted in Figure 6 (see also (6) and (7)). Note that in the remainder we will interchangeably make use of the unit quaternion q^{nb} and the rotation matrix R^{nb} as representations of the orientation. Also, we will use the notation $R^{\mathrm{bn}} = (R^{\mathrm{bn}})^{\mathsf{T}}$ for the inverse rotation.

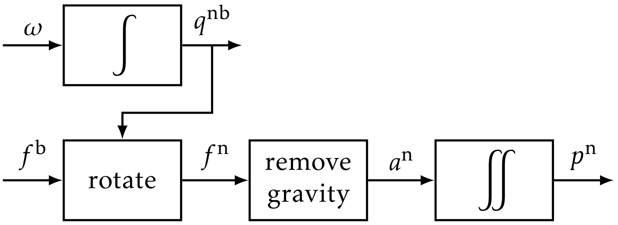

Figure 6: *Schematic depicting the process of determining position and orientation from inertial measurements, assuming a known initial position and orientation.*

The inertial bias terms δ_ω and δ_{a} from (6) and (7) are slowly time-varying. Hence, they are modeled as random walks,

$$\begin{aligned} \delta_{\omega,t+1} &= \delta_{\omega,t} + e_{\delta_\omega,t}, & \text{(19a)} \\ \delta_{\mathrm{a},t+1} &= \delta_{\mathrm{a},t} + e_{\delta_{\mathrm{a}},t}, & \text{(19b)} \end{aligned}$$

where $e_{\delta_{\mathrm{a}},t}$ and $e_{\delta_\omega,t}$ are i.i.d. Gaussian noises.

In the calibration algorithm we regard all UWB pulses as independent. In the pose estimation, however, we take into account the time-dependency. Modeling this, it can be assumed that the transmitter sends in regular intervals $\delta\tau$. In practice, these time intervals $\delta\tau$ will vary slightly over time due to clock drift and clock jitter. Hence, the time of transmission τ is modeled as an integrated random walk

$$\tau_{t+1} = \tau_t + \delta\tau_t + e_{\tau,t}, \tag{20a}$$

$$\delta\tau_{t+1} = \delta\tau_t + e_{\delta\tau,t}, \tag{20b}$$

where $e_{\tau,t}$ and $e_{\delta\tau,t}$ are i.i.d. Gaussian noise.

In the EKF measurement update, the UWB measurements, modeled as in (4), are used to update the state. For this, the IMU and the UWB transmitter are assumed to be rigidly attached to each other. The distance between both is assumed to be known and it is denoted t^{b}. The transmitter position t_t^{n} in (4) and the IMU pose $q_t^{\mathrm{nb}}, p_t^{\mathrm{n}}$ in (18) are therefore related by

$$t_t^{\mathrm{n}} = p_t^{\mathrm{n}} + R_t^{\mathrm{nb}} t^{\mathrm{b}}. \tag{21}$$

Combining (18)-(20), the resulting state vector estimated in the EKF is given by

$$x_t = \left((p_t^{\mathrm{n}})^{\mathsf{T}}, (v_t^{\mathrm{n}})^{\mathsf{T}}, (q_t^{\mathrm{nb}})^{\mathsf{T}}, (\delta_{\mathrm{a},t})^{\mathsf{T}}, (\delta_{\omega,t})^{\mathsf{T}}, \tau_t, \delta\tau_t \right)^{\mathsf{T}}. \tag{22}$$

Note that we encode the orientation state using a three-dimensional state vector around a linearization point represented by a unit quaternion (Crassidis et al., 2007; Grisetti et al., 2010; Hol, 2011). We assume the measurement covariances relevant to the EKF to be known. They can be chosen from data sheets, from Allan variance analysis (El-Sheimy et al., 2008) or based on prior sensor information. Our pose estimation approach is summarized in Algorithm 2.

Algorithm 2 Pose estimation

1. Initialize the state vector.
2. Perform a time update using the process model (18)-(20) with the inertial measurements as input signals.
3. If new UWB measurements are available, do a measurement update with outlier detection. Use the measurements in combination with the measurement model (4) and (21).
4. Set $t := t + 1$ and iterate from Step 2.

7 Experimental results

In our experiments, we use a UWB setup consisting of 10 receivers deployed in a room with a size of approximately 8 × 6 × 2.5 m. In Section 7.1 we will first present our calibration results. Subsequently, we will discuss experimental results from an approximately 35 s experiment, where a subject is walking along a circular path. IMUs and UWB transmitters have been attached to his feet and to his head. The UWB measurements from the transmitter on the foot are significantly more affected by NLOS conditions and multipath since the transmitter is quite close to the ground. Furthermore, the body often blocks the direct path to the receivers. In Section 7.2 we will discuss our multilateration results using a transmitter on the foot. We will show the benefits of using an asymmetric heavy-tailed distribution (5) over a symmetric Cauchy distribution. In Section 7.3 we will discuss our pose estimation results from combining the inertial and UWB measurements of the sensors on the subject's head.

7.1 Calibration

Algorithm 1 has been used to estimate the receivers' positions and clock offsets in the UWB setup. The estimated trajectory of the transmitter and the ML estimates of the receivers' positions are depicted in Figure 8. The smoothness of the transmitter's trajectory suggests that good multilateration results are obtained and hence gives confidence in the resulting calibration results. This confidence is strengthened by Figure 7 in which the residuals of the calibration algorithm are depicted for all 10 receivers. As can be seen, the residuals look fairly Gaussian around 0 apart from a number of outliers in the negative direction, consistent with our modeled noise assumption (9).

The parameters γ and σ in (17) are considered to be tuning parameters. The parameter γ in (16) is the scale parameter of the Cauchy distribution. Its choice influences the width of the distribution. The parameter σ^2 in the Gaussian distribution represents its covariance. A too large choice of σ^2 and/or a too small choice of γ would reduce the effect of the asymmetric distribution. A too small σ^2 on the other hand makes it difficult for the algorithm to find a good estimate. A too large choice of γ would give the algorithm too much freedom. We do not estimate the parameters γ and σ. Instead, we use a more pragmatic approach and choose values for γ and σ which work well on our data. For the results presented in Figures 7 and 8, we have used $\gamma = 1$ and $\sigma^2 = 0.1$.

7.2 Multilateration

To provide challenging data for the multilateration algorithm discussed in Section 4, in this section we present multilateration results using measurements from the transmitter on the foot. Note that the results have been obtained using a UWB system that has been calibrated with a previous version of our calibration algorithm, presented in Hol et al. (2010).

For each UWB pulse we solve a multilateration problem (8). Two different noise distributions have been tested. The first is the asymmetric heavy-tailed distribution (9) of which the parameters σ and γ are chosen as in Section 7.1. The second is a symmetric Cauchy distribution with $\gamma = 1$. The position estimates using both noise distributions are presented in Figure 9. Reference data from an optical positioning system is also depicted. On this fairly difficult data set, the asymmetric distribution (9) clearly leads to more accurate position estimates. Wrong position estimates from the multilateration algorithm using Cauchy noise distribution can be attributed to the fact that it allows for fairly large positive

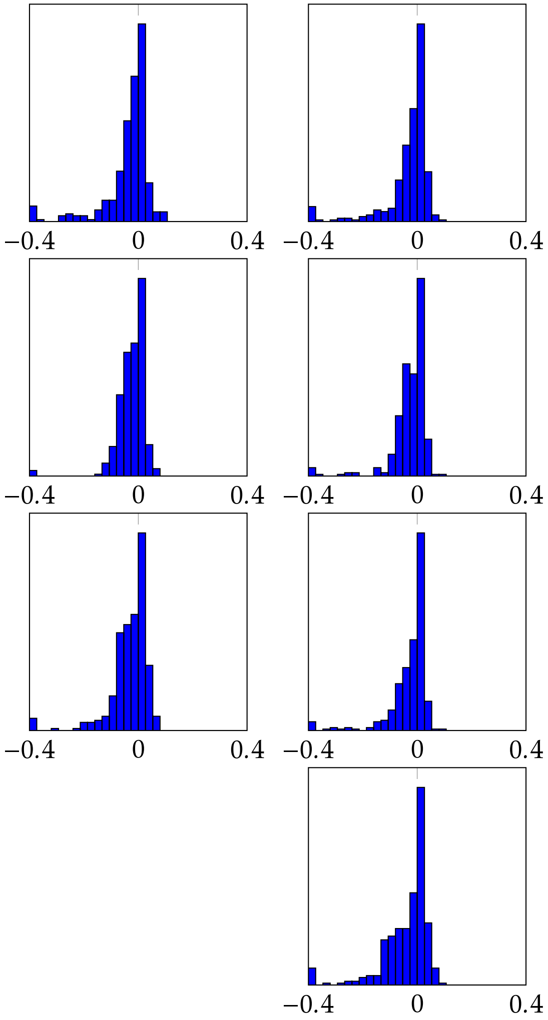

Figure 7: *Residuals from the calibration algorithm for the 10 receivers. Note that the residuals outside of the scope of the figures have been collected in the outermost bins.*

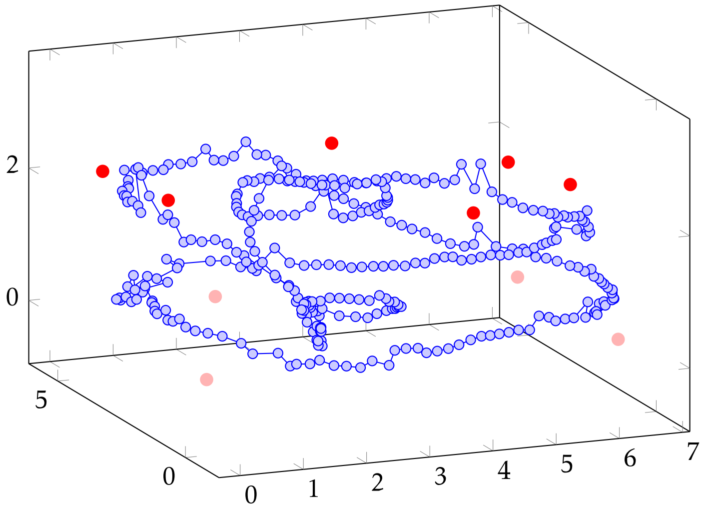

Figure 8: Calibration results of the UWB setup. The estimated transmitter positions are depicted in blue. The receivers in our UWB setup are either placed close to the ground or close to the ceiling. The positions of the receivers close to the ceiling are depicted in bright red. The positions of the receivers close to the ground are depicted in light red.

residuals as shown in Figure 10. Note that on "cleaner" UWB data, both distributions perform equally well.

7.3 Pose estimation

To evaluate the proposed pose estimation algorithm it has been used to track the motion of a test-subject walking in an indoor environment. The same experiment has been used as for the multilateration discussed in Section 7.2. However, in Algorithm 2 we have instead used the IMU and the transmitter on the head of the subject. The UWB measurements hence suffer less from multipath and NLOS conditions. The IMU provides 120 Hz inertial measurements. The UWB pulses are transmitted at 10 Hz.

Figure 11 shows an overview of the estimated trajectory and the UWB receivers' positions. The circular path is clearly recognizable. It only occupies a small part of the measurement volume of the UWB tracking system so that a performance comparison with an optical reference system is possible.

Figures 12 and 13 show the estimated position and orientation of the IMU as compared to those from an optical reference system. It can be concluded that the system provides drift-free and accurate estimates for all quantities at a high output frequency. In fact, the comparison shows 5 cm RMSE for position and 1° RMSE for orientation, see Table 1.

The above discussion shows that the proposed sensor fusion algorithm performs

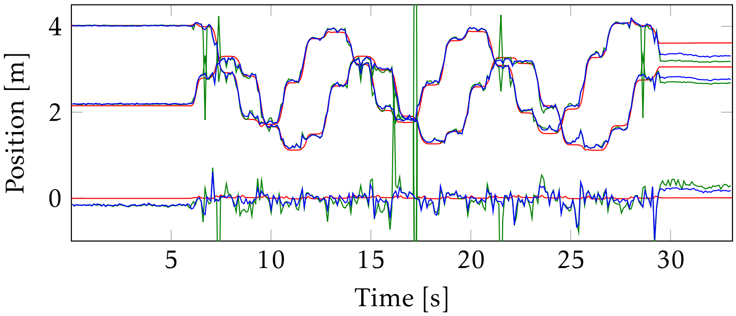

Figure 9: *Position estimates from the multilateration approach using the transmitter on the foot. The estimated positions using the asymmetric heavy-tailed noise distribution* (9) *are depicted in blue. The estimated positions using a Cauchy noise distribution are depicted in green. Data from an optical reference system is shown in red.*

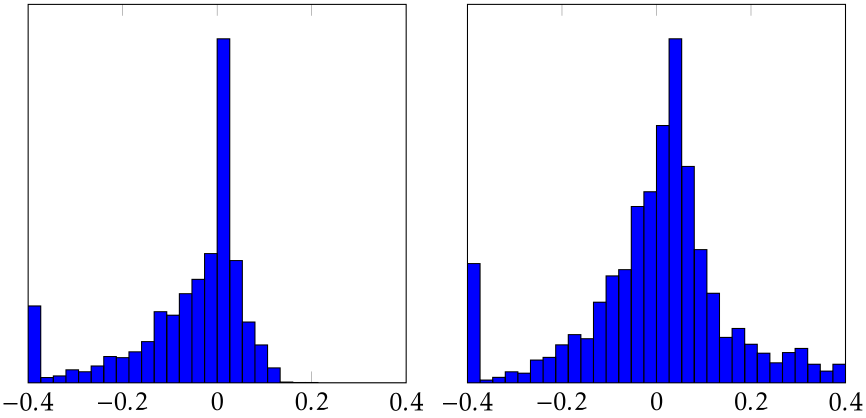

Figure 10: *Residuals from the multilateration approach using (left) the asymmetric distribution* (9) *and (right) a symmetric Cauchy distribution.*

Table 1: *RMSE for the position and orientation estimates from Algorithm 2 as compared to data from an optical reference system.*

		x	y	z
position	m	0.05	0.04	0.03
orientation	°	0.65	0.46	0.85

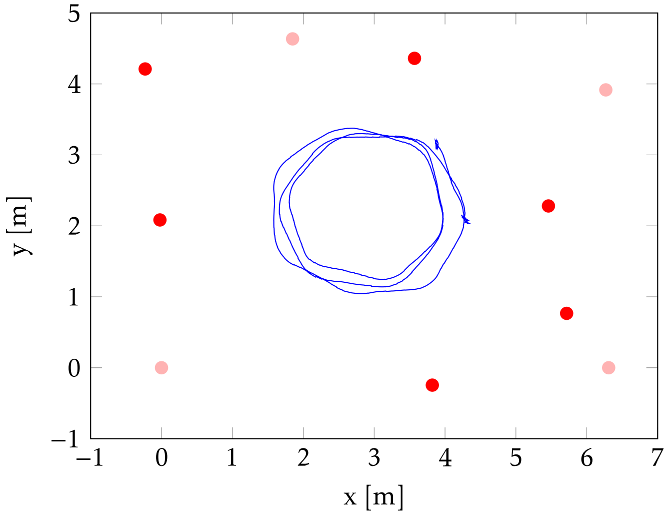

Figure 11: *Top view of the experiment where the subject walked a circular trajectory. Shown is the estimated trajectory $p^n_{1:N}$ of the IMU on the subject's head (blue). The positions of the receivers close to the ceiling are depicted in bright red. The positions of the receivers close to the floor are depicted in light red.*

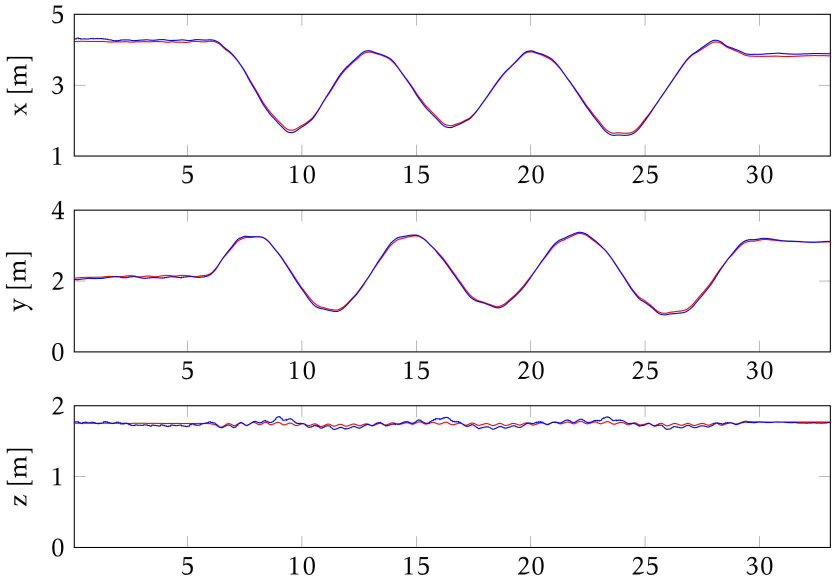

Figure 12: *Position of the IMU $p^n_{1:N}$. The estimates from Algorithm 2 are depicted in blue. The estimates from an optical reference system are depicted in red.*

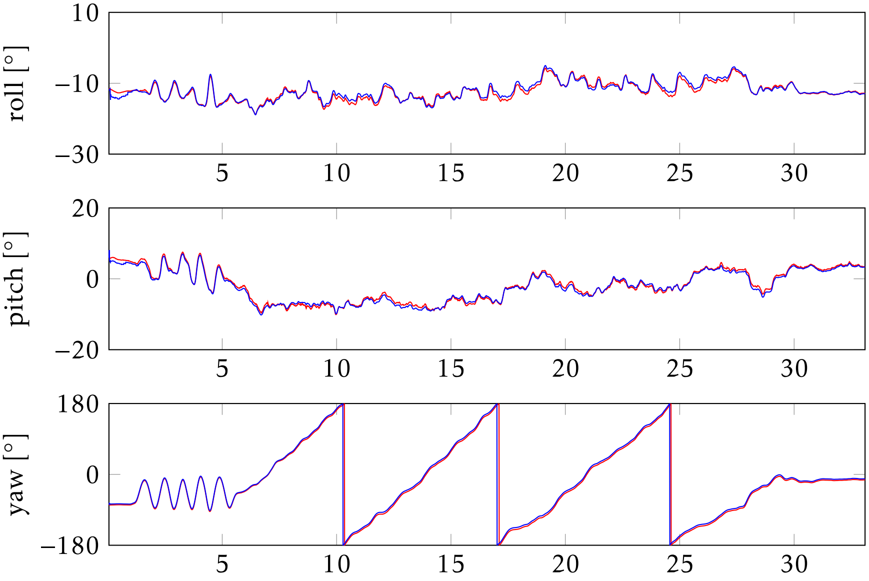

Figure 13: *Orientation of the IMU* $q^{nb}_{1:N}$ *expressed in Euler angles (roll, pitch, yaw). The estimates from Algorithm 2 are depicted in blue. The estimates from an optical reference system are depicted in red.*

very well on a realistic indoor tracking scenario. This performance can not exclusively be attributed to effective sensor fusion; accurate calibration of the UWB system is equally important.

8 Conclusions and future work

We have presented a sensor fusion approach to combine inertial measurements with TOA measurements from a UWB system for 6D pose estimation. The approach is shown to lead to accurate position and orientation estimates when compared to data from an optical reference system. The accuracy of this approach heavily depends on the quality of the calibration of the UWB system, i.e. on the accuracy of the estimates of the receivers' positions and clock offsets. We have solved the UWB calibration problem using a novel approach, assuming an asymmetric heavy-tailed distribution to model the outliers in the UWB measurements. Using the same distribution, we have also shown that accurate position estimates can be obtained using a multilateration approach, even from challenging data containing a fairly large amount of outliers.

Interesting future work involves extending the sensor fusion approach discussed in Section 6 by making use of an optimization-based approach in a similar way as presented in Kok et al. (2014a) instead of the EKF. Using that approach, the asymmetric heavy-tailed distribution can straightforwardly be taken into account.

Acknowledgements

This work is supported by CADICS, a Linnaeus Center funded by the Swedish Research Council (VR) and by BALANCE, a European Commission, FP7 research project.

Bibliography

G. Bellusci, D. Roetenberg, F. Dijkstra, H. J. Luinge, and P. Slycke. Xsens MVN MotionGrid: Drift-free human motion tracking using tightly coupled ultra-wideband and miniature inertial sensors, June 2011.

S. Boyd and L. Vandenberghe. *Convex Optimization*. Cambridge University Press, 2004.

Y. T. Chan and K. C. Ho. A simple and efficient estimator for hyperbolic location. *IEEE Transactions on Signal Processing*, 42(8):1905–1915, 1994.

J. L. Crassidis, F. L. Markley, and Y. Cheng. A survey of nonlinear attitude estimation methods. *Journal of Guidance, Control, and Dynamics*, 30(1):12–28, 2007.

A. De Angelis, J.O. Nilsson, I. Skog, P. Händel, and P. Carbone. Indoor positioning by ultrawide band radio aided inertial navigation. *Metrology and Measurement Systems*, 17(3):447–460, 2010.

N. El-Sheimy, H. Hou, and X. Niu. Analysis and modeling of inertial sensors using Allan variance. *IEEE Transactions on Instrumentation and Measurement*, 57(1):140–149, 2008.

S. Gezici, Z. Tian, G. B. Giannakis, H. Kobayashi, A. F Molisch, H. V. Poor, and Z. Sahinoglu. Localization via ultra-wideband radios: a look at positioning aspects for future sensor networks. *IEEE Signal Processing Magazine*, 22(4): 70–84, 2005.

G. Grisetti, R. Kummerle, C. Stachniss, U. Frese, and C. Hertzberg. Hierarchical optimization on manifolds for online 2D and 3D mapping. In *Proceedings of the IEEE International Conference on Robotics and Automation (ICRA)*, pages 273–278, Anchorage, Alaska, 2010.

J. D. Hol. *Sensor Fusion and Calibration of Inertial Sensors, Vision, Ultra-Wideband and GPS*. PhD thesis, Linköping University, Sweden, June 2011.

J. D. Hol, F. Dijkstra, H. Luinge, and T. B. Schön. Tightly coupled UWB/IMU pose estimation. In *Proceedings of the IEEE International Conference on Ultra-Wideband (ICUWB)*, pages 688–692, Vancouver, Canada, September 2009.

J. D. Hol, T. B. Schön, and F. Gustafsson. Ultra-wideband calibration for indoor positioning. In *Proceedings of the IEEE International Conference on Ultra-Wideband (ICUWB)*, pages 1–4, Nanjing, China, September 2010.

M. Kok, J. D. Hol, and T. B. Schön. An optimization-based approach to human body motion capture using inertial sensors. In *Proceedings of the 19th World Congress of the International Federation of Automatic Control (accepted for publication)*, Cape Town, South Africa, August 2014a.

M. Kok, J. D. Hol, and T. B. Schön. Indoor positioning using ultra-wideband and inertial measurements. *Preprint*, 2014b.

J. Nocedal and S. J. Wright. *Numerical Optimization*. Springer Series in Operations Research, 2nd edition, 2006.

S. Pittet, V. Renaudin, B. Merminod, and M. Kasser. UWB and MEMS based indoor navigation. *Journal of Navigation*, 61(3):369–384, July 2008.

Z. Sahinoglu, S. Gezici, and I. Güvenc. *Ultra-wideband Positioning Systems: Theoretical Limits, Ranging Algorithms, and Protocols*. Cambridge University Press, 2008.

A. H. Sayed, A. Tarighat, and N. Khajehnouri. Network-based wireless location: challenges faced in developing techniques for accurate wireless location information. *IEEE Signal Processing Magazine*, 22(4):24–40, 2005.

S. Sczyslo, J. Schroeder, S. Galler, and T. Kaiser. Hybrid localization using UWB and inertial sensors. In *Proceedings of the IEEE International Conference on Ultra-Wideband (ICUWB)*, volume 3, pages 89–92, Hannover, Germany, September 2008.

Time Domain. `http://www.timedomain.com`, Accessed on April 7, 2014.

Ubisense. `http://www.ubisense.net`, Accessed on April 8, 2014.

Xsens Technologies B.V. `http://www.xsens.com`, Accessed on November 17, 2013.

Paper C

An optimization-based approach to human body motion capture using inertial sensors

Authors: Manon Kok, Jeroen D. Hol and Thomas B. Schön

Edited version of the paper:

M. Kok, J. D. Hol, and T. B. Schön. An optimization-based approach to human body motion capture using inertial sensors. In *Proceedings of the 19th World Congress of the International Federation of Automatic Control (accepted for publication)*, Cape Town, South Africa, August 2014a.

An optimization-based approach to human body motion capture using inertial sensors

Manon Kok[⋆], Jeroen D. Hol[†] and Thomas B. Schön[‡]

[⋆]Dept. of Electrical Engineering,
Linköping University,
SE–581 83 Linköping, Sweden
`manko@isy.liu.se`

[†]Xsens Technologies B.V.,
P.O. Box 559,
7500 AN Enschede, the Netherlands
`jeroen.hol@xsens.com`

[‡]Dept. of Information Technology
Uppsala University,
SE-751 05 Uppsala, Sweden
`thomas.schon@uu.se`

Abstract

In inertial human motion capture, a multitude of body segments are equipped with inertial measurement units, consisting of 3D accelerometers, 3D gyroscopes and 3D magnetometers. Relative position and orientation estimates can be obtained using the inertial data together with a biomechanical model. In this work we present an optimization-based solution to magnetometer-free inertial motion capture. It allows for natural inclusion of biomechanical constraints, for handling of nonlinearities and for using all data in obtaining an estimate. As a proof-of-concept we apply our algorithm to a lower body configuration, illustrating that the estimates are drift-free and match the joint angles from an optical reference system.

1 Introduction

Human body motion capture is used for many applications such as character animation, sports and biomechanical analysis (Xsens Technologies B.V., 2013). It focuses on simultaneously estimating the relative position and orientation of the different body segments (expressed in terms of the joint angles) and estimating the absolute position of the body. Motion capture is often performed using either vision-based technologies (Moeslund et al., 2006) or using inertial sensors. The main advantage of using inertial sensors over vision-based technologies is that they are not restricted in space and do not require line of sight visibility (Welch and Foxlin, 2002). In inertial human body motion capture, the human body is equipped with inertial measurement units (IMUs), consisting of 3D accelerometers, 3D gyroscopes and 3D magnetometers as shown in Figure 1. Each body

Figure 1: Examples of inertial motion capture. Upper left: olympic and world champion speed skating Ireen Wüst wearing an inertial motion capture suit with 17 inertial sensors. Upper right: graphical representation of the estimated orientation and position of the body segments. Lower left and right: experiment showing that line of sight visibility is not necessary for inertial motion capture.

segment's position and orientation (pose) can be estimated by integrating the gyroscope data and double integrating the accelerometer data in time and combining these integrated estimates with a biomechanical model. Inertial sensors are successfully used for full body motion capture in many applications (Xsens Technologies B.V., 2013; Roetenberg et al., 2013; Kang et al., 2011; Yun and Bachmann, 2006).

Inertial sensors inherently suffer from integration drift. When using inertial sensors for orientation estimation they are therefore generally combined with magnetometers. Magnetometer measurements, however, are known to cause problems in motion capture applications since the magnetic field measured at the different sensor locations is typically different (Luinge et al., 2007; Cooper et al., 2009; Favre et al., 2008). Including information from biomechanical constraints, i.e. information about the body segments being rigidly connected, can eliminate the need of using magnetometer measurements. Incorporating these constraints, the sensor's *relative* position and orientation become observable as long as the subject is not standing completely still (Hol, 2011). Estimating joint angles using a pair of inertial sensors, where each sensor estimates its own orientation using an extended Kalman filter (EKF) (Yuan and Chen, 2013) is therefore computationally cheap, but valuable information from biomechanical constraints is lost. Existing approaches therefore include the biomechanical constraints like for instance in Luinge et al. (2007) where an EKF is run using only the accelerometer and gyroscope measurements and a least-squares filter is added to incorporate the biomechanical constraints.

To allow for natural inclusion of biomechanical constraints, we introduce a new optimization-based approach for inertial motion capture. Compared to filtering approaches, optimization-based approaches are computationally expensive. Recent developments in both computational power and in available algorithms have, however, opened up possibilities for solving large-scale problems efficiently and even in real-time (Mattingley and Boyd, 2010). Using an optimization formulation of the problem, a smoothing estimate can be obtained and nonlinearities can be handled. It also opens up possibilities for simultaneously estimating calibration parameters and for incorporating non-Gaussian noise.

The paper is organized as follows. After introducing the problem formulation in Section 2, in Section 3 we will introduce the biomechanical model, discussing the relevant coordinate frames, variables and biomechanical constraints. In Section 4 we will subsequently introduce the dynamic and sensor models. In Section 6 we will discuss experimental results, focusing on a subproblem, namely a lower body configuration consisting of 7 sensors, assuming a known calibration and not including any position aiding. These experiments are intended to serve as a proof-of-concept. A more in-depth analysis including a comparison with other methods is planned for future work.

Note that using inertial sensors and biomechanical constraints only, the *absolute* position is not observable, i.e. any translation of the body's position estimates will lead to an equally valid solution of the estimation problem. For example in the case of the speed skater in Figure 1, the estimated pose of the speed skater will resemble the “true” motion, but the exact location on the ice rink is not observable. This unobservability typically results in a drift of the body's absolute position over time. Because of this, it is not possible to compare our position estimates with those of the optical reference system and for now we focus on analysis of the joint angles. To estimate absolute position it is necessary to include e.g. GPS, ultra-wideband (Hol, 2011) or zero velocity updates when the foot is at stand still (Callmer, 2013; Woodman, 2010) and this is planned for future work.

2 Problem formulation

The use of inertial sensors for human body motion capture requires inertial sensors to be placed on different body segments. The knowledge about the placement of the sensors on the body segments and the body segments' connections to each other by joints can be incorporated using a biomechanical model.

The problem of estimating the relative position and orientation of each body segment is formulated as a constrained estimation problem. Given N measurements $y_{1:N} = \{y_1, \ldots, y_N\}$, a point estimate of the variables z can be obtained as a constrained maximum a posteriori (MAP) estimate, maximizing the posterior density function

$$\begin{aligned} \max_{z} \quad & p(z \mid y_{1:N}) \\ \text{s.t.} \quad & c_{\mathrm{e}}(z) = 0, \end{aligned} \tag{1}$$

where $c_{\mathrm{e}}(z)$ represents the equality constraints. In our problem, z consists of both static parameters θ and time-varying variables $x_{1:N}$. Using this together with the Markov property of the time-varying variables and the fact that the logarithm is a monotonic function, we can rewrite (1) as

$$\begin{aligned} \min_{z=\{x_{1:N},\theta\}} \quad & \underbrace{-\log p(x_1 \mid y_1) - \log p(\theta)}_{\text{initialization}} \\ & \underbrace{-\sum_{t=2}^{N} \log p(x_t \mid x_{t-1}, \theta)}_{\text{dynamic model}} \; \underbrace{-\sum_{t=1}^{N} \log p(y_t \mid x_t, \theta)}_{\text{biomechanical/sensor model}} \\ \text{s.t.} \quad & c_{\mathrm{bio}}(z) = 0. \end{aligned} \tag{2}$$

Obtaining the MAP estimate thus amounts to solving a constrained optimization problem where the constraints $c_{\mathrm{bio}}(z)$ originate from a biomechanical model. The cost function consists of different parts related to the initialization of the variables, a dynamic model for the time-varying states and a biomechanical and sensor model. More details about the variables, the different parts of the cost function and the constraints are provided in Sections 3 and 4.

The optimization problem (2) is solved using an infeasible start Gauss-Newton method (Boyd and Vandenberghe, 2004). The number of variables in the problem will become large already for short experiments and a small number of segments. The problem (2) can, however, still be solved efficiently due to its inherent sparseness.

3 Biomechanical model

A biomechanical model represents the human body as consisting of body segments connected by joints. In the example application in Figure 1 the body is modeled as consisting of 23 segments, whereas Figure 2 illustrates two of these body segments. These can be thought of as the upper and lower leg, each with a sensor attached to it. The main purpose of Figure 2 is to introduce the different coordinate frames, variables and calibration parameters. These definitions can

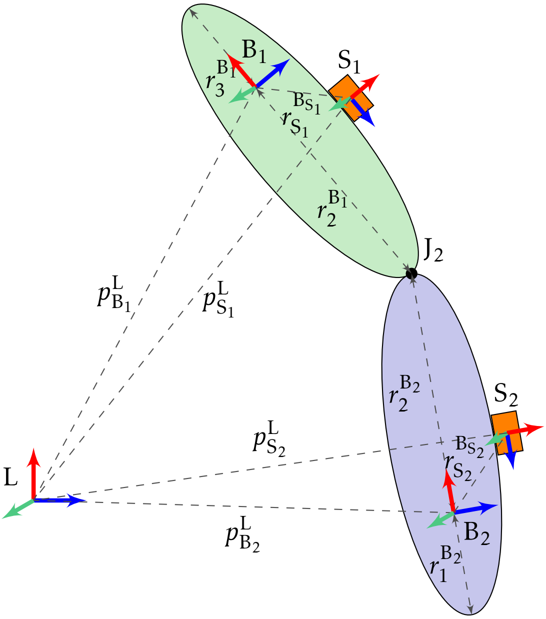

Figure 2: *Connection of two segments and definition of the variables and coordinate frames.*

straightforwardly be extended to any sensor and any body segment. The relevant coordinate frames are:

The local coordinate frame L aligned with the local gravity vector, with the z-axis pointing up. The horizontal directions are defined according to any convenient choice of local coordinates.

The body segment coordinate frame $\mathbf{B}_j$ fixed to the bone in body segment B_j. Its origin can be anywhere along the bone, but it is usually in the center of rotation of a joint.

The sensor coordinate frame $\mathbf{S}_i$ of the moving IMU S_i. Its origin is located in the center of the accelerometer triad and its axes are aligned to the casing. All measurements of the IMU are resolved in this frame.

In setting up the optimization problem (2), the first step is to define the set of sensors $\mathcal{S}$, the set of body segments $\mathcal{B}$ and the set of joints $\mathcal{J}$ in the problem. Each inertial sensor needs to be mounted on the body, and sensor S_i is assumed to be placed on body segment B_{S_i}. The distance $r_{S_i}^{B_{S_i}}$ and orientation $q^{B_{S_i}S_i}$ of sensor S_i with respect to body segment B_{S_i} are without loss of generality assumed to be known from calibration.

Our knowledge of the human body can be used to identify which body segments are connected by which joints, i.e. the set $\mathcal{B}_{J_k}$ needs to be determined for each joint

J_k. To express the location of the joint in the body frames of the connected body segments, the distances $r_k^{\mathrm{B}_j}$ from the body frame B_j to joint k, need to be defined for all joints $\mathrm{J}_k \in \mathcal{J}$ and all $\mathrm{B}_j \in \mathcal{B}_{\mathrm{J},k}$. We assume without loss of generality that they are known from calibration. Generally, all joints are assumed to be ball-and-socket joints, but we incorporate additional knowledge about a subset of the joints, denoted by $\mathcal{H}$, which we assume to be hinge joints.

For reasons that will be discussed in Section 4, we define the set of time steps in the optimization as $\mathcal{T}$ rather than explicitly summing over all time steps $t = 1 \ldots N$ as in (2). The variables in the optimization problem are then given by

- the position $p^{\mathrm{L}}_{\mathrm{S}_i,t}$ and velocity $v^{\mathrm{L}}_{\mathrm{S}_i,t}$ of sensor S_i in the local frame L, $\forall$ $\mathrm{S}_i \in \mathcal{S}$ and $\forall$ $t \in \mathcal{T}$,
- the orientation $q_t^{\mathrm{LS}_i}$ of sensor S_i with respect to the local frame L, $\forall$ $\mathrm{S}_i \in \mathcal{S}$ and $\forall$ $t \in \mathcal{T}$,
- the position $p^{\mathrm{L}}_{\mathrm{B}_j,t}$ of body segment B_j in the local frame L, $\forall$ $\mathrm{B}_j \in \mathcal{B}$ and $\forall$ $t \in \mathcal{T}$,
- the orientation $q_t^{\mathrm{LB}_j}$ of body segment B_j with respect to the local frame L, $\forall$ $\mathrm{B}_j \in \mathcal{B}$ and $\forall$ $t \in \mathcal{T}$,
- the gyroscope bias b_{ω,S_i} of sensor S_i, $\forall$ $\mathrm{S}_i \in \mathcal{S}$,
- the mean acceleration state of one of the sensors $\mathrm{S}_i \in \mathcal{S}$, $\forall$ $t \in \mathcal{T}$.

Defining the number of sensors as N_S and the number of body segments as N_B, the number of variables in the optimization problem is $z \in \mathbb{R}^{(9N_S+6N_B+3)N+3N_S}$. When we solve the optimization problem, we encode the rotation states using a three-dimensional state vector (Crassidis et al., 2007; Grisetti et al., 2010; Hol, 2011). Throughout the paper, we typically interchangeably make use of the unit quaternion q^{LS} and the rotation matrix R^{LS} as representations of the orientation. The quaternion conjugate, representing the inverse rotation will be represented by $(q^{\mathrm{LS}})^c = q^{\mathrm{SL}}$. Similarly for the rotation matrix, $(R^{\mathrm{LS}})^{\mathsf{T}} = R^{\mathrm{SL}}$.

More details about the gyroscope bias variables and the reason for the inclusion of the mean acceleration state will be given in Section 4.2.

Based on the biomechanical model it is possible to derive relations between the different variables. We will categorize them in three classes.

Joints between the body segments. The constraints $c_{\mathrm{bio}}(z)$ in the optimization problem (2) enforce the body segments to be connected at the joint locations at all times,

$$c_{\mathrm{bio}}(z) = p^{\mathrm{L}}_{\mathrm{B}_m,t} + R_t^{\mathrm{LB}_m} r_k^{\mathrm{B}_m} - p^{\mathrm{L}}_{\mathrm{B}_n,t} - R_t^{\mathrm{LB}_n} r_k^{\mathrm{B}_n}, \qquad B_n, B_m \in \mathcal{B}_{\mathrm{J}_k}, \tag{3}$$

which is included for all $\mathrm{J}_k \in \mathcal{J}$ and $t \in \mathcal{T}$. This leads to N_J constraints at each time step t in the optimization problem (2), where N_J is the number of joints.

Placement of the sensors on the body segments. The position and orientation of sensor S_i can be expressed in terms of its position and orientation on body segment $\mathrm{B}_{\mathrm{S}_i}$. Ideally, this can be incorporated using equality constraints in (2). However, it is physically impossible to place the sensor directly on the bone. Hence, it has to be placed on the soft tissue and the sensor will inevitably move slightly with respect to the bone. We therefore model the position and orientation of sensor S_i on body segment $\mathrm{B}_{\mathrm{S}_i}$ as

$$p^{\mathrm{L}}_{\mathrm{S}_i,t} = p^{\mathrm{L}}_{\mathrm{B}_{\mathrm{S}_i},t} + R^{\mathrm{LB}_{\mathrm{S}_i}}_t \left(r^{\mathrm{B}_{\mathrm{S}_i}}_{\mathrm{S}_i} + e^{\mathrm{B}_{\mathrm{S}_i}}_{\mathrm{p},t} \right), \tag{4a}$$

$$q^{\mathrm{LS}_i}_t = q^{\mathrm{LB}_{\mathrm{S}_i}}_t \, q^{\mathrm{B}_{\mathrm{S}_i}\mathrm{S}_i} \exp\left(\tfrac{1}{2} e^{\mathrm{S}_i}_{\mathrm{q},t} \right), \tag{4b}$$

where we assume $e^{\mathrm{B}_{\mathrm{S}_i}}_{\mathrm{p},t} \sim \mathcal{N}(0, \Sigma_{\mathrm{p}})$ and $e^{\mathrm{S}_i}_{\mathrm{q},t} \sim \mathcal{N}(0, \Sigma_{\mathrm{q}})$.

Rotational freedom of the joints. For some joints, it is known that their rotation is (mainly) limited to one or two axes. An example of this is the knee which is a hinge joint, although it can in practice flex a little around the other axes too. Minimizing

$$e_{\mathrm{J}_k,t} = \begin{bmatrix} n_1^{\mathrm{T}} \\ n_3^{\mathrm{T}} \end{bmatrix} \left(R^{\mathrm{LB}_m}_t \right)^{\mathrm{T}} R^{\mathrm{LB}_n}_t n_2, \qquad B_n, B_m \in \mathcal{B}_{\mathrm{J}_k}, \tag{5}$$

where n_1, n_2 and n_3 denote the different axis directions and $e_{\mathrm{J}_k,t} \sim \mathcal{N}(0, \Sigma_k)$, will minimize the rotation around any but the n_2-axis. This cost function can be included at any time t for any joint k that is a hinge joint, i.e. $\forall\ \mathrm{J}_k \in \mathcal{H}, \forall\ t \in \mathcal{T}$. Note that inclusion of this knowledge is optional in the algorithm.

4 Dynamic and sensor models

The sensor's position, velocity and orientation at each time instance can be related by a dynamic model in which the accelerometer and gyroscope measurements are used as inputs (Gustafsson, 2012; Hol, 2011). In this work we choose a slightly different approach to reduce the number of variables in the optimization problem (2). To achieve high update rates using a relatively small number of variables, we use an approach similar to the one discussed by Savage (1998a,b). Hence, strapdown inertial integration, in which the accelerometer and gyroscope signals are integrated, is run at high update rates. This leads to accelerometer measurements Δp and Δv representing a difference in position and velocity and gyroscope measurements Δq representing a difference in orientation. These are integrated for $\frac{T_s}{T}$ times, where T_s is the sampling time of the inertial sensors and T is the sampling time used in the optimization problem (2).

4.1 Dynamic model

The position, velocity and orientation of each sensor S_i are related from time t to time $t + T$ using the accelerometer measurements $\Delta p^{\mathrm{S}_i}_t$, $\Delta v^{\mathrm{S}_i}_t$ and the gyroscope measurements $\Delta q_t^{\mathrm{S}_i}$. The position and velocity states at each time step are modeled according to

$$\begin{aligned} p^{\mathrm{L}}_{\mathrm{S}_i,t+T} =& p^{\mathrm{L}}_{\mathrm{S}_i,t} + T v^{\mathrm{L}}_{\mathrm{S}_i,t} + \\ & R_t^{\mathrm{LS}_i} \left(\Delta p_t^{\mathrm{S}_i} + w_{\mathrm{p},t}^{\mathrm{S}_i} \right) + \tfrac{T^2}{2} g^{\mathrm{L}}, \end{aligned} \tag{6a}$$

$$v^{\mathrm{L}}_{\mathrm{S}_i,t+T} = v^{\mathrm{L}}_{\mathrm{S}_i,t} + R_t^{\mathrm{LS}_i} \left(\Delta v_t^{\mathrm{S}_i} + w_{\mathrm{v},t}^{\mathrm{S}_i} \right) + T g^{\mathrm{L}}, \tag{6b}$$

where $\Delta p_t^{\mathrm{S}_i}$ and $\Delta v_t^{\mathrm{S}_i}$ denote the inputs based on the accelerometer measurements. The noise terms are modeled as $w_{\mathrm{p},t} \sim \mathcal{N}(0, Q_{\mathrm{p}})$ and $w_{\mathrm{v},t} \sim \mathcal{N}(0, Q_{\mathrm{v}})$. The earth gravity is denoted by g^{L}. The orientation states are modeled as

$$q_{t+T}^{\mathrm{LS}_i} = q_t^{\mathrm{LS}_i} \Delta q_t^{\mathrm{S}_i} \exp\left(\tfrac{1}{2} w_{\mathrm{q},t}^{\mathrm{S}_i} \right), \tag{6c}$$

where $\Delta q_t^{\mathrm{S}_i}$ denotes the gyroscope measurements, corrected for the estimated gyroscope bias, and $w_{\mathrm{q},t}^{\mathrm{S}_i} \sim \mathcal{N}(0, Q_{\mathrm{q}})$.

Since (6) models the states in terms of their value at the previous time step, the state at the first time instance needs to be treated separately. The orientation $q_1^{\mathrm{LS}_i}$ of each sensor S_i is estimated using the first accelerometer and magnetometer sample of that sensor. Note that this is the only place in the algorithm where magnetometer measurements are used. The variables $q_1^{\mathrm{LS}_i}$ are then initialized around this estimated orientation with additive noise $e_{\mathrm{q}_1}^{\mathrm{S}_i} \sim \mathcal{N}(0, \Sigma_{\mathrm{q}_1})$. The position $p^{\mathrm{L}}_{\mathrm{S}_i,1}$ of one of the sensors is without loss of generality initialized around zero with additive noise $e_{\mathrm{p}_1} \sim \mathcal{N}(0, \Sigma_{\mathrm{p}_1})$. This defines the origin of the local coordinate frame L.

4.2 Sensor model

The gyroscope measurements are affected by a slowly time-varying sensor bias. For relatively short experiments, the sensor biases of all sensors $\mathrm{S}_i \in \mathcal{S}$ can be assumed to be constant. Hence, we include only one three-dimensional variable for each sensor to represent the gyroscope bias. This variable b_{ω,S_i} is modeled as $b_{\omega,\mathrm{S}_i} \sim \mathcal{N}(0, \Sigma_{\mathrm{b}_\omega})$.

As described in Section 1, we do not include position aiding in our problem, resulting in only *relative* position and orientation observability. A problem that can be encountered for this case is that of so-called gravity leakage. Because the subject's *absolute* inclination is unobservable, the gravity vector risks being misinterpreted as an acceleration. In the case of stationary measurements, when the accelerometer only measures the gravity vector, the accelerometer measurements can be used as a source of absolute inclination information. In case of motion, the accelerometer measurements will measure an additional acceleration. It can, however, still be assumed that the mean acceleration over a certain time period is zero (Luinge, 2002). We therefore assume that one sensor follows this acceleration model for all $t \in \mathcal{T}$, up to some noise $e_{\mathrm{a}} \sim \mathcal{N}(0, \Sigma_{\mathrm{a}})$.

5 Resulting algorithm

The biomechical model from Section 3 and the dynamic and sensor models from Section 4 can be combined and used to describe the probability density functions in (2). Eliminating all constant terms from the optimization, this results in a constrained weighted least-squares problem. This problem is given by

$$\begin{aligned}
\min_{z} \sum_{t\in\mathcal{T}} \sum_{\mathrm{S}_i\in\mathcal{S}} & \Bigg(\underbrace{\|e^{\mathrm{S}_i}_{\mathrm{p},t}\|^2_{\Sigma_\mathrm{p}^{-1}} + \|e^{\mathrm{B}_{\mathrm{S}_i}}_{\mathrm{q},t}\|^2_{\Sigma_\mathrm{q}^{-1}}}_{\text{placement of sensors on body (4)}} \underbrace{+ \|w^{\mathrm{S}_i}_{\mathrm{p},t}\|^2_{Q_\mathrm{p}^{-1}} + \|w^{\mathrm{S}_i}_{\mathrm{v},t}\|^2_{Q_\mathrm{v}^{-1}} + \|w^{\mathrm{S}_i}_{\mathrm{q},t}\|^2_{Q_\mathrm{q}^{-1}} \Bigg)}_{\text{dynamic model (6)}} \\
& + \sum_{\mathrm{S}_i\in\mathcal{S}} \underbrace{\|b_{\omega,\mathrm{S}_i}\|^2_{\Sigma_{\mathrm{b}_\omega}^{-1}}}_{\text{gyroscope bias}} + \sum_{t\in\mathcal{T}} \sum_{\mathrm{J}_k\in\mathcal{H}} \underbrace{\|e_{\mathrm{J}_k,t}\|^2_{\Sigma_k^{-1}}}_{\text{hinge (5)}} \\
& \underbrace{+ \|e_{\mathrm{p}_1}\|^2_{\Sigma_{\mathrm{p}_1}^{-1}} + \sum_{\mathrm{S}_i\in\mathcal{S}} \|e^{\mathrm{S}_i}_{\mathrm{q}_1}\|^2_{\Sigma_{\mathrm{q}_1}^{-1}}}_{\text{initialization}} + \sum_{t\in\mathcal{T}} \underbrace{\|e_{\mathrm{a},t}\|^2_{\Sigma_\mathrm{a}^{-1}}}_{\text{acceleration model}}, \\
\text{s.t. } c_{\mathrm{bio}}(z) = {} & p^{\mathrm{L}}_{\mathrm{B}_m,t} + R^{\mathrm{LB}_m}_t r^{\mathrm{B}_m}_k - p^{\mathrm{L}}_{\mathrm{B}_n,t} - R^{\mathrm{LB}_n}_t r^{\mathrm{B}_n}_k, \\
& B_n, B_m \in \mathcal{B}_{\mathrm{J}_k} \quad \forall\ \mathrm{J}_k \in \mathcal{J}, \forall\ t \in \mathcal{T},
\end{aligned} \tag{7}$$

where the constraints are based on (3).

The complete algorithm is summarized in Algorithm 1. Note that in our current implementation the optimization is performed over the entire data set and the computations are therefore done offline. We plan to extend the approach to a moving horizon approach (Rao et al., 2001) to enable processing of longer data sets and to allow for online estimation.

The covariance matrices in (7) representing the sensor covariances are determined using Allan variance analysis (El-Sheimy et al., 2008). The covariance matrices related to the placement of the sensors on the body, the hinge constraint and the acceleration model, do not represent any physical quantities and are chosen more or less ad hoc. Experiments have shown that the solution of the optimization problem is not very sensitive to the tuning of these values.

The optimization (7) is started using an initial estimate of the variables z_0. All variables z are initialized at zero except for the orientations at the first time step, which are initialized around their estimated orientation as described in Section 4.2. This is an infeasible solution, justifying the need for an infeasible start optimization algorithm.

6 Experiments

We validated our approach with experiments using an MVN Awinda system which is a wireless inertial motion capture system with 17 sensors attached to different body segments (Xsens Technologies B.V., 2013) as shown in Figure 3. An optical

Algorithm 1 Inertial human motion capture

```
1. Define the set of sensors $\mathcal{S}$, the set of body segments $\mathcal{B}$ and the set of joints $\mathcal{J}$. Mount the inertial sensors on the body and
    (a) define for each sensor $\mathrm{S}_i \in \mathcal{S}$ on which body segment $\mathrm{B}_{\mathrm{S}_i} \in \mathcal{B}$ it is placed. Calibrate the system to obtain the position $r_{\mathrm{S}_i}^{\mathrm{B}_{\mathrm{S}_i}}$ and orientation $q^{\mathrm{B}_{\mathrm{S}_i}\mathrm{S}_i}$ of each sensor $\mathrm{S}_i \in \mathcal{S}$ on body segment $\mathrm{B}_{\mathrm{S}_i} \in \mathcal{B}$,
    (b) define the set of body segments $\mathcal{B}_{\mathrm{J}_k}$ connected to each joint $k$ for all $\mathrm{J}_k \in \mathcal{J}$. Calibrate the system to obtain the distances $r_k^{\mathrm{B}_j}$ of each body segment coordinate frames $\mathrm{B}_j \in \mathcal{B}_{\mathrm{J}_k}$ to the different joints $k$,
    (c) define the subset $\mathcal{H}$ of joints that are restricted in their rotations and can be regarded as a hinge joint.
2. Perform an experiment collecting inertial measurements $\Delta p_t^{\mathrm{S}_i}, \Delta v_t^{\mathrm{S}_i}$ and $\Delta q_t^{\mathrm{S}_i}$ and a magnetometer measurement at $t = 1$, $y_{\mathrm{m},1}^{\mathrm{S}_i}$.
3. Postprocess the data
    (a) Initialize $z_0$ and set $l = 0$.
    (b) Determine the values of the cost functions and the constraints in (2), their Jacobians and the approximate Hessian of the cost function. Determine a step direction using an infeasible start Gauss-Newton algorithm and update $z_l \to z_{l+1}$.
    (c) Set $l := l + 1$ and iterate from 3(b) until the algorithm is converged and the solution $z_{l+1}$ is feasible.
```

motion capture system has been used as a source of reference data. Since our focus is on the legs, one leg has been equipped with optical markers, providing reference position and orientation of the foot sensor, lower leg sensor, upper leg sensor and – not visible in the figure – the pelvis sensor.

Inertial data has been collected at 30 Hz. The sensors, however, run the strapdown integration algorithm discussed in Section 4 internally at 600 Hz to capture the high bandwidth of the measurement signals during impact, for instance during foot impact on the ground. To speed up the computations, the optimization algorithm itself has been run at a frequency of 10 Hz.

The optimization problem typically converges in a few iterations. To solve the problem for an experiment of 10 seconds takes about 5 minutes on an AMD X4 2.8 GHz processor for a first inefficient Matlab implementation of the algorithm. Initial tests with a C-implementation, however, show that speed improvements of up to 500 times are easily obtained. Taking into account that at the moment we postprocess the whole data set while for a real-time application a moving horizon can be used, we think that a real-time implementation of the algorithm is indeed quite possible.

The collected inertial data has been postprocessed used in the optimization problem (2) for a lower body configuration consisting of a set $\mathcal{S}$ of 7 sensors placed on 7 body segments $\mathcal{B}$: both feet, both lower legs, both upper legs and the pelvis.

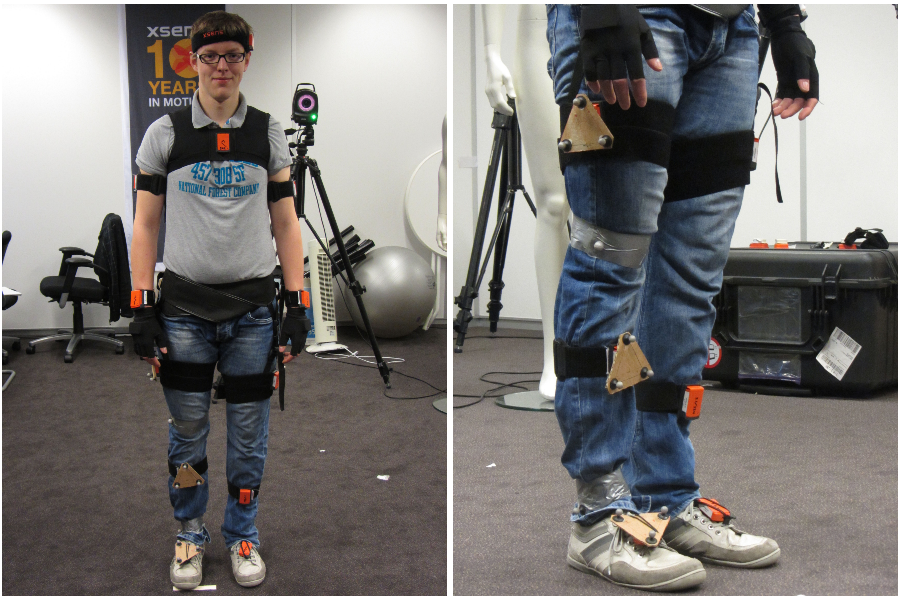

Figure 3: *Experimental setup where the human body is equipped with inertial sensors on different body segments. Optical markers for the reference system have been placed on the right foot sensor, right lower and upper leg sensors and – not visible in the figure – the pelvis.*

The position of each sensor $\mathrm{S}_i \in \mathcal{S}$ on the body segment $r_{\mathrm{S}_i}^{\mathrm{B}_{\mathrm{S}_i}}$ has been manually measured. The orientations of the sensors on the body segments $q^{\mathrm{B}_{\mathrm{S}_i}\mathrm{S}_i}$ for all $\mathrm{S}_i \in \mathcal{S}$ have been determined by standing still in a pre-determined pose as described by Roetenberg et al. (2013). The 7 body segments are connected by 6 joints $\mathcal{J}$ of which the two knee joints are assumed to be hinge joints. Calibrating for the distances $r_k^{\mathrm{B}_j}$ amounts to defining the distances between the different joint centers which is again done by manual measuring. We acknowledge that this is an inaccurate calibration method and as future work we therefore plan to extend the algorithm to automatically estimate these calibration parameters.

Figure 4 visualizes the pose of the lower body of a walking subject estimated using Algorithm 1 for parts of an experiment. Note that our experimental setup does allow for accurate *absolute* position estimates. The location of the different steps has therefore been corrected for one joint location using the position estimates from the optical reference system. The steps are taken from a short experiment and the optimization is run at 30 Hz for plotting purposes.

To compare our relative orientation results to those of the optical reference system, we focus on the estimated joint angle of the right knee during an experiment of around 37 seconds. Joint angles are defined as the angle between two connected body segments at the joint center. For the knee joint, the bending of

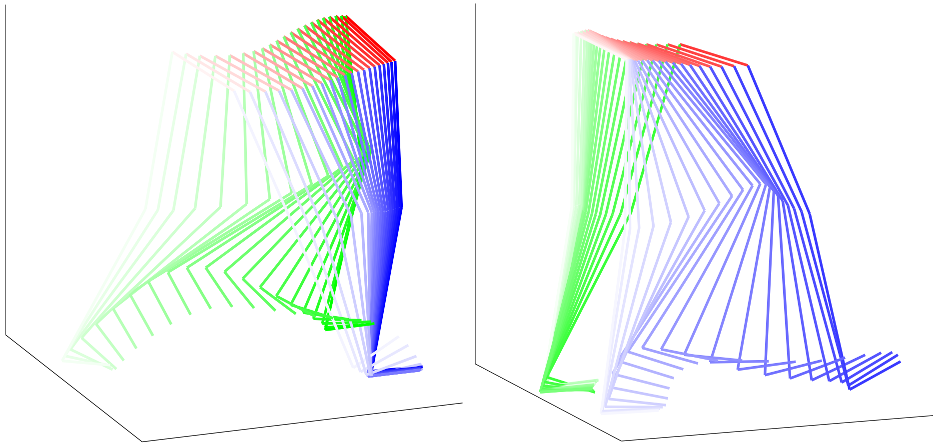

Figure 4: *Estimated pose of the lower body at different times during a step of the left leg (left) and the right leg (right). The view is chosen such that we view the subject from the right, and the right leg is depicted in blue, the left leg in green and the connection between the hips in red.*

the knee during walking is referred to as flexion/extension. The rotation around the other two axes (abduction/adduction and internal/external rotation) are generally quite small for this joint. Because it is not possible to observe the joint center and sensors/markers are generally placed on the soft tissue instead of on the bone, computation of joint angles depends on a model of the joint locations in the body. Theoretically, it is possible to estimate the joint angle from the orientation results of the sensor if the exact location of the sensors with respect to the joints is known, i.e. in case of a perfect calibration, and if the sensors would be rigidly attached to the bone. In practice this is clearly not possible. However, since both the inertial sensors and the optical reference markers are placed on the same location on the body segments as shown in Figure 3, it is still possible to compare the angles to assess the quality of our estimates.

To be able to compare our joint angle estimates to those of the reference system, a coordinate frame alignment between the sensor coordinate frame and the coordinate frame of the optical markers needs to be performed. This has been done as described by Hol (2011). Note that due to limited excitation of the upper leg sensor, it was not possibly to do this alignment based on the sensor signals. Instead, the alignment has been performed based on the joint angle estimates. The joint angle estimates from our algorithm can be seen to match the joint angles from the optical reference system. A more quantitative analysis can be performed when the calibration parameters are properly estimated and position aiding is included. Note that due to the limited size of the measurement volume of the optical reference system, the movements are quite restricted and at some time instances in the experiment the optical reference data is not present.

From our optimization algorithm it is also possible to estimate the joint angles from the angles of the body segments. These are included in red in Figure 5. There is no validation for the angles obtained in this way, but the estimated abduction/adduction and internal/external rotation are considerably closer to zero, as we would expect from our knowledge that these rotations are quite small.

7 Conclusions and future work

An optimization approach to inertial human body motion capture has been developed, capable of estimating the relative position and orientation of the body segments. Experimental results show that the algorithm works well, quickly converging to a feasible solution and resulting in drift-free joint angle estimates which match the joint angles from an optical reference system.

We plan to extend the approach to also estimate the calibration parameters and to include position aiding in the form of zero velocity updates at stand still and ultra-wideband position aiding (Hol et al., 2009). This will also allow a more quantitative analysis of the results. Future work also includes adding more body segments, modeling of non-Gaussian noise where appropriate and implementing a moving horizon estimation version of the algorithm.

Acknowledgements

This work is supported by MC Impulse, a European Commission, FP7 research project, by CADICS, a Linnaeus Center funded by the Swedish Research Council (VR) and by BALANCE, a European Commission, FP7 research project. The authors would like to thank Dr. Daniel Roetenberg for valuable discussions and Raymond Zandbergen for implementation support.

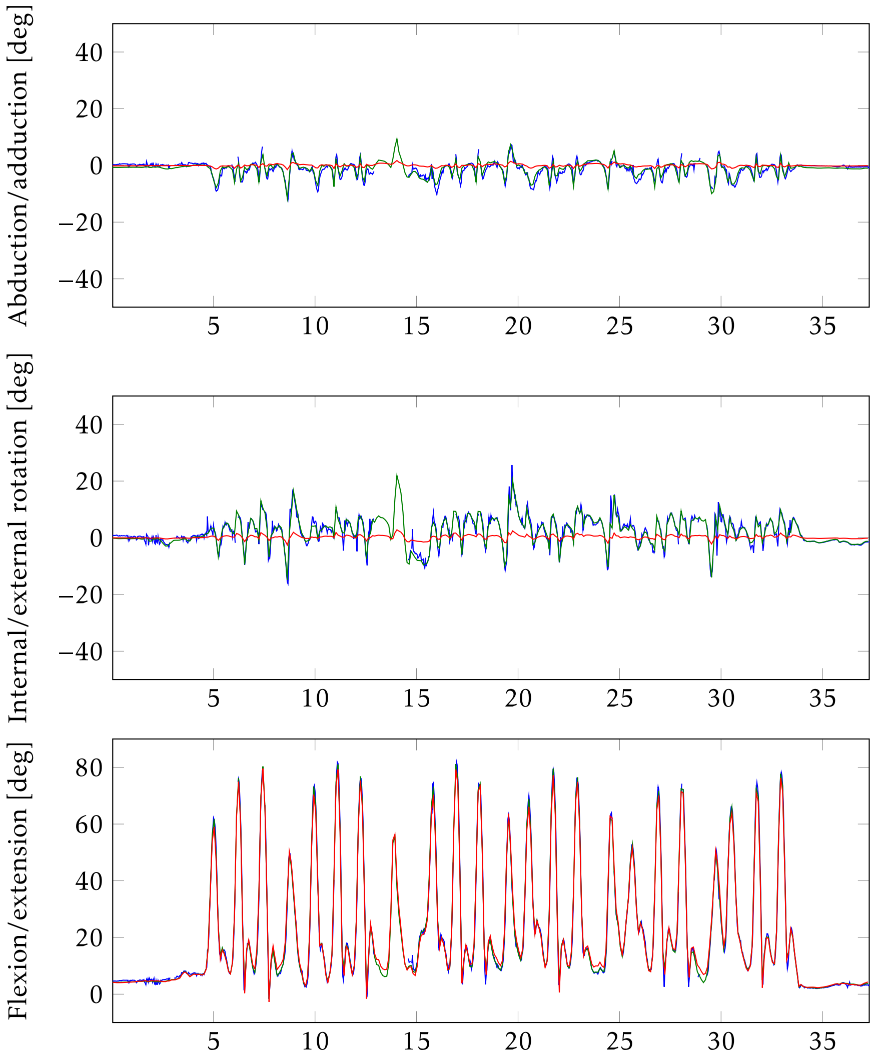

Figure 5: *Knee joint angles for the right knee for an experiment consisting of 23 steps. The optical reference data is plotted in blue, the joint angle estimated from the sensor's orientations, using our algorithm is plotted in green, the joint angle from the body segment orientations is plotted in red. Best viewed in color.*

Bibliography

S. Boyd and L. Vandenberghe. *Convex Optimization*. Cambridge University Press, 2004.

J. Callmer. *Autonomous Localization in Unknown Environments*. PhD thesis, Linköping University, Sweden, June 2013.

G. Cooper, I. Sheret, L. McMillan, K. Siliverdis, N Sha, D. Hodgins, L. Kenney, and D. Howard. Inertial sensor-based knee flexion/extension angle estimation. *Journal of Biomechanics*, 42(16):2678 – 2685, 2009.

J. L. Crassidis, F. L. Markley, and Y. Cheng. A survey of nonlinear attitude estimation methods. *Journal of Guidance, Control, and Dynamics*, 30(1):12–28, 2007.

N. El-Sheimy, H. Hou, and X. Niu. Analysis and modeling of inertial sensors using Allan variance. *IEEE Transactions on Instrumentation and Measurement*, 57(1):140–149, 2008.

J. Favre, B. M. Jolles, R. Aissaoui, and K. Aminian. Ambulatory measurement of 3D knee joint angle. *Journal of biomechanics*, 41(5):1029–1035, 2008.

G. Grisetti, R. Kummerle, C. Stachniss, U. Frese, and C. Hertzberg. Hierarchical optimization on manifolds for online 2D and 3D mapping. In *Proceedings of the IEEE International Conference on Robotics and Automation (ICRA)*, pages 273–278, Anchorage, Alaska, 2010.

F. Gustafsson. *Statistical Sensor Fusion*. Studentlitteratur, 2012.

J. D. Hol. *Sensor Fusion and Calibration of Inertial Sensors, Vision, Ultra-Wideband and GPS*. PhD thesis, Linköping University, Sweden, June 2011.

J. D. Hol, F. Dijkstra, H. Luinge, and T. B. Schön. Tightly coupled UWB/IMU pose estimation. In *Proceedings of the IEEE International Conference on Ultra-Wideband (ICUWB)*, pages 688–692, Vancouver, Canada, September 2009.

D. H. Kang, Y. J. Jung, A. J. Park, and J. W. Kim. Human body motion capture system using magnetic and inertial sensor modules. In *Proceedings of the 5th international universal communication symposium (IUCS)*, Gumi, Korea, October 2011.

M. Kok, J. D. Hol, and T. B. Schön. An optimization-based approach to human body motion capture using inertial sensors. In *Proceedings of the 19th World Congress of the International Federation of Automatic Control (accepted for publication)*, Cape Town, South Africa, August 2014.

H. J. Luinge. *Inertial Sensing of Human Movement*. PhD thesis, University of Twente, Enschede, the Netherlands, October 2002.

H. J. Luinge, P. H. Veltink, and C. T. M. Baten. Ambulatory measurement of arm orientation. *Journal of Biomechanics*, 40(1):78–85, 2007.

J. Mattingley and S. Boyd. Real-time convex optimization in signal processing. *IEEE Signal Processing Magazine*, 27(3):50–61, 2010.

T. B. Moeslund, A. Hilton, and V. Krüger. A survey of advances in vision-based human motion capture and analyis. *Computer Vision and Image Understanding*, 104(2-3):90–126, 2006.

C. V. Rao, J. B. Rawlings, and J. H. Lee. Constrained linear state estimation - a moving horizon approach. *Automatica*, 37(10):1619–1628, 2001.

D. Roetenberg, H. J. Luinge, and P. Slycke. Xsens MVN: Full 6DOF human motion tracking using miniature inertial sensors, May 2013.

P. G. Savage. Strapdown inertial navigation integration algorithm design part 1: Attitude algorithms. *Journal of Guidance, Control and Dynamics*, 21(1):19–28, 1998a.

P. G. Savage. Strapdown inertial navigation integration algorithm design part 2: Velocity and position algorithms. *Journal of Guidance, Control and Dynamics*, 21(2):208–221, 1998b.

G. Welch and E. Foxlin. Motion tracking: No silver bullet, but a respectable arsenal. *IEEE Computer Graphics and Applications*, 22(6):24–38, 2002.

O. J. Woodman. *Pedestrian localisation for indoor environments*. PhD thesis, University of Cambridge, United Kingdom, September 2010.

Xsens Technologies B.V. `http://www.xsens.com`, Accessed on November 17, 2013.

Q. Yuan and I.-M. Chen. 3-D localization of human based on an inertial capture system. *IEEE Transactions on Robotics*, 29(3):806–812, 2013.

X. Yun and E. R. Bachmann. Design, implementation, and experimental results of a quaternion-based Kalman filter for human body motion tracking. *IEEE Transactions on Robotics*, 22(6):1216–1227, 2006.

Paper D

MEMS-based inertial navigation based on a magnetic field map

Authors: Manon Kok, Niklas Wahlström, Thomas B. Schön, Fredrik Gustafsson

Edited version of the paper:

M. Kok, N. Wahlström, T. B. Schön, and F. Gustafsson. MEMS-based inertial navigation based on a magnetic field map. In *Proceedings of the 38th International Conference on Acoustics, Speech, and Signal Processing (ICASSP)*, pages 6466–6470, Vancouver, Canada, May 2013.

MEMS-based inertial navigation based on a magnetic field map

Manon Kok⋆, Niklas Wahlström⋆, Thomas B. Schön†, Fredrik Gustafsson⋆

⋆Dept. of Electrical Engineering,
Linköping University,
SE–581 83 Linköping, Sweden
{manko,nikwa,fredrik}@isy.liu.se

†Dept. of Information Technology
Uppsala University,
SE-751 05 Uppsala, Sweden
thomas.schon@uu.se

Abstract

This paper presents an approach for 6D pose estimation where MEMS inertial measurements are complemented with magnetometer measurements assuming that a model (map) of the magnetic field is known. The resulting estimation problem is solved using a Rao-Blackwellized particle filter. In our experimental study the magnetic field is generated by a magnetic coil giving rise to a magnetic field that we can model using analytical expressions. The experimental results show that accurate position estimates can be obtained in the vicinity of the coil, where the magnetic field is strong.

1 Introduction

With the reducing cost of accelerometers and gyroscopes (inertial sensors) and magnetometers, these sensor are becoming increasingly available in day-to-day life. It is for instance common that these sensors are present in modern smartphones. Positioning based on inertial sensors alone suffers greatly from drift and does not give reliable estimates for any but the highest quality sensors. Because of this, sensors such as GPS and ultra-wideband are often used as an aiding source (Hol, 2011). While GPS solutions only work for outdoor applications, indoor solutions are often highly dependent on additional infrastructure.

Magnetometers are a reliable source of information due to their high sampling rates and reliable sensor readings. They measure the superposition of the local earth magnetic field and the magnetic field induced by magnetic structures in the vicinity. Magnetometers are widely used as a source of heading information, relying on the assumption that no magnetic disturbances are present. Especially in indoor applications this assumption is often violated due to the presence of steel in the construction of buildings and objects like radiators, tables and chairs.

This paper presents a method to obtain accurate position and orientation estimates based on inertial and magnetometer data assuming a map of the magnetic field is known. This enables positioning with widely available sensors, without requirements on additional infrastructure.

In recent years, the idea of using the presence of magnetic disturbances as a source of position information has started appearing in the literature. Most interest is from the robot localization perspective where odometry information is available (Suksakulchai et al., 2000; Navarro and Benet, 2009; Vallivaara et al., 2011; Georgiou and Dai, 2010). Generally, in these applications localization is only considered in 2D, and the sensor is assumed to be rotating around only one axis. To the best of the authors' knowledge, little work has been done on combining inertial and magnetometer measurements, for example Vissière et al. (2007); Dorveaux et al. (2011). This is a more challenging problem compared to using odometry information, since low grade inertial measurement units (IMUs) generally have poor dead-reckoning performance. The approach presented in Vissière et al. (2007) is not based on magnetic field maps, but uses knowledge about the physical properties of the magnetic field and its gradient to aid localization using an extended Kalman filter approach. Other approaches focus on using sensors in smartphones for localization (Chung et al., 2011; IndoorAtlas, 2012; Gozick et al., 2011) and consider magnetometer data only or very limited information from the inertial sensors. The direction of the magnetic field can, however, only be derived from the magnetic field measurements when the sensor orientation is known. Not estimating the full orientation therefore poses constraints on the allowed sensor rotations. In our approach no constraints on the sensor rotations are required since the full 6D pose is estimated.

To isolate the problem of localization inside a known magnetic field map from the problem of obtaining the map, this work assumes that the magnetic field map is known and is generated by a magnetic coil. The reason for using a magnetic coil is that it is one of the few cases for which the magnetic field can be computed analytically. In other words, we have a perfect model describing the magnetic field produced by the magnetic coil. The magnetic field measurements can be described as a nonlinear function of the sensor position in this map and its orientation with respect to the map.

2 Models

Before introducing the dynamic and measurement equations, the relevant coordinate frames and the state vector will be introduced. All measurements are assumed to be obtained in the body coordinate frame denoted by b, which is the coordinate frame of the measurement unit with the origin in the center of the accelerometer triad. The position is tracked in the earth coordinate frame denoted by e, which is fixed in the world. The magnetic field map is represented in the map coordinate frame denoted by m whose orientation is assumed to be aligned with that of the coil. The origin of the earth coordinate frame e is assumed to coincide with that of the map coordinate frame and with the center of the magnetic coil.

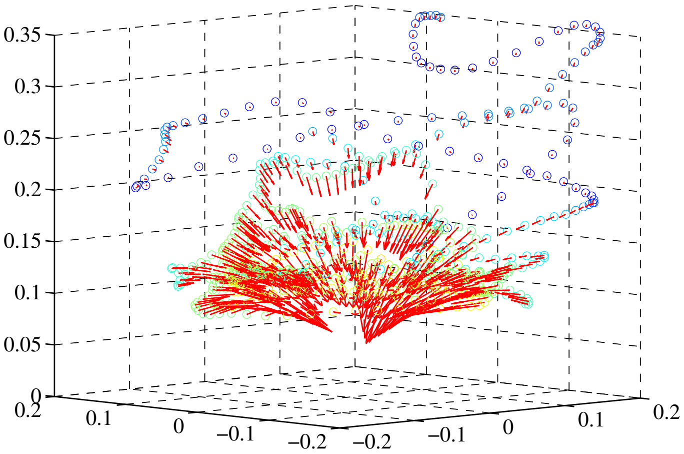

Figure 1: *Magnetometer measurements represented in the earth coordinate frame. The measurements have been preprocessed by subtracting the earth magnetic field. The magnitude is indicated by the colors and the direction by the arrows.*

The relevant state vector consists of the sensor's position p^{e} and velocity v^{e}, its orientation with respect to the earth frame expressed as a unit quaternion $q^{\mathrm{eb}} = \begin{pmatrix} q_0 & q_1 & q_2 & q_3 \end{pmatrix}^{\mathsf{T}}$ and the gyroscope bias b_ω^{b}. In our model we have used the inertial measurements as inputs to the dynamic equations in order to not increase the state dimension. For reasons that will become clear after the model has been provided, we split the state vector into two parts $x_t = \begin{pmatrix} (x_t^{\mathrm{n}})^{\mathsf{T}} & (x_t^{\mathrm{l}})^{\mathsf{T}} \end{pmatrix}^{\mathsf{T}}$, where

$$x_t^{\mathrm{n}} = \begin{pmatrix} (p_t^{\mathrm{e}})^{\mathsf{T}} & (q_t^{\mathrm{eb}})^{\mathsf{T}} \end{pmatrix}^{\mathsf{T}}, \qquad x_t^{\mathrm{l}} = \begin{pmatrix} (v_t^{\mathrm{e}})^{\mathsf{T}} & (b_\omega^{\mathrm{b}})^{\mathsf{T}} \end{pmatrix}^{\mathsf{T}}. \tag{1}$$

2.1 Dynamical model

The dynamical equations can be derived by using the inertial measurements as inputs. A commonly used, slowly time-varying random walk model is used for the gyroscope bias (Hol, 2011). This leads to the following state update equations for the linear and nonlinear states (Hol, 2011; Törnqvist, 2008)

$$\begin{aligned} x^{\mathrm{n}}_{t+1} = {} & \underbrace{\begin{pmatrix} \mathcal{I}_3 & 0 \\ 0 & \mathcal{I}_4 \end{pmatrix}}_{A^{\mathrm{nn}}} x^{\mathrm{n}}_t + \underbrace{\begin{pmatrix} T\mathcal{I}_3 & 0 \\ 0 & -\frac{T}{2}\widetilde{S}(q^{\mathrm{eb}}_t) \end{pmatrix}}_{A^{\mathrm{nl}}_t(x^{\mathrm{n}}_t)} x^{\mathrm{l}}_t + \\ & \underbrace{\begin{pmatrix} \frac{T^2}{2}\mathcal{R}(q^{\mathrm{eb}}_t) & \frac{T^2}{2}\mathcal{I}_3 & 0 \\ 0 & 0 & \frac{T}{2}\widetilde{S}(q^{\mathrm{eb}}_t) \end{pmatrix}}_{B^{\mathrm{n}}_t(x^{\mathrm{n}}_t)} u_t + \underbrace{\begin{pmatrix} \frac{T^2}{2}\mathcal{R}(q^{\mathrm{eb}}_t) & 0 \\ 0 & \frac{T}{2}\widetilde{S}(q^{\mathrm{eb}}_t) \end{pmatrix}}_{G^{\mathrm{n}}_t(x^{\mathrm{n}}_t)} \underbrace{\begin{pmatrix} w^{\mathrm{b}}_{a,t} \\ w^{\mathrm{b}}_{\omega,t} \end{pmatrix}}_{w^{\mathrm{n}}_t} \end{aligned} \tag{2a}$$

$$x^{\mathrm{l}}_{t+1} = \underbrace{\begin{pmatrix} \mathcal{I}_3 & 0 \\ 0 & \mathcal{I}_3 \end{pmatrix}}_{A^{\mathrm{ll}}} x^{\mathrm{l}}_t + \underbrace{\begin{pmatrix} T\mathcal{R}(q^{\mathrm{eb}}_t) & T\mathcal{I}_3 & 0 \\ 0 & 0 & 0 \end{pmatrix}}_{B^{\mathrm{l}}_t(x^{\mathrm{n}}_t)} u_t + \underbrace{\begin{pmatrix} T\mathcal{R}(q^{\mathrm{eb}}_t) & 0 \\ 0 & \mathcal{I}_3 \end{pmatrix}}_{G^{\mathrm{l}}_t(x^{\mathrm{n}}_t)} \underbrace{\begin{pmatrix} w^{\mathrm{b}}_{a,t} \\ w^{\mathrm{b}}_{\mathrm{b}_\omega,t} \end{pmatrix}}_{w^{\mathrm{l}}_t}. \tag{2b}$$

Here, $\mathcal{I}_k$ denotes the identity matrix of size $k \times k$, $\mathcal{R}(q^{\mathrm{eb}}_t) \in SO(3)$ is the rotation matrix obtained from the unit quaternion q^{eb}_t and[1]

$$\widetilde{S}(q^{\mathrm{eb}}_t) = \begin{pmatrix} -q_1 & -q_2 & -q_3 \\ q_0 & -q_3 & q_2 \\ q_3 & q_0 & -q_1 \\ -q_2 & q_1 & q_0 \end{pmatrix}. \tag{3}$$

The input vector u_t is given by

$$u_t = \left((y^{\mathrm{b}}_{\mathrm{a},t})^{\mathsf{T}} \quad (g^{\mathrm{e}})^{\mathsf{T}} \quad (y^{\mathrm{b}}_{\omega,t})^{\mathsf{T}} \right)^{\mathsf{T}}, \tag{4}$$

where g^{e} denotes the gravity vector and the accelerometer and the gyroscope measurements are denoted by $y^{\mathrm{b}}_{\mathrm{a}}$ and y^{b}_{ω}, respectively. The latter are modeled as

$$y^{\mathrm{b}}_{\mathrm{a},t} = R^{\mathrm{be}}_t (a^{\mathrm{e}}_t - g^{\mathrm{e}}) + w^{\mathrm{b}}_{\mathrm{a},t}, \tag{5a}$$

$$y^{\mathrm{b}}_{\omega,t} = \omega^{\mathrm{b}}_t + b^{\mathrm{b}}_{\omega} + w^{\mathrm{b}}_{\omega,t}, \tag{5b}$$

based on the fact that the accelerometer measures both the gravity vector and the body's free acceleration. The noise is modeled as

$$w^{\mathrm{b}}_{\mathrm{a}} \sim \mathcal{N}(0, Q_{\mathrm{a}}), \qquad Q_{\mathrm{a}} = \sigma^2_{\mathrm{a}} \mathcal{I}_3, \tag{6a}$$

$$w^{\mathrm{b}}_{\omega} \sim \mathcal{N}(0, Q_{\omega}), \qquad Q_{\omega} = \sigma^2_{\omega} \mathcal{I}_3, \tag{6b}$$

$$w^{\mathrm{b}}_{\mathrm{b}_\omega} \sim \mathcal{N}(0, Q_{\mathrm{b}_\omega}), \qquad Q_{\mathrm{b}_\omega} = \sigma^2_{\mathrm{b}_\omega} \mathcal{I}_3. \tag{6c}$$

---

[1] Note that the propagation of the quaternion state in this way is an approximation, valid only for high sampling rates. The algorithm does not prevent use of the exact update equation and the approximation is only used to reduce computational complexity.

The state noise is assumed to be distributed according to

$$w_t = \begin{pmatrix} w_t^{\mathrm{n}} \\ w_t^{\mathrm{l}} \end{pmatrix} \sim \mathcal{N}(0, Q), \tag{7a}$$

$$Q = \begin{pmatrix} Q^{\mathrm{nn}} & Q^{\mathrm{nl}} \\ (Q^{\mathrm{nl}})^{\mathsf{T}} & Q^{\mathrm{ll}} \end{pmatrix} = \left(\begin{array}{cc|cc} Q_{\mathrm{a}} & 0 & Q_{\mathrm{a}} & 0 \\ 0 & Q_{\omega} & 0 & 0 \\ \hline Q_{\mathrm{a}}^{\mathsf{T}} & 0 & Q_{\mathrm{a}} & 0 \\ 0 & 0 & 0 & Q_{\mathrm{b}_{\omega}} \end{array}\right). \tag{7b}$$

Note that the linear and nonlinear state noise is highly correlated since the accelerometer noise acts on both the position and velocity states. This needs to be taken into account in the implementation.

2.2 Magnetometer measurement model

The magnetometer measurements are modeled as

$$y_{\mathrm{m},t}^{\mathrm{b}} = h(x_t^{\mathrm{n}}) + e_{\mathrm{m},t}^{\mathrm{b}}, \tag{8}$$

where $e_{\mathrm{m},t}^{\mathrm{b}} \sim \mathcal{N}(0, R)$ and $h(x_t^{\mathrm{n}})$ is a function of the position p_t^{e} and orientation q_t^{eb} states. In practice this will be a superposition of the local earth magnetic field and all magnetic disturbances present.

As discussed in the introduction, to isolate the problem of positioning inside a map from the problem of making the map, we chose an experimental setup where the magnetic field is generated by a magnetic coil. In this case a magnetic field map is analytically known assuming the coil's position and orientation are known. The function $h(x_t^{\mathrm{n}})$ is given by

$$h(x_t^{\mathrm{n}}) = \mathcal{R}(q^{\mathrm{be}}) R^{\mathrm{em}} B(R^{\mathrm{me}} p_t^{\mathrm{e}}). \tag{9}$$

The function $B(R^{\mathrm{me}} p_t^{\mathrm{e}})$ gives the magnetic field in the map coordinate frame at a position p^{m}. The expression for the magnetic field from the coil is given by (Schepers, 2009)

$$B(p^{\mathrm{m}}) = \frac{\mu_0 N_w I}{2\pi\sqrt{\left(\sqrt{p_x^2 + p_y^2} + a\right)^2 + p_z^2}} \begin{pmatrix} \frac{p_x p_z}{p_x^2 + p_y^2}\left[-K(k) + \frac{a^2 + p_x^2 + p_y^2 + p_z^2}{\left(\sqrt{p_x^2+p_y^2} - a\right)^2 + p_z^2} E(k)\right] \\ \frac{p_y p_z}{p_x^2 + p_y^2}\left[-K(k) + \frac{a^2 + p_x^2 + p_y^2 + p_z^2}{\left(\sqrt{p_x^2+p_y^2} - a\right)^2 + p_z^2} E(k)\right] \\ \left[K(k) + \frac{a^2 - p_x^2 - p_y^2 - p_z^2}{\left(\sqrt{p_x^2+p_y^2} - a\right)^2 + p_z^2} E(k)\right] \end{pmatrix} \tag{10}$$

where $p^{\mathrm{m}} = \begin{pmatrix} p_x & p_y & p_z \end{pmatrix}$, μ_0 is the magnetic permeability in vacuum, a is the coil radius, N_w is the number of windings, I is the current through the coil and

$E(k)$ and $K(k)$ are given by the following elliptic integrals

$$E(k) = \int_{0}^{\pi/2} \sqrt{1 - k^2 \sin^2 \theta} d\theta, \tag{11a}$$

$$K(k) = \int_{0}^{\pi/2} \frac{1}{\sqrt{1 - k^2 \sin^2 \theta}} d\theta, \tag{11b}$$

where

$$k = \sqrt{\frac{4a\sqrt{p_x^2 + p_y^2}}{(\sqrt{p_x^2 + p_y^2} + a)^2 + p_z^2}}. \tag{12}$$

These equations implicitly assume that the origin of the earth coordinate frame coincides with that of the map coordinate frame. Note that our measurement model assumes that no background field is present.

2.3 Some additional words about the magnetic field model

The magnetic field of a coil is generally described as a function of the perpendicular distance p_z towards the coil and the radial distance $r = \sqrt{p_x^2 + p_y^2}$ towards the center of the coil (Schepers, 2009; Griffiths, 1999). However, in tracking we are interested in absolute position rather than just the distance to a source. Parametrizing the magnetic field in terms of a position p_x, p_y, p_z introduces unobservability. Assuming the coil is placed horizontally, this results in two horizontal circles, one above and one below the coil, where the horizontal position is coupled to the heading as an unobservable manifold. We assume that the sensor can only be positioned above the coil and therefore have an entire circle of solutions at each time step. Note that in the more general case where multiple magnetic sources are present and possibly rotated with respect to each other, the unobservable manifold will be differently shaped or in some cases non-existent. To make our dynamic model applicable to any magnetic field map, we have not adapted the parametrization of our state vector to this specific structure.

3 Computing the estimate

As can be seen from the dynamical and measurement model presented in Section 2, the state dynamics is assumed to be linear while the measurement model is a nonlinear function of the sensor's position and orientation. A nonlinear filtering technique is therefore needed to compute a state estimate. A linear substructure can, however, be recognized, which can be exploited using a Rao-Blackwellized particle filter (RBPF) in which the state is split into a state x^{l} that enters linearly in both the dynamic and measurement model and a state x^{n} that enters non-linearly, where x^{l} and x^{n} are defined by (1). An RBPF solves the nonlinear filtering problem by using a Kalman filter (KF) for the linear states and a particle filter (PF) for the nonlinear states.

The RBPF in this paper has been derived from Törnqvist (2008) and Lindsten (2011) and is summarized in Algorithm 1. It applies the model structure (2), (8), the noise assumptions (6) and their correlations given in (7). In (13), $\bar{x}_t^i$ and $\bar{P}_t^i$ are computed, which are a stacked version of the nonlinear and linear states and covariances. Based on these, the nonlinear and linear time update are given by (14), (15) respectively. Note that in (15) the pseudo-inverse, denoted by †, of $\bar{P}_t^{\mathrm{nn},i}$ needs to be taken because this matrix is rank deficient due to the presence of quaternion states.

Since the measurement model (9) only depends on the nonlinear states, measurement information about the linear states is in our problem only available through the nonlinear states. Algorithm 1 does therefore not contain an explicit KF measurement update. However, measurement information implicitly present in the nonlinear states is taken into account in the linear states in (15).

3.1 RBPF-MAP

To compare particle filter estimates to reference data, a point estimate needs to be computed at each time step. The most commonly used approach for this is to take the conditional mean estimate. Due to the unobservability in our model (see Section 2.3), however, all particles on a horizontal circle are equally likely, which can lead to an uninformative point estimate in center of the circle.

In Driessen and Boers (2008); Saha et al. (2009) a maximum a posteriori estimate for the particle filter (PF-MAP) has been derived, which is argued to give a better point estimate in multi-modal applications. The PF-MAP estimate is an approximation of the MAP estimate given by

$$\widehat{x}_{t|t}^{\mathrm{MAP}} = \arg\max_{x_t^i} \; p(y_t|x_t^i) \sum_j p(x_t^i|x_{1:t-1}^j) w_{t-1}^j. \tag{16}$$

Following a similar reasoning, the RBPF-MAP estimate, can be shown to be

$$\widehat{x}_{t|t}^{\mathrm{MAP}} = \arg\max_{x_t^{\mathrm{n},i},x_t^{\mathrm{l},i}} \; p(y_t|x_t^{\mathrm{n},i}, x_t^{\mathrm{l},i}) \sum_j w_{t-1}^j \mathcal{N}(x_t^i; \bar{x}_{t|t-1}^j, \bar{P}_{t|t-1}^j), \tag{17}$$

where $\bar{x}_{t|t-1}^j$ and $\bar{P}_{t|t-1}^j$ can be obtained from (13). Note that since our problem does not have a KF measurement update, instead of the commonly used double subscript denoting the time for the linear states, Algorithm 1 only uses a single subscript.

When implementing this in Step 2 of the Algorithm 1, it needs to be taking into account that the covariance matrix $\bar{P}_t^j$ is rank deficient due to the presence of quaternion states. Because computation of (17) is computationally heavy, it could also be considered to use the most probable particle of the posterior. This would

Algorithm 1 Rao-Blackwellized particle filter

1. Initialization: For $i = 1, \ldots, N$ generate $x_0^{\mathrm{n},i} \sim p_{x_0^{\mathrm{n}}}$, set $\{x_0^{\mathrm{l},i}, P_0^i\} = \{x_0^{\mathrm{l}}, P_0\}$, $\gamma_{-1}^i = \frac{1}{N}$, and set $t = 0$.
2. Measurement update: For $i = 1, \ldots, N$ evaluate the particle importance weights $\gamma_t^i = \frac{1}{c_t}\gamma_{t-1}^i p(y_t | x_{0:t}^{\mathrm{n},i}, y_{0:t-1})$ based on (8) where $c_t = \sum_{i=1}^{N} \gamma_{t-1}^i p(y_t | x_{0:t}^{\mathrm{n},i}, y_{0:t-1})$.
3. If $t > 0$, compute the estimate $\widehat{x}_t$ based on (17).
4. Resampling: If $\widehat{N}_{\mathrm{eff}} = \frac{1}{\sum_{i=1}^{N}(\gamma_t^i)^2} < \frac{2}{3}N$, resample N particles with replacement from the set $\{x_t^{\mathrm{n},i}, x_t^{\mathrm{l},i}\}_{i=1}^{N}$ where the probability to take sample i is γ_t^i, and reset the weights to $\gamma_t^i = \frac{1}{N}$.
5. Time update: Determine the Gaussian mixture

$$\bar{x}_{t+1}^i = A_t^i x_t^i + B_t^i u_t, \tag{13a}$$

$$\bar{P}_{t+1}^i = A_t^{\mathrm{l},i} P_t^i (A_t^{\mathrm{l},i})^{\mathsf{T}} + G_t^i Q (G_t^i)^{\mathsf{T}}, \tag{13b}$$

where

$$\bar{x}_t^i = \begin{pmatrix} \bar{x}_t^{\mathrm{n},i} \\ \bar{x}_t^{\mathrm{l},i} \end{pmatrix}, \qquad \bar{P}_t^i = \begin{pmatrix} \bar{P}_t^{\mathrm{nn},i} & \bar{P}_t^{\mathrm{nl},i} \\ (\bar{P}_t^{\mathrm{nl},i})^{\mathsf{T}} & \bar{P}_t^{\mathrm{ll},i} \end{pmatrix},$$

$$A_t^{\mathrm{l},i} = \begin{pmatrix} A_t^{\mathrm{nl},i}(x_t^{\mathrm{n},i}) \\ A^{\mathrm{ll}} \end{pmatrix}, \qquad A_t^i = \begin{pmatrix} A^{\mathrm{nn}} & A_t^{\mathrm{nl},i}(x_t^{\mathrm{n},i}) \\ 0 & A^{\mathrm{ll}} \end{pmatrix},$$

$$B_t^i = \begin{pmatrix} B_t^{\mathrm{n},i}(x_t^{\mathrm{n},i}) \\ B_t^{\mathrm{l},i}(x_t^{\mathrm{n},i}) \end{pmatrix}, \qquad G_t^i = \begin{pmatrix} G_t^{\mathrm{n},i}(x_t^{\mathrm{n},i}) & 0 \\ 0 & G_t^{\mathrm{l},i}(x_t^{\mathrm{n},i}) \end{pmatrix}.$$

The nonlinear states can now sampled according to

$$x_{t+1}^{\mathrm{n},i} \sim \mathcal{N}(\bar{x}_{t+1}^{\mathrm{n},i}, \bar{P}_{t+1}^{\mathrm{nn},i}), \tag{14}$$

and the linear states can be updated according to

$$x_{t+1}^{\mathrm{l},i} = \bar{x}_{t+1}^{\mathrm{l},i} + (\bar{P}_{t+1}^{\mathrm{nl},i})^{\mathsf{T}} (\bar{P}_{t+1}^{\mathrm{nn},i})^{\dagger} (x_{t+1}^{\mathrm{n},i} - \bar{x}_{t+1}^{\mathrm{n},i}), \tag{15a}$$

$$P_{t+1}^i = \bar{P}_{t+1}^{\mathrm{ll},i} - (\bar{P}_{t+1}^{\mathrm{nl},i})^{\mathsf{T}} (\bar{P}_{t+1}^{\mathrm{nn},i})^{\dagger} \bar{P}_{t+1}^{\mathrm{nl},i}. \tag{15b}$$

6. Set $t := t + 1$ and iterate from Step 2.

lead to similar results in Section 4.

4 Experimental results

4.1 Experimental setup

An experiment has been performed in which the magnetic field is generated by a magnetic coil where the number of windings N_w is equal to 50, the current I through the coil is 1 A and the radius a of the coil is 6 cm. A MEMS IMU (Xsens MTi) providing synchronized inertial and magnetometer measurements at a sampling frequency of 100 Hz is used. A picture of the experimental setup can be found in Figure 2. Ground truth data is collected from an optical reference system (Vicon system) and is used for validation of the estimates as well as for determining the position and orientation R^{em} of the coil.

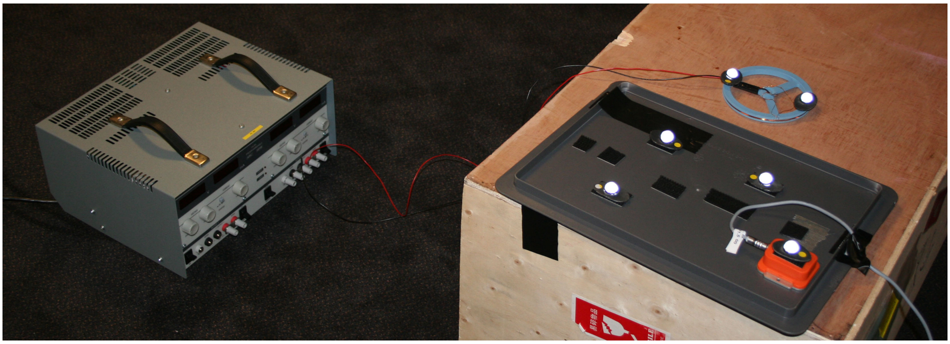

Figure 2: *The experimental setup consisting of an IMU (orange box), a coil and a power supply. Optical markers are present, used for obtaining ground truth data, via an optical reference system.*

Before the magnetometer measurements can be used in Algorithm 1, they need to be preprocessed for two reasons. First, the model (9) assumes that the magnetometer only measures the magnetic field due to a coil. A constant term representing the local earth magnetic field therefore needs to be determined and subtracted from all measurements. Second, the IMU used outputs magnetometer measurements in arbitrary units, while the model (9) determines the magnetic field in Tesla. A constant multiplication on all axes is therefore needed. Both constants are obtained by determining a best estimate from a part of the data where the magnetic disturbance is (approximately) zero. The preprocessed data is illustrated in Figure 1. The circles represent the preprocessed magnetometer measurements, downsampled to 4 Hz. The color of the circles represents the magnitude of the magnetic field. The magnetic field falls off cubically with distance which explains why the magnitude of the magnetic field is reduced quickly with distance from the coil. Each preprocessed measurement also gives rise to a red arrow indicating the direction of the magnetic field. The length of the arrows illustrates the magnitude.

4.2 Results

Using the collected inertial and magnetometer data, Algorithm 1 can be applied to obtain state estimates. Due to the fact that the magnitude of the magnetic field falls off cubically with distance, all results in this section are based on data no further away from the coil's origin than 40 cm. These have been compared to the ground truth data from the reference system. This section focuses on analysis of the position estimates. Due to the unobservability discussed in Section 2.3 we do not expect exact matches between the RBPF estimates and the ground truth data. A good comparison of the quality of the estimates, however, are the radial position and height estimates. The error plots can be found in Figure 3. The RBPF is initialized around the true estimate using the reference data, but any other (reasonable) initialization will give comparable results.

As can be seen in Figure 3, very good position estimates are obtained. However, at approximately 42 s, there is a big peak in both the radial position and the height errors. This can be explained by the fact that at this time instant, the sensor is the furthest away from the coil, almost 40 cm. The approach presented in this work is thus able to obtain high accurate position estimates for longer times, only when the sensor remains close to the coil. This is a major limitation in using the magnetic field as a source of position information in the way presented in this paper. The further away from the magnetic disturbance the less informative the measurements become. Even though at 40 cm from the coil the signal to noise ratio is still good, tracking problems occur due to model errors. It is therefore important to have a good model of the magnetic field (Wahlström et al., 2013).

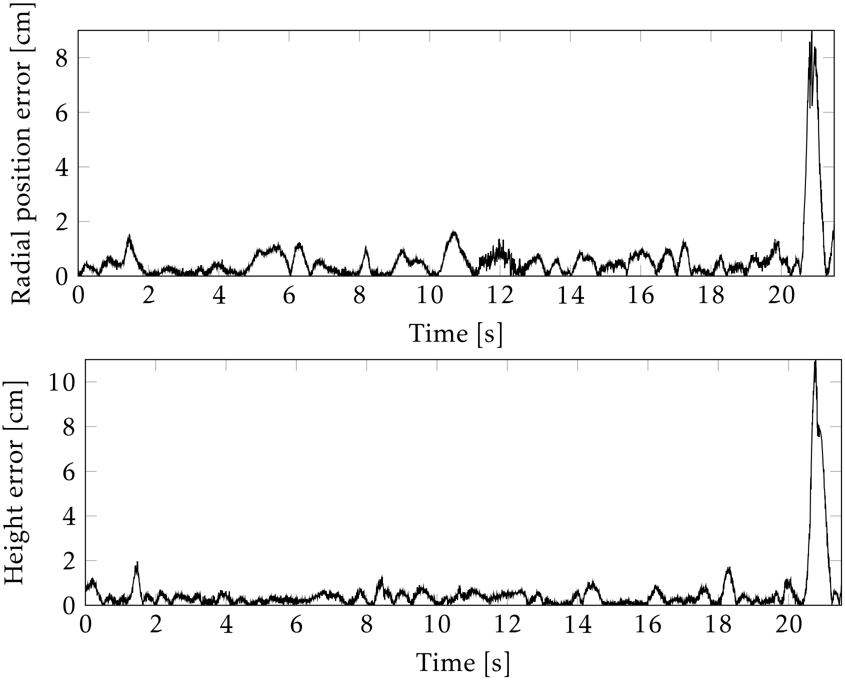

Figure 3: *Error plots comparing the RBPF position estimates with the ground truth data from the optical reference system.*

5 Conclusions and future work

This paper has shown that close to a magnetic distortion generated by a magnetic coil, good position and orientation estimates can be obtained from inertial and magnetometer data only. Ideas for future work include extending the magnetometer model to a more realistic measurement model. First trials show that we can probably deal with including the local earth magnetic field. We also aim at combining this work with Wahlström et al. (2013) into an approach where simultaneous localization and mapping (SLAM) is possible. Another future line of research aims at studying the unobservability manifolds from the magnetic field in different cases.

Acknowledgements

This work is supported by MC Impulse, a European Commission, FP7 research project and CADICS, a Linneaus Center funded by the Swedish Research Council (VR). The authors would like to thank Xsens Technologies for their support in starting this work as well as in collecting the data sets and Dr. Slawomir Grzonka for pointing out this interesting field of research.

Bibliography

J. Chung, M. Donahoe, C. Schmandt, I. J. Kim, P. Razavai, and M. Wiseman. Indoor location sensing using geo-magnetism. In *Proceedings of the 9th international conference on Mobile systems, applications, and services (MobiSys)*, pages 141–154, Bethesda, USA, June 2011.

E. Dorveaux, T. Boudot, M. Hillion, and N. Petit. Combining inertial measurements and distributed magnetometry for motion estimation. In *Proceedings of the American Control Conference (ACC)*, pages 4249–4256, San Francisco, USA, June 2011. IEEE.

H. Driessen and Y. Boers. MAP estimation in particle filter tracking. In *IET Seminar on Target Tracking and Data Fusion: Algorithms and Applications*, pages 41–45, 2008.

E. Georgiou and J. Dai. Self-localization of an autonomous maneuverable nonholonomic mobile robot using a hybrid double-compass configuration. In *Proceedings of the 7th International Symposium on Mechatronics and its Applications (ISMA)*, pages 1–8, Sharjah, United Arab Emirates, April 2010. IEEE.

B. Gozick, K. P. Subbu, R. Dantu, and T. Maeshiro. Magnetic maps for indoor navigation. *IEEE Transactions on Instrumentation and Measurement*, 60(12): 3883–3891, 2011.

D. J. Griffiths. *Introduction to electrodynamics*, volume 3. Prentice Hall, New Jersey, 1999.

J. D. Hol. *Sensor Fusion and Calibration of Inertial Sensors, Vision, Ultra-Wideband and GPS*. PhD thesis, Linköping University, Sweden, June 2011.

IndoorAtlas. `http://www.indooratlas.com`, Accessed on November 30, 2012.

M. Kok, N. Wahlström, T. B. Schön, and F. Gustafsson. MEMS-based inertial navigation based on a magnetic field map. In *Proceedings of the 38th International Conference on Acoustics, Speech, and Signal Processing (ICASSP)*, pages 6466–6470, Vancouver, Canada, May 2013.

F. Lindsten. *Rao-Blackwellised particle methods for inference and identification*. Licentiate thesis, Linköping University, Sweden, 2011.

D. Navarro and G. Benet. Magnetic map building for mobile robot localization purpose. In *Proceedings of the IEEE Conference on Emerging Technologies and Factory Automation (ETFA)*, pages 1–4, Mallorca, Spain, September 2009.

S. Saha, Y. Boers, H. Driessen, P. K. Mandal, and A. Bagchi. Particle based MAP state estimation: A comparison. In *Proceedings of the 12th International Conference on Information Fusion*, pages 278–283, July 2009.

H. M. Schepers. *Ambulatory assessment of human body kinematics and kinetics*. PhD thesis, University of Twente, Enschede, June 2009.

S. Suksakulchai, S. Thongchai, D. M. Wilkes, and K. Kawamura. Mobile robot localization using an electronic compass for corridor environment. In *Proceedings of the IEEE International Conference on Systems, Man, and Cybernetics (SMC)*, volume 5, pages 3354–3359, Nashville, USA, October 2000.

D. Törnqvist. *Estimation and Detection with Applications to Navigation*. PhD thesis, Linköping University, November 2008. Thesis No. 1216.

I. Vallivaara, J. Haverinen, A. Kemppainen, and J. Roning. Magnetic field-based SLAM method for solving the localization problem in mobile robot floor-cleaning task. In *Proceedings of the 15th International Conference on Advanced Robotics (ICAR)*, pages 198–203, Tallinn, Estonia, June 2011.

D. Vissière, A.P. Martin, and N. Petit. Using magnetic disturbances to improve IMU-based position estimation. In *Proceedings of the European Control Conference (ECC)*, pages 2853–2858, Kos, Greece, July 2007.

N. Wahlström, M. Kok, T. B. Schön, and F. Gustafsson. Modeling magnetic fields using Gaussian processes. In *Proceedings of the 38th International Conference on Acoustics, Speech, and Signal Processing (ICASSP)*, pages 3522–3526, Vancouver, Canada, May 2013.

Licentiate Theses
Division of Automatic Control
Linköping University

P. Andersson: Adaptive Forgetting through Multiple Models and Adaptive Control of Car Dynamics. Thesis No. 15, 1983.

B. Wahlberg: On Model Simplification in System Identification. Thesis No. 47, 1985.

A. Isaksson: Identification of Time Varying Systems and Applications of System Identification to Signal Processing. Thesis No. 75, 1986.

G. Malmberg: A Study of Adaptive Control Missiles. Thesis No. 76, 1986.

S. Gunnarsson: On the Mean Square Error of Transfer Function Estimates with Applications to Control. Thesis No. 90, 1986.

M. Viberg: On the Adaptive Array Problem. Thesis No. 117, 1987.

K. Ståhl: On the Frequency Domain Analysis of Nonlinear Systems. Thesis No. 137, 1988.

A. Skeppstedt: Construction of Composite Models from Large Data-Sets. Thesis No. 149, 1988.

P. A. J. Nagy: MaMiS: A Programming Environment for Numeric/Symbolic Data Processing. Thesis No. 153, 1988.

K. Forsman: Applications of Constructive Algebra to Control Problems. Thesis No. 231, 1990.

I. Klein: Planning for a Class of Sequential Control Problems. Thesis No. 234, 1990.

F. Gustafsson: Optimal Segmentation of Linear Regression Parameters. Thesis No. 246, 1990.

H. Hjalmarsson: On Estimation of Model Quality in System Identification. Thesis No. 251, 1990.

S. Andersson: Sensor Array Processing; Application to Mobile Communication Systems and Dimension Reduction. Thesis No. 255, 1990.

K. Wang Chen: Observability and Invertibility of Nonlinear Systems: A Differential Algebraic Approach. Thesis No. 282, 1991.

J. Sjöberg: Regularization Issues in Neural Network Models of Dynamical Systems. Thesis No. 366, 1993.

P. Pucar: Segmentation of Laser Range Radar Images Using Hidden Markov Field Models. Thesis No. 403, 1993.

H. Fortell: Volterra and Algebraic Approaches to the Zero Dynamics. Thesis No. 438, 1994.

T. McKelvey: On State-Space Models in System Identification. Thesis No. 447, 1994.

T. Andersson: Concepts and Algorithms for Non-Linear System Identifiability. Thesis No. 448, 1994.

P. Lindskog: Algorithms and Tools for System Identification Using Prior Knowledge. Thesis No. 456, 1994.

J. Plantin: Algebraic Methods for Verification and Control of Discrete Event Dynamic Systems. Thesis No. 501, 1995.

J. Gunnarsson: On Modeling of Discrete Event Dynamic Systems, Using Symbolic Algebraic Methods. Thesis No. 502, 1995.

A. Ericsson: Fast Power Control to Counteract Rayleigh Fading in Cellular Radio Systems. Thesis No. 527, 1995.

M. Jirstrand: Algebraic Methods for Modeling and Design in Control. Thesis No. 540, 1996.

K. Edström: Simulation of Mode Switching Systems Using Switched Bond Graphs. Thesis No. 586, 1996.

J. Palmqvist: On Integrity Monitoring of Integrated Navigation Systems. Thesis No. 600, 1997.
A. Stenman: Just-in-Time Models with Applications to Dynamical Systems. Thesis No. 601, 1997.
M. Andersson: Experimental Design and Updating of Finite Element Models. Thesis No. 611, 1997.
U. Forssell: Properties and Usage of Closed-Loop Identification Methods. Thesis No. 641, 1997.
M. Larsson: On Modeling and Diagnosis of Discrete Event Dynamic systems. Thesis No. 648, 1997.
N. Bergman: Bayesian Inference in Terrain Navigation. Thesis No. 649, 1997.
V. Einarsson: On Verification of Switched Systems Using Abstractions. Thesis No. 705, 1998.
J. Blom, F. Gunnarsson: Power Control in Cellular Radio Systems. Thesis No. 706, 1998.
P. Spångéus: Hybrid Control using LP and LMI methods – Some Applications. Thesis No. 724, 1998.
M. Norrlöf: On Analysis and Implementation of Iterative Learning Control. Thesis No. 727, 1998.
A. Hagenblad: Aspects of the Identification of Wiener Models. Thesis No. 793, 1999.
F. Tjärnström: Quality Estimation of Approximate Models. Thesis No. 810, 2000.
C. Carlsson: Vehicle Size and Orientation Estimation Using Geometric Fitting. Thesis No. 840, 2000.
J. Löfberg: Linear Model Predictive Control: Stability and Robustness. Thesis No. 866, 2001.
O. Härkegård: Flight Control Design Using Backstepping. Thesis No. 875, 2001.
J. Elbornsson: Equalization of Distortion in A/D Converters. Thesis No. 883, 2001.
J. Roll: Robust Verification and Identification of Piecewise Affine Systems. Thesis No. 899, 2001.
I. Lind: Regressor Selection in System Identification using ANOVA. Thesis No. 921, 2001.
R. Karlsson: Simulation Based Methods for Target Tracking. Thesis No. 930, 2002.
P.-J. Nordlund: Sequential Monte Carlo Filters and Integrated Navigation. Thesis No. 945, 2002.
M. Östring: Identification, Diagnosis, and Control of a Flexible Robot Arm. Thesis No. 948, 2002.
C. Olsson: Active Engine Vibration Isolation using Feedback Control. Thesis No. 968, 2002.
J. Jansson: Tracking and Decision Making for Automotive Collision Avoidance. Thesis No. 965, 2002.
N. Persson: Event Based Sampling with Application to Spectral Estimation. Thesis No. 981, 2002.
D. Lindgren: Subspace Selection Techniques for Classification Problems. Thesis No. 995, 2002.
E. Geijer Lundin: Uplink Load in CDMA Cellular Systems. Thesis No. 1045, 2003.
M. Enqvist: Some Results on Linear Models of Nonlinear Systems. Thesis No. 1046, 2003.
T. Schön: On Computational Methods for Nonlinear Estimation. Thesis No. 1047, 2003.
F. Gunnarsson: On Modeling and Control of Network Queue Dynamics. Thesis No. 1048, 2003.
S. Björklund: A Survey and Comparison of Time-Delay Estimation Methods in Linear Systems. Thesis No. 1061, 2003.

M. Gerdin: Parameter Estimation in Linear Descriptor Systems. Thesis No. 1085, 2004.

A. Eidehall: An Automotive Lane Guidance System. Thesis No. 1122, 2004.

E. Wernholt: On Multivariable and Nonlinear Identification of Industrial Robots. Thesis No. 1131, 2004.

J. Gillberg: Methods for Frequency Domain Estimation of Continuous-Time Models. Thesis No. 1133, 2004.

G. Hendeby: Fundamental Estimation and Detection Limits in Linear Non-Gaussian Systems. Thesis No. 1199, 2005.

D. Axehill: Applications of Integer Quadratic Programming in Control and Communication. Thesis No. 1218, 2005.

J. Sjöberg: Some Results On Optimal Control for Nonlinear Descriptor Systems. Thesis No. 1227, 2006.

D. Törnqvist: Statistical Fault Detection with Applications to IMU Disturbances. Thesis No. 1258, 2006.

H. Tidefelt: Structural algorithms and perturbations in differential-algebraic equations. Thesis No. 1318, 2007.

S. Moberg: On Modeling and Control of Flexible Manipulators. Thesis No. 1336, 2007.

J. Wallén: On Kinematic Modelling and Iterative Learning Control of Industrial Robots. Thesis No. 1343, 2008.

J. Harju Johansson: A Structure Utilizing Inexact Primal-Dual Interior-Point Method for Analysis of Linear Differential Inclusions. Thesis No. 1367, 2008.

J. D. Hol: Pose Estimation and Calibration Algorithms for Vision and Inertial Sensors. Thesis No. 1370, 2008.

H. Ohlsson: Regression on Manifolds with Implications for System Identification. Thesis No. 1382, 2008.

D. Ankelhed: On low order controller synthesis using rational constraints. Thesis No. 1398, 2009.

P. Skoglar: Planning Methods for Aerial Exploration and Ground Target Tracking. Thesis No. 1420, 2009.

C. Lundquist: Automotive Sensor Fusion for Situation Awareness. Thesis No. 1422, 2009.

C. Lyzell: Initialization Methods for System Identification. Thesis No. 1426, 2009.

R. Falkeborn: Structure exploitation in semidefinite programming for control. Thesis No. 1430, 2010.

D. Petersson: Nonlinear Optimization Approaches to $\mathcal{H}_2$-Norm Based LPV Modelling and Control. Thesis No. 1453, 2010.

Z. Sjanic: Navigation and SAR Auto-focusing in a Sensor Fusion Framework. Thesis No. 1464, 2011.

K. Granström: Loop detection and extended target tracking using laser data. Thesis No. 1465, 2011.

J. Callmer: Topics in Localization and Mapping. Thesis No. 1489, 2011.

F. Lindsten: Rao-Blackwellised particle methods for inference and identification. Thesis No. 1480, 2011.

M. Skoglund: Visual Inertial Navigation and Calibration. Thesis No. 1500, 2011.

S. Khoshfetrat Pakazad: Topics in Robustness Analysis. Thesis No. 1512, 2011.

P. Axelsson: On Sensor Fusion Applied to Industrial Manipulators. Thesis No. 1511, 2011.

A. Carvalho Bittencourt: On Modeling and Diagnosis of Friction and Wear in Industrial Robots. Thesis No. 1516, 2012.

P. Rosander: Averaging level control in the presence of frequent inlet flow upsets . Thesis No. 1527, 2012.

N. Wahlström: Localization using Magnetometers and Light Sensors. Thesis No. 1581, 2013.

R. Larsson: System Identification of Flight Mechanical Characteristics. Thesis No. 1599, 2013.

Y. Jung: Estimation of Inverse Models Applied to Power Amplifier Predistortion. Thesis No. 1605, 2013.

M. Syldatk: On Calibration of Ground Sensor Networks. Thesis No. 1611, 2013.

M. Roth: Kalman Filters for Nonlinear Systems and Heavy-Tailed Noise. Thesis No. 1613, 2013.

D. Simon: Model Predictive Control in Flight Control Design — Stability and Reference Tracking. Thesis No. 1642, 2014.

J. Dahlin: Sequential Monte Carlo for inference in nonlinear state space models. Thesis No. 1652, 2014.